Contribution to the Dynamics of a Solar Sail in the Earth - Sun System

Ariadna Farrés

Departament de Matemàtica Aplicada i Anàlisi
Universitat de Barcelona

Programa de doctorat de Matemàtiques.
Bienni 2003-2005.

Memòria presentada per aspirar al grau de Doctor en Matemàtiques per la Universitat de Barcelona.

Certifico que aquesta memòria ha estat realitzada per Arianda Farrés Basiana, i dirigida per mi.

Barcelona, 29 de juny de 2009

Àngel Jorba Monte.

Als meus pares i el meu germà

Contents

Agraïments

En aquest moments és fàcil oblidar-se algú, ja que són moltes les persones amb les qui he compartit aquests anys de tesi, i moltes les que han aportat d'una manera o d'una altra alguna cosa durant aquest llarg viatge.

Recordo que un dia l'Àngel em va dir que fer una tesi imprimia caràcter i que et feia conèixer a tu mateix. I crec que té tota la raó, no sé si tinc més caràcter que abans de començar, però sí que és cert que he conegut parts de mi que desconeixia. A ell voldria agrair-li especialment tot el que m'ha ensenyat, tant en l'àmbit professional com en el personal, i per tota la paciència que ha tingut amb mi aguantant les meves cabòries i canvis d'opinió. De ben segur que sense ell aquesta tesi no hagués estat possible. Gràcies.

També m'agradaria agrair a tots els meus companys del Departament de Matemàtica Aplicada i Anàlisi de la Universitat de Barcelona, el bon ambient de treball i tots els mitjans que sempre han posat al meu abast. Especialment a en Carles Simó i a en Gerard Gómez, per l'interès que sempre han mostrat en la meva recerca i totes les aportacions que hi han fet. Tampoc voldria deixar de banda els joves companys del xalet: Pau, Jordi, Arturo, Eli, Eva Marina, Eva, Montse, Jordi-Lluís, Ruben, Anna ... (i segur que em deixo algú), pels grans moments durant tantes hores de dinars i cafès a mig matí i mitja tarda. Ells han fet que venir a treballar aquest últim any hagi estat tot un plaer.

Durant tots aquest anys, entre cursos, congressos i trobades científiques varies he conegut gent meravellosa, dels qui he après molt i amb els qui he compartit grans moments. A tots vosaltres moltes gràcies per fer-me gaudir del món de les matemàtiques.

En la part personal, m'agradaria agrair els meus pares per tot el suport que m'han donat tots aquests anys. Per creure en mi incondicionalment, recolzar-me en les meves decisions i estar sempre al meu costat. I també al meu germanet, Jordi, ja que no puc imaginar millor company d'aventures. Ja saps que t'estimo molt i que vull que seguim tenint grans moments tots dos junts.

No puc oblidar-me de la resta de la meva família, ja que són una part molt important de la meva vida. Als meus avis, agrair-los tot l'amor que sempre m'han donat i que espero

ser capaç de tornar-los-hi mica en mica. I a tots els meus tiets i cosins per fer de cada dinar familiar una festa de la qual no vull marxar mai.

Finalment agrair a la colla de Sant Pol 2000, per mostrar tant d'interès en tot el que faig i pels grans moments que hem viscut tots plegats. I a les meves companyes d'equip, especialment a l'Ana, Núria i Marina, per sempre estar al meu costat.

A tots i cadascun de vosaltres MOLTES GRÀCIES !!!

Resum

Les veles solars són un nou concepte de propulsió espacial que mira d'aprofitar la pressió de radiació solar per accelerar una nau. Una vela solar és, essencialment, una gran superfície reflectant molt lleugera, de manera que l'impacte dels fotons que emet el sol sobre aquesta impulsen la nau. En els últims anys les agències espacials han començat a investigar aquesta nova tecnologia. Malauradament encara no s'ha desplegat amb èxit cap vela solar a l'espai. Els dos intents més recents són *Cosmos 1* i *NanoSail*. Totes dues missions van fallar abans que la nau arribés a l'òrbita nominal, sense tenir opcions de provar de desplegar la vela solar i estudiar-ne el seu comportament. Però tot sembla indicar que algun dia les veles solar seran una realitat.

S'han fet molts estudis sobre veles solars i les seves aplicacions. El llibre de referència en aquesta àrea és [McI99] on estan resumits la major part dels estudis fins el 1999. El disseny d'una vela solar, models per a les forces, la dinàmica en òrbites al voltant del sol o d'un planeta, són alguns dels temes que es tracten en aquest llibre. De totes maneres, les eines de sistemes dinàmics no han tingut massa influència, de moment, en aquesta àrea.

L'ús de sistemes dinàmics en astrodinàmica no és nou pel grup de sistemes dinàmics de la UB i UPC. A [GLMS01a, GLMS01b, GJMS01] trobem un recull de diversos problemes d'astrodinàmica on s'han aplicat eines de sistemes dinàmics per a aplicacions concretes. Nosaltres proposem usar idees similars per tal de navegar amb una vela solar en el sistema Terra - Sol.

Un dels objectius principals d'aquesta tesi és estudiar, de manera extensa, la dinàmica natural d'una vela solar en el sistema Terra - Sol. Aquest és un primer pas, per poder dissenyar estratègies per a la navegació, com per exemple: estratègies de control al voltant d'un punt d'equilibri, una òrbita periòdica o un tor invariant o bé usar les varietats invariants per moure'ns per l'espai. En el capítol 1 fem una descripció dels aspectes més rellevants sobre veles solars i expliquem el model que usarem.

Hem usat com a model el Problema Restringit de Tres Cossos afegint l'efecte de la pressió de radiació solar. És ben sabut [Sze67] que el Problema Restringit de Tres

Cossos en coordenades sinòdiques té 5 punts d'equilibri, que corresponen a les posicions on l'atracció gravitatòria dels dos primaris, la Terra i el Sol, es compensa. Quan afegim l'efecte de la vela, tenim una força més amb la que jugar. En aquest cas tenim una família $2D$ de punts d'equilibri parametritzada per l'orientació de la vela. Aquests nous punts d'equilibri obren un ampli ventall de possibles missions que no poden ser assolides usant un sistema de propulsió "tradicional". Dos exemples són les missions "Geostorm" i "Polar Observer" [McI99]. Totes dues missions requereixen mantenir un satèl·lit al voltant d'un punt d'equilibri durant molt de temps, cosa que no es pot assolir amb un sistema de propulsió tradicional, degut a les limitacions en el combustible. La missió Geostorm pretén mantenir un satèl·lit prop d'un punt d'equilibri situat entre la Terra i el Sol, lleugerament desplaçat cap al Sol respecte el clàssic L_1, amb l'objectiu de monitoritzar les tempestes electromagnètiques. D'altra banda Polar Observer vol mantenir una nau en un punt d'equilibri situat sobre del pla de l'eclíptica, visualitzant de manera constant un dels dos pols de la Terra.

La major part dels punts d'equilibri són inestables. Per tant necessitem una estratègia de control per tal de mantenir la trajectòria d'una vela solar prop del punt. Hem dissenyat una estratègia de control usant eines de sistemes dinàmics, en el capítol 2 n'expliquem els detalls. La idea rau en entendre la variació de l'espai de fase quan varia l'orientació de la vela. Podem veure que prop del punt d'equilibri la dinàmica es pot aproximar per un moviment del tipus sella $\times$ centre $\times$ centre. Per tant, quan la vela està prop del punt d'equilibri, la trajectòria s'escapa al llarg de la direcció inestable. Si canviem l'orientació de la vela, els punts d'equilibri varien lleugerament i el mateix passa amb les direccions estables i inestables. Volem trobar un nou punt d'equilibri de manera que la direcció inestable d'aquest nou punt porti la trajectòria de la vela prop del punt d'equilibri inicial. Per altra banda, s'ha de tenir en compte la component central del moviment, ja que aquesta podria créixer i fer escapar la trajectòria de la nau. Hem aplicat aquestes estratègies per a les dues missions ja mencionades, per mantenir una vela solar prop del punt d'equilibri durant 30 anys. També hem fet simulacions incloent errors en la determinació de la posició i velocitat de la vela, i errors en l'orientació de la vela.

Més endavant ens agradaria estendre aquestes idees per a dissenyar estratègies de control al voltant d'òrbites periòdiques. Per aquest motiu necessitem conèixer la dinàmica no lineal al voltant d'un punt d'equilibri i veure com varia quan canviem l'orientació de la vela. En aquesta ens hem fixat principalment en la regió de punts d'equilibri prop de SL_1 (SL_1 és el punt d'equilibri L_1 desplaçat degut a l'efecte de la vela quan aquesta està orientada perpendicular a la direcció del sol).

Hem desenvolupat eines numèriques per poder estudiar el moviment periòdic i quasi-periòdic prop de SL_1. Aquestes eines són generals i poden ser usades al voltant d'altres punts d'equilibri.

Degut a la inestabilitat de la regió, no podem prendre condicions inicials arbitràries i integrar-les numèricament, ja que les trajectòries s'escaparien ràpidament d'un entorn del punt d'equilibri. Per aquest motiu, proposem fer la reducció a la varietat centre al voltant dels diferents punts d'equilibri. Volem trobar una aproximació d'ordre alt de la dinàmica a la varietat centre, i usar-la per descriure'n el seu comportament. Donat que el sistema és Hamiltonià només per un conjunt petit de paràmetres, no ens en podem aprofitar com a [Jor99, JM99] on es discuteix la dinàmica prop dels punts colineals del RTBP. En aquest cas, calcularem la sèrie de potencies del graph de la varietat centre, $y = v(x)$, al voltant del punt d'equilibri a ordre alt [Sim90, Har08]. Estem interessats en tenir un mètode eficient, ja que volem estudiar diversos casos per a l'orientació de la vela. Al capítol 3 descrivim el mètode i com implementar-lo per a tenir un codi eficient. També hem comparat, en termes d'eficiència, aquest mètode amb el mètode de les sèries de Lie, pel cas particular d'una vela perpendicular a la direcció del sol, i.e. on el sistema sí que és Hamilitonià.

Finalment, en el capítol 4 descrivim la dinàmica al voltant dels diferents punts d'equilibri prop de SL_1. Calculem famílies d'òrbites periòdiques usant mètodes de continuació, i usarem les aproximacions de la varietat centre trobades en el capítol anterior per entendre el moviment quasi-periòdic en un entorn del punt d'equilibri. Al voltant de cada un dels punts d'equilibri hi trobem dues famílies d'òrbites periòdiques, cada una relacionada amb una de les dues freqüències que defineixen el moviment central. La interacció entre les dues freqüències dóna lloc a famílies de tors invariants. També hi trobem òrbites del tipus Halo que apareixen després d'una bifurcació en la família plana d'òrbites periòdiques.

En acabar resumim els resultats més rellevants i puntualitzem algunes possibles direccions de cara al futur.

Introduction

Solar sails are a new concept of spacecraft propulsion that has more adepts everyday. The idea is to provide a spacecraft with a large membrane mirror such that the impact of the photons emitted by the Sun and their further reflection produce momentum on it. For the moment there has yet not been a successful deployment of a solar sail in space, although lately there have been a couple of attempts: *Cosmos 1* and *NanoSail*. Both missions failed before the spacecraft could get to the nominal orbit, not being able to deploy the solar sail and test the technology. In the last years, space agencies have started to invest in this technology and it seems that at some point solar sails will become a reality.

Studies on the use of a solar sails have been done in the past. One of the reference books in the field is [McI99] where most of the studies on the subject up to 1999 are summarised. The design of solar sails, the force models for the different structures, the dynamics on heliocentric or geocentric orbits are some of the subjects covered in this book. Nevertheless, dynamical system tools have had a small influence in this area.

The use of dynamical systems tools in astrodynamics is not new for the UB-UPC Dynamical System group. Lots of studies have been made in the past applying this tools to several astrodynamical problems [GLMS01a, GLMS01b, GJMS01]. We propose to use similar ideas to navigate through the Earth - Sun system with a solar sail.

One of the goals of this thesis is to study, in an extended way, the natural dynamics of a solar sail in the Earth - Sun system. This is a first step of a more ambitious project of designing strategies for different kind of mission application such as, station keeping strategies around equilibrium points, periodic orbits and invariant tori, or consider using invariant manifold to go from one region on the phase space to the other in a natural way. Either using solar sails or other type of low - thrust spacecraft propulsion, covering most of this aspects within the framework of dynamical systems.

In Chapter 1 we review some of the known aspects on solar sails and explain the model and problems that we want to face. We use the Restricted Three Body Problem (RTBP) adding the solar radiation pressure on the solar sail as a model and study some of its most

relevant dynamical properties.

It is well known [Sze67], that the Restricted Three Body Problem in synodical coordinates has 5 equilibrium points, which correspond to the position where the gravitational attraction of the two primaries, Earth and Sun, compensate. When we consider the extra effect of the solar sail, there is a 2D family of new equilibria parametrised by the sail orientation. These artificially generated equilibrium points open a wide new range of possible mission applications, the Geostorm mission and the Polar Observer are two examples [McI99]. The Geostorm is a mission concept where a modest sail is placed Sunwards of the classical Earth - Sun L_1 point. Then using a magnetometer to detect the solar wind polarity enables to double the time of alert of a conventional L_1 Halo orbiter such as SOHO. The Polar Observer aims to use an artificial equilibrium point displaced above the ecliptic plane, high above one of the Earth's poles. This would provide constant real-time views of the polar latitudes for studding, for instance, climate change.

Most of these equilibrium points are unstable, hence a station keeping strategy is required if we want to maintain the solar sail close to equilibria for a long time. In Chapter 2 we derive a station keeping strategy using dynamics system tools. The idea is to understand the variation of the phase space when the sail orientation is changed. We can see that the linear dynamics around these equilibrium points is closely approximated by a saddle $\times$ centre $\times$ centre motion. Hence when the sail is close to the equilibrium point its trajectory will escape along the unstable direction. If we change the sail orientation, the fixed position varies slightly, and so do the stable and unstable directions. We want to find a new sail orientation such that the unstable direction of the new equilibrium brings the trajectory back to a vicinity of the initial position. Furthermore, one must take into account the centre projection of the motion, as this one can result of an unbounded growth. We have applied these strategies for the two missions mentioned before maintaining the solar sail around the desired equilibrium point up to 30 years. We have also tested the robustness of our strategies including errors in the position and velocity determination, as well as errors on the orientation of the sail at each manoeuvre. We will discuss the effect of these errors on the controllability of the solar sail.

Further on, we would like to extend these ideas to derive station keeping strategies around periodic orbits. For this reason we need to have a more complete understanding of the non-linear dynamics around an equilibrium point, and how it varies when the sail orientation changes. In this thesis we have focused on the motion in a close neighbourhood of the displaced L_1 equilibrium point for a solar sail, called SL_1.

We have developed numerical tools for the study of the bounded motion close to SL_1.

These techniques are very general and can be applied around other equilibrium points.

Due to the instability of the region, we cannot take arbitrary initial conditions and integrate them numerically, as they would quickly escape from the vicinity of the fixed point. For this reason, we propose to perform the reduction to the centre manifold around the different equilibrium points. We want to find a high order approximation of the motion on the centre manifold and use it to describe the motion on it. As the system is only Hamiltonian for a small set of values of the sail orientation we cannot take advantage of this as in [Jor99, JM99] where the motion around the collinear points of the RTBP is discussed. Instead, we compute the power expansion of the graph, $y = v(x)$, of the centre manifold around an equilibrium point up to high order [Sim90, Har08]. We are interested in an efficient algorithm as we want to do the reduction to the centre manifold for different sail orientations. In Chapter 3 we describe this algorithm and also give some details on the implementation of an efficient code. We also compare the efficiency of our algorithms with the Lie series method, for the particular case of a sail oriented perpendicular to the Sun - line, when the system is Hamiltonian.

Finally, in Chapter 4 we describe the dynamics around different equilibrium points close to SL_1. We have computed the families of periodic orbits by means of a continuation method. We have also used the approximation to the centre manifold obtained in the previous chapter to have a description of the periodic and quasi-periodic motion in an extended neighbourhood of these equilibrium points. Around each of the equilibrium points we find families of planar and vertical periodic orbits related to the two frequencies defining the centre motion. Families of Halo - type orbits can also be found. The interaction between the two frequencies gives rise to families of invariant tori.

At the end of this dissertation we summarise the main results and point out some possible directions for future work.

Chapter 1

Solar Sails in the RTBP

1.1 Solar Sails

A *Solar Sail* is a new concept of spacecraft propulsion. The idea is to take advantage of the *solar radiation pressure* to produce momentum. We provide a small spacecraft with a solar sail: a large membrane mirror, made of a very light material and highly reflecting, so that the impact of the photons emitted by the Sun and its further reflection propel the spacecraft. Although the acceleration experienced is much smaller than the one achieved by a "traditional" thruster, this one acts in a continuous way, being able to continuously accelerate the spacecraft.

Why we should consider Solar Sails as an option is clear, they open a wide new range of possible mission applications that cannot be achieved by a conventional spacecraft. First of all, the source of energy is unlimited, so we can consider long term missions like exploring the Solar System. The further away the target planet is the more competitive a solar sail becomes, due to its continuous acceleration. Several studies have been done in this direction, some examples are [VdHM79, SRM04, HMM$^+$04].

Second, one can use a solar sail to remain in fixed locations high over the ecliptic plane, using the reflected sunlight to counteract the gravitational attraction of the Earth or any other planet. This mission concept was first introduced by Robert L. Forward [For90]. He proposes a mission to hover one of the Earth's poles with what he calls "Statite": a satellite that does not orbit. In the Section 1.3 we will see that the effect of a solar sail creates in the Earth - Sun system a family of artificial equilibria that can be used for very interesting mission applications. Some examples are the Geostrom Warning Mission [Wes04, MM04, Yen04], VIGIWING [PPP96] and the Polar Observer [McI03, MM04], all of them propose to maintain a spacecraft in a fixed location using a solar sail.

Finally, the cost of the spacecraft is low, giving the chance to small companies enter in the space industry.

Unfortunately, to the date, there has not been a successful deployment of a solar sail in space. Cosmos 1 was a project led by The Planetary Society and Cosmos Studios to test the first solar sail in space. The main goal of the mission was to successfully deploy a solar sail and raise its altitude through solar sailing. Any measurable increase in the spacecraft's orbit would have been considered a success. Cosmos 1 was launched in June 2005, but a rocket failure prevented it from reaching its intended orbit, and it was never possible to test a solar sail in space. In August 2008, NASA's Nano Sail followed the same faith. It was launched as a piggy-back payload on the Falcon launch vehicle. The goal was to deploy the sail and test the effect of the atmospheric drag on the sail, but the launch vehicle experienced a problem during stage separation and was unable to achieve an Earth orbit. Currently, The Planetary Society is working in collaboration with NASA and the Russian Space Research Institute to put together a new solar sail mission (Cosmos 2). For further details: `http://www.planetary.org/programs/projects/solar_sailing/`

1.1.1 Solar radiation pressure

The *solar radiation pressure* is the force exerted by the solar radiation on an object within its reach. It is of interest in astrodynamics, as it is a source of orbital perturbation. When we consider a solar sail, we want to take advantage of the solar radiation pressure to produce momentum on the spacecraft.

The pressure P exerted on the surface of the sail by the impact of the photons is defined as the momentum per unit of area and time. One can see [McI99] that it can be expressed in terms of the energy flux W divided by the speed of light c,

$$P = \frac{W}{c}. \tag{1.1}$$

The energy flux, W, is the rate of transfer of energy per unit of area. At a certain distance from the Sun, r, the energy flux can be written in term of the Sun's luminosity L_S and the Sun - Earth distance $R_E = 1AU$.

$$W = W_E \left(\frac{R_E}{r}\right)^2, \qquad \text{with} \qquad W_E = \frac{L_S}{4\pi R_E^2}. \tag{1.2}$$

Where W_E is the energy flux measured at the Earth's distance from the Sun. As the orbit of the Earth around the Sun is slightly elliptical, the energy flux received at the Earth

varies approximately 3.5%. An accepted mean value for this constant is 1368 J/m^2s.

Using equations (1.1) and (1.2) we have that the solar radiation pressure at $1AU$ from the Sun is $P = 4.56 \times 10^{-6} N/m^2$. For a perfectly reflecting sail, the observed pressure is twice this value, as the photons that impact on the surface of the sail are totally reflected. When this is not the case, we must add a coefficient ($\eta < 1$) related to the sail's reflectivity.

1.1.2 The force on a Solar Sail

A solar sail is an oriented surface, so the acceleration that it experiences is a function of the sail's area and orientation. The orientation is given by the normal direction to the surface of the sail ($\vec{n}$).

If we consider a perfectly reflecting sail, the angle of the incident photons with the surface of the sail is the same as the angle of the reflected photon with the surface of the sail, and the magnitude of force due to the incident and reflected photons is the same, see Figure 1.1. If the sail is not perfectly reflecting, the angles of the incident and reflected photons with the surface of the sail vary slightly, as well as the magnitude of their forces.

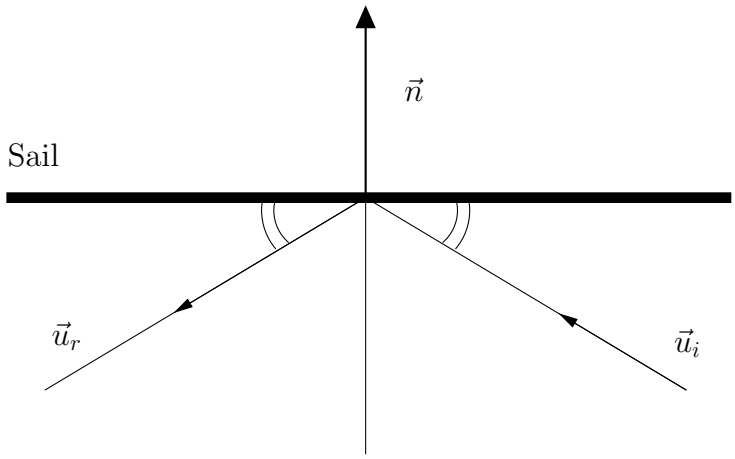

Figure 1.1: *Schematic representation of the impact and reflection of photons emitted by the Sun on the surface of a flat perfectly reflecting solar sail.*

In this work we focus on a flat, perfectly reflecting solar sail. Let A be the area of the sail. The force exerted on the surface of the sail due to incident photons from a direction $\vec{u}_i$ is given by,

$$\vec{F}_i = PA\langle \vec{u}_i, \vec{n} \rangle \vec{u}_i, \tag{1.3}$$

where $A\langle\vec{u}_i, \vec{n}\rangle$ is the projected area of the sail in the $\vec{u}_i$ direction and P is the solar radiation pressure. Similarly, the force due to the reflected photons in the direction $-\vec{u}_r$ is,

$$\vec{F}_r = -PA\langle\vec{u}_r, \vec{n}\rangle\vec{u}_r. \tag{1.4}$$

For a perfectly reflecting sail: $\vec{u}_i - \vec{u}_r = 2\langle\vec{u}_i, \vec{n}\rangle\vec{n}$. Then the total force exerted on the surface of the sail is,

$$\vec{F}_{sail} = \vec{F}_i + \vec{F}_r = 2PA\langle\vec{u}_i, \vec{n}\rangle^2\vec{n}. \tag{1.5}$$

Finally, combining equations (1.1), (1.2) and (1.5) the total force can be written as:

$$\vec{F}_{sail} = \frac{2AW_E R_E^2}{cr^2}\langle\vec{u}_i, \vec{n}\rangle^2\vec{n}. \tag{1.6}$$

If we are moving on heliocentric orbits, the direction of the incident photons $\vec{u}_i$ is given by the radial vector from the Sun to the sail ($\vec{r}$). Furthermore, the solar sail acceleration can be written in terms of the gravitational acceleration as:

$$\vec{a}_{sail} = \beta\frac{Gm_s}{r^2}\ \langle\vec{r}, \vec{n}\rangle^2\ \vec{n}, \tag{1.7}$$

where m_s is the mass of the Sun, G is the universal gravitational constant and β is a dimensionless parameter known as the lightness number of the sail.

Sail lightness number

The *sail lightness number*, β, is defined as the ratio of the solar radiation pressure acceleration to the solar gravitational acceleration, and it is usually used to describe the performance of a solar sail. Notice that both quantities, the solar radiation acceleration and the solar gravitational acceleration depend on the inverse square distance to the Sun. If we consider $\beta = 1$ the solar sail's force compensates the Sun's gravitational attraction, and if $\beta > 1$ the solar radiation pressure becomes the primary force and the Sun's gravitational attraction acts as a perturbation force. With the current technology, values of $\beta \approx 0.05$ are considered reasonable for a first mission application [MM04].

From equations (1.2) and (1.6) we can see that

$$\beta = \frac{\sigma^*}{\sigma}, \qquad \text{where} \qquad \sigma^* = \frac{L_S}{2\pi GM_s c} \approx 1.53 g/m^2. \tag{1.8}$$

Where σ is commonly known as the *sail loading parameter* and is a key parameter on the design of a solar sail. Now we can parametrise the performance of the solar sail by the

total mass of the spacecraft per unit of area $\sigma = m/A$. In Table 1.1 we have the relation between β and the sail loading parameter σ. As already mentioned, it is considered reasonable to take $\beta \approx 0.05$, which corresponds to a sail loading parameter $\sigma \approx 30 g/m^2$. Then, a $75m \times 75m$ square sail is required for a total spacecraft mass of $170kg$.

Characteristic acceleration

We define the *characteristic acceleration*, a_0, of a solar sail as the acceleration that a sail perpendicular to the Sun - sail line experiences at 1 AU from the Sun. Using equation (1.5), we have that the characteristic acceleration for a perfectly reflecting sail is:

$$a_0 = \frac{2PA}{m}.$$

If we consider a non-perfectly reflecting solar sail, we must add a reflectivity coefficient $\eta < 1$. In Section 1.1.1 we have seen that at $1AU$ from the Sun the solar radiation pressure $P = 4.56 \times 10^{-6}\ N/m^2$. Hence, the characteristic acceleration can be written as:

$$a_0 = \frac{9.17\eta}{\sigma}\ mm/s^2.$$

The characteristic acceleration is an equivalent design parameter to the sail loading σ, and is also used to describe the performance of a solar sail. In Table 1.1 we can see the relation between the parameters β, σ and a_0. For instance, if we consider a sail loading $\sigma \approx 30.6 g/m^2$, we have a characteristic acceleration $a_0 \approx 0.30 mm/s^2$.

β	0.02	0.04	0.05	0.06	0.1	0.2
σ(g/m^2)	76.50	38.25	30.6	25.50	15.30	7.65
a_0(mm/s^2)	0.12	0.24	0.30	0.36	0.59	1.19

Table 1.1: *Relation between the sail's lightness number (β), the sail loading parameter (σ) and the characteristic acceleration (a_0).*

1.1.3 Sail orientation

As we know, a solar sail is an orientable surface. As one can imagine, the sail orientation plays an important role in the spacecraft dynamics. Changes on the sail orientation change the magnitude of the force exerted by the sail and also the direction of the thrust.

Attitude techniques must be used to maintain a specific sail orientation [Wie04a, Wie04b] but this is not the goal of this work. From now on we will assume that we can maintain a given fixed sail orientation.

The orientation of the sail is defined in terms of the normal direction to the surface of the sail, parametrised by two angles α and δ. There are several ways to define these two angles [McI99, LP04, RRS05], and we can always find a change of variables to go from one definition to the other. From a dynamical point of view, this has a impact if we study the behaviour of the sail with a fixed orientation. Using one definition or the other the final output can be different.

We define these two angles as follows.

- α is the angle between the projection of the Sun - sail line and the normal vector to the sail ($\vec{n}$) on the ecliptic plane.
- δ is the difference between: a) the angle of the Sun - sail line with the ecliptic plane; and b) the angle of the normal vector $\vec{n}$ with the ecliptic plane.

In Figure 1.2 we have a graphic representation of these angles.

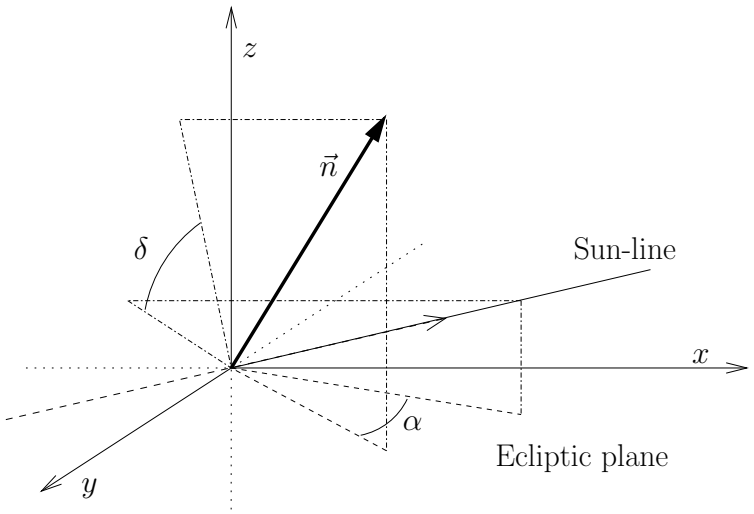

Figure 1.2: *Graphic description of the two angles (α, δ) that define the sail orientation.*

Notice that there are some limitations on the values of the two angles (α and δ) as the normal direction to the surface of the sail, $\vec{n}$, cannot point towards the Sun. In particular, if $\vec{r}_s$ represents the Sun - sail direction, then:

$$\langle \vec{r}_s, \vec{n} \rangle \geq 0. \tag{1.9}$$

1.2 The Restricted Three Body Problem for a Solar Sail

To describe the motion of a Solar Sail on the Earth - Sun system, we use the Restricted Three Body Problem for a Solar Sail (RTBPS). It is well known that the Restricted Three Body Problem (RTBP) considers the motion of an infinitesimal small particle, m, that is under the gravitational attraction of two bodies, m_1, m_2, called primaries [Sze67]. The two primaries orbit around their common centre of mass in a circular way and the gravitational attraction of the small particle on the two primaries is discarded. We take as the two primaries, Earth and Sun, and the small particle is a solar sail. Hence, we must also take into account the solar radiation pressure.

To simplify, we normalised the units mass, distance and time so that the total mass of the system is 1, the Sun - Earth distance is 1 and the period of their orbit is 2π. With these units, the gravitational constant G is also 1. Furthermore, we use a synodical or rotating reference system: the origin is taken at the centre of mass of both primaries, the X axis is given by the direction that goes from the Earth to the Sun, the Z axis is given by the direction of the angular variation of the primaries (i.e. perpendicular to the ecliptic plane), and finally, the Y axis is chosen to have an orthogonal positively oriented reference system. With this reference system the primaries remain fixed along time. The small primary of mass μ, is located at $(1-\mu, 0, 0)$ and the big primary of mass $1-\mu$, at $(\mu, 0, 0)$ (Figure 1.3). It is clear that the Earth is the small primary, and with this normalised units we have,

$$\mu = \mu_{SE} \approx 3.00348060100486 \times 10^{-6}.$$

We consider the sail to be flat and perfectly reflecting. Thus, the force due to the solar radiation pressure is in the normal direction to the surface of the sail (see Section 1.1.2). Using equation (1.7) we have that the acceleration due to the sail is given by,

$$\vec{a}_{sail} = \beta \frac{1-\mu}{r_{PS}^2} \langle \vec{r}_s, \vec{n} \rangle^2 \vec{n}. \tag{1.10}$$

Where β is the sail's lightness number, $\vec{n}$ is the normal direction to the surface to the sail, $\vec{r}_s$ is the Sun - sail direction and r_{PS} is the Sun - sail distance.

Using the same scheme as in [Sze67] for the RTBP, one can see that the equations of

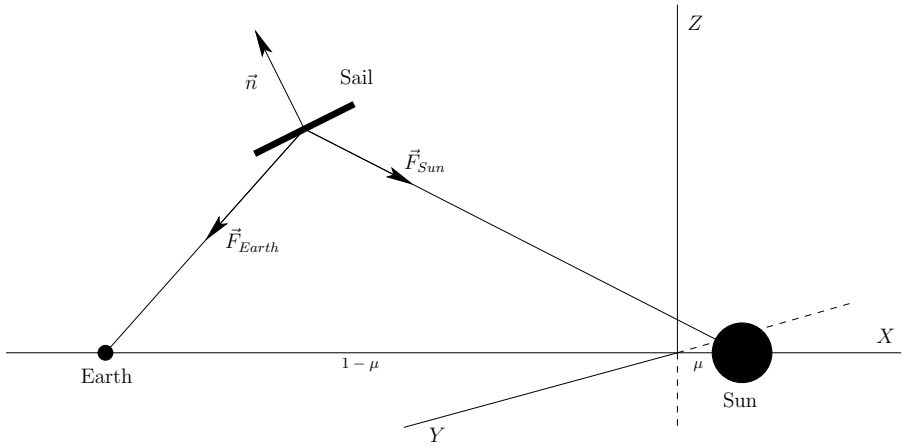

Figure 1.3: *Schematic representation of the position of the two primaries and the solar sail in the synodical reference system.*

motion of the RTBPS for a flat and perfectly reflecting solar sail are,

$$\begin{aligned}
\ddot{X} &= 2\dot{Y} + X - (1-\mu)\frac{X-\mu}{r_{PS}^3} - \mu\frac{X+1-\mu}{r_{PE}^3} + \beta\frac{1-\mu}{r_{PS}^2}\langle\vec{r}_s,\vec{n}\rangle^2 n_X, \\
\ddot{Y} &= -2\dot{X} + Y - \left(\frac{1-\mu}{r_{PS}^3} + \frac{\mu}{r_{PE}^3}\right) Y + \beta\frac{1-\mu}{r_{PS}^2}\langle\vec{r}_s,\vec{n}\rangle^2 n_Y, \qquad (1.11) \\
\ddot{Z} &= -\left(\frac{1-\mu}{r_{PS}^3} + \frac{\mu}{r_{PE}^3}\right) Z + \beta\frac{1-\mu}{r_{PS}^2}\langle\vec{r}_s,\vec{n}\rangle^2 n_Z,
\end{aligned}$$

where r_{PS} and r_{PE} denote the distances to the Sun and Earth respectively:

$$\begin{aligned}
r_{PS}^2 &= (X-\mu)^2 + Y^2 + Z^2, \\
r_{PE}^2 &= (X-\mu+1)^2 + Y^2 + Z^2,
\end{aligned}$$

and $\vec{r}_s = [\, X-\mu\ ,\ Y\ ,\ Z\,]/r_{PS}$ is the Sun - line direction. We take $\phi(X,Y)$ and $\psi(X,Y,Z)$ as

$$\phi(X,Y) = \arctan\left(\frac{Y}{X-\mu}\right), \qquad \psi(X,Y,Z) = \arctan\left(\frac{Z}{\sqrt{(X-\mu)^2+Y^2}}\right), \qquad (1.12)$$

the angles that define $\vec{r}_s$ in spherical coordinates. Then,

$$\vec{r}_s = [\, \cos(\phi(X,Y))\cos(\psi(X,Y,Z))\ ,\ \sin(\phi(X,Y))\cos(\psi(X,Y,Z))\ ,\ \sin(\psi(X,Y,Z))\,]\,.$$

Now, taking the two angles α and δ as defined in Section 1.1.3, the normal vector to the surface of the sail, $\vec{n} = [\ n_X\ ,\ n_Y\ ,\ n_Z\ ]$, satisfies:

$$\begin{aligned} n_X &= \cos(\phi(X,Y)+\alpha)\cos(\psi(X,Y,Z)+\delta), \\ n_Y &= \sin(\phi(X,Y)+\alpha)\cos(\psi(X,Y,Z)+\delta), \\ n_Z &= \sin(\psi(X,Y,Z)+\delta). \end{aligned} \tag{1.13}$$

One can check that here the projected area of the surface of the sail is:

$$\langle \vec{r}_s, \vec{n} \rangle^2 = \left[\frac{(r_2^2 \cos\alpha + Z^2)\cos\delta + Z r_2 (1-\cos\alpha)\sin\delta}{r_{PS}^2} \right]^2, \tag{1.14}$$

with $r_2 = \sqrt{(X-\mu)^2 + Y^2}$.

Hence, for a fixed sail orientation this quantity can vary with the position of the sail. Notice, that it is always zero when $\vec{r}_s \perp \vec{n}$ (e.g. $\delta = \pi/2$ and $\alpha = 0$). So, if $\beta = 0$ or $\vec{r}_s \perp \vec{n}$, the sail effect is discarded and we have the RTBP. If $\alpha = \delta = 0$, the sail is perpendicular to the Sun - line and it takes its maximum value $\langle \vec{r}_s, \vec{n} \rangle = 1$.

It is well know that the RTBP can be expressed as a Hamiltonian system by introducing the momenta: $P_X = \dot{X} - Y$, $P_Y = \dot{Y} + X$, $P_Z = \dot{Z}$. Unfortunately, when the solar radiation pressure is added, this only holds for a small set of sail orientations: when the sail is aligned with respect to the Sun - sail ($\vec{r}_s \perp \vec{n}$) and when the sail is perpendicular to the Sun - sail ($\vec{r}_s \parallel \vec{n}$). In the first case the effect of the sail is discarded, and in the second case, the system presents some similarities with the RTBP (essentially we are slightly changing the Sun's gravitational attraction). For further details see Appendix B.

For the other sail orientations, the system is no longer Hamiltonian, but it is still conservative (in the sense that the Lebesgue measure is preserved by the flow). For the particular case $\alpha = 0$ and δ free (i.e. the sail only admits vertical oscillations with respect to the Sun - sail line) the system is also time reversible by

$$R : (t, X, Y, Z, \dot{X}, \dot{Y}, \dot{Z}) \mapsto (-t, X, -Y, Z, -\dot{X}, \dot{Y}, -\dot{Z}).$$

Hence, under certain constraints on the equilibrium points the system behaves locally as a Hamiltonian system [LR98]. In Chapter 4, we study in more detail this particular case.

1.3 Family of Equilibrium Points

It is well known that the RTBP has 5 equilibrium points $L_{1,\dots,5}$: three of them, $L_{1,2,3}$, lay on the X axis and are known as Euler points or collinear points; the other two, $L_{4,5}$, are the third vertex of two equilateral triangle on the plane using the two primaries as vertices, and are known as Lagrangian points or triangular points.

When the effect due to the solar sail is introduced the system has new families of equilibrium solutions, sometimes referred to as surfaces of "artificial" equilibria [MMSM94, McI99]. The five equilibrium points on the RTBP are the positions in the phase space where the gravitational attraction of both primaries compensates. When we add the effect of the solar sail, we have an extra force that can be oriented freely (under certain constraints) and allows to have 2D families of new equilibrium points, parametrised by the sail orientation. For example, we can find equilibria above the ecliptic plane by orienting the sail so that it compensates the Earth's gravitational attraction.

If we consider the particular case of a solar sail perpendicular to the Sun - sail direction, the Sun gravitational attraction and the sail acceleration are in opposite directions. Hence, we also have 5 equilibrium points: three of them lay on the X axis, we call them $SL_{1,2,3}$, and are displaced closer to the Sun than $L_{1,2,3}$. The other two, that we call $SL_{4,5}$, form a triangle with the two primaries, defined by the constraint $r_{PS} = (1-\beta)^{1/3}, r_{PE} = 1$. We can see that the larger the sail performance is, the closer the equilibrium points are to the Sun. When $\beta \to 1$ the equilibrium points SL_1, SL_3, SL_4 and SL_5 tend to the Sun, while SL_2 moves towards the Earth. For further details see Appendix B.

As we know, the equilibrium solutions appear when the velocities and accelerations at a certain position are zero. Taking equation (1.11) we have that these points must satisfy:

$$\begin{aligned} -X + (1-\mu)\frac{X-\mu}{r_{PS}^3} + \mu\frac{X+1-\mu}{r_{PE}^3} &= \beta\frac{1-\mu}{r_{PS}^2}\langle\vec{r}_s,\vec{n}\rangle^2 n_X, \\ -Y + \left(\frac{1-\mu}{r_{PS}^3} + \frac{\mu}{r_{PE}^3}\right)Y &= \beta\frac{1-\mu}{r_{PS}^2}\langle\vec{r}_s,\vec{n}\rangle^2 n_Y, \\ \left(\frac{1-\mu}{r_{PS}^3} + \frac{\mu}{r_{PE}^3}\right)Z &= \beta\frac{1-\mu}{r_{PS}^2}\langle\vec{r}_s,\vec{n}\rangle^2 n_Z. \end{aligned} \tag{1.15}$$

Notice that the left - hand side of the equality is the gradient of the potential of the classical RTBP,

$$\Omega(X,Y,Z) = \frac{1}{2}(X^2+Y^2) + \frac{(1-\mu)}{r_{PS}} + \frac{\mu}{r_{PE}}.$$

So, the equilibrium points must satisfy:

$$-\nabla\Omega = \beta\frac{1-\mu}{r_{PS}^2}\langle\vec{r}_s,\vec{n}\rangle^2\vec{n}.$$

Hence, we can have an equilibrium point at (X, Y, Z) if the sail orientation in this position is parallel to $\nabla\Omega$ and has the appropriate magnitude.

For a fixed small β there are 5 continuous families of equilibria, parametrised by the sail orientation α and δ. Each one containing one of the 5 Lagrangian equilibrium points. As β increases, these five families merge with each other, and the families of equilibria are in 2 disconnected surfaces Σ_1 and Σ_2: the surface Σ_1 is like a torus centred around the Sun, containing L_1, L_3, L_4 and L_5; the surface Σ_2 is like a sphere placed at the left - hand side of Earth and contains L_2. As β increases, the inner radius of the torus Σ_1 decreases, vanishing for $\beta = 1$. For $\beta > 1$, the surfaces Σ_1 are like a cylinder [MMSM94, McI99]. Anyway, it is not realistic to consider $\beta > 1$ as we would mean we have a sail with a force greater than the Sun's gravitational attraction. For this reason, from now on we will consider $\beta \in [0, 1]$. For an easy illustration, sections of these surfaces on the XY and XZ planes are shown.

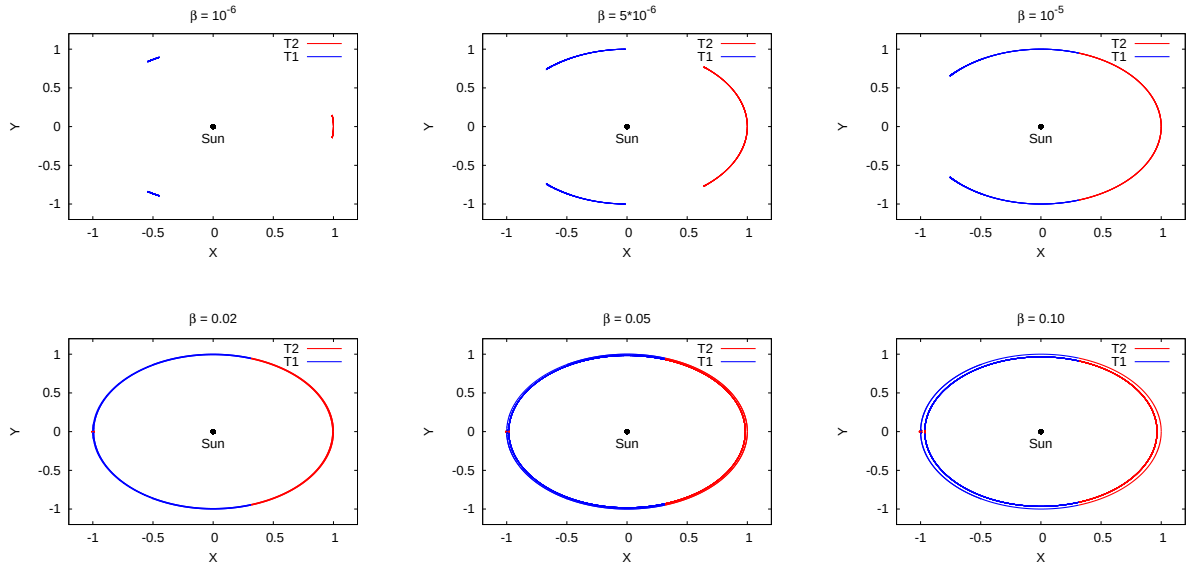

Figure 1.4: *Sections on the XY plane of the surfaces of equilibria for different fixed values of β. In blue fixed points of class $\mathcal{T}_1$ and in red fixed points of class $\mathcal{T}_2$. From left to right, top to bottom $\beta = 10^{-6}, 5\times10^{-6}, 10^{-5}, 0.02, 0.05, 0.1$.*

In Figure 1.4 we can see the evolution of these surfaces of equilibria on the XY plane for $\beta = 10^{-6}, 5\times10^{-6}, 10^{-5}, 0.02, 0.05, 0.1$. We can observe that as β increases, these families

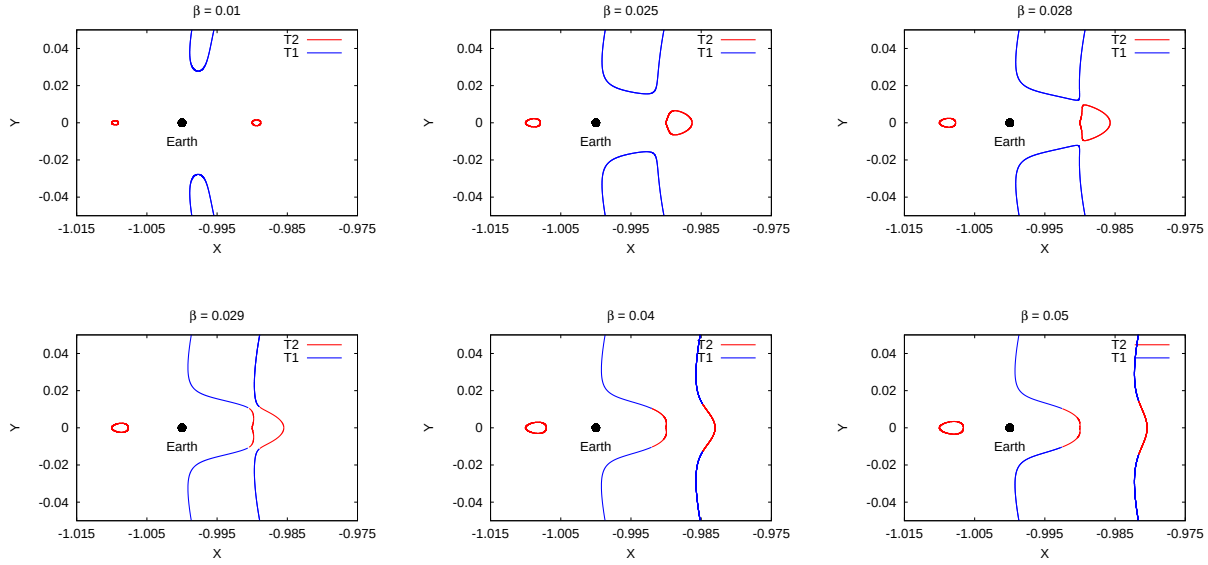

Figure 1.5: *Sections on the XY plane of the surfaces of equilibria for different fixed values of β. In blue fixed points of class $\mathcal{T}_1$ and in red fixed points of class $\mathcal{T}_2$. From left to right, top to bottom $\beta = 0.01, 0.025, 0.028, 0.029, 0.04, 0.05$.*

merge into each other. In Figure 1.5 we have a more detailed vision on the region close to the Earth for $\beta = 0.01, 0.025, 0.028, 0.029, 0.04, 0.05$, where we can see when the surfaces of equilibria merge into each other between $\beta = 0.028$ and $\beta = 0.029$. In Figure 1.6 we have the $\{X, Z\}$ section of these surfaces of equilibria for $\beta = 0.02, 0.04, 0.06, 0.08, 0.1$.

The colours in Figures 1.4, 1.5 and 1.6 are related to the stability properties of the equilibrium point. The equilibrium points in blue (class $\mathcal{T}_1$) have three complex eigenvalues, and as we will discuss later on, most of them are practically stable, as the rate of escape due to the real part of the eigenvalues is very small. The equilibrium points in red (class $\mathcal{T}_2$) are unstable and have a pair of real eigenvalues and two pairs of complex ones. This is discussed in more detail in Section 1.4.

In Section 1.1.3 we mentioned that there are some limitation on the sail orientation. It is physically understood that the sail acceleration, and so the sail orientation ($\vec{n}$) can never be directed towards the Sun, hence $\langle \vec{r}_s, -\nabla\Omega \rangle \geq 0$. This condition gives a boundary for the existence of equilibria, given by the condition $S(X, Y, Z) = 0$, where

$$\mathcal{S}(X, Y, Z) = X(X - \mu) + Y^2 - \frac{1 - \mu}{r_{PS}} - \mu \frac{(X - \mu)(X - \mu + 1) + Y^2 + Z^2}{r_{PE}^3}. \tag{1.16}$$

The function $\mathcal{S} = 0$ has two topological disconnected surfaces $\mathcal{S}_1$ and $\mathcal{S}_2$, that define the boundary of the existence of equilibrium solutions. The surface $\mathcal{S}_1$ is topologically

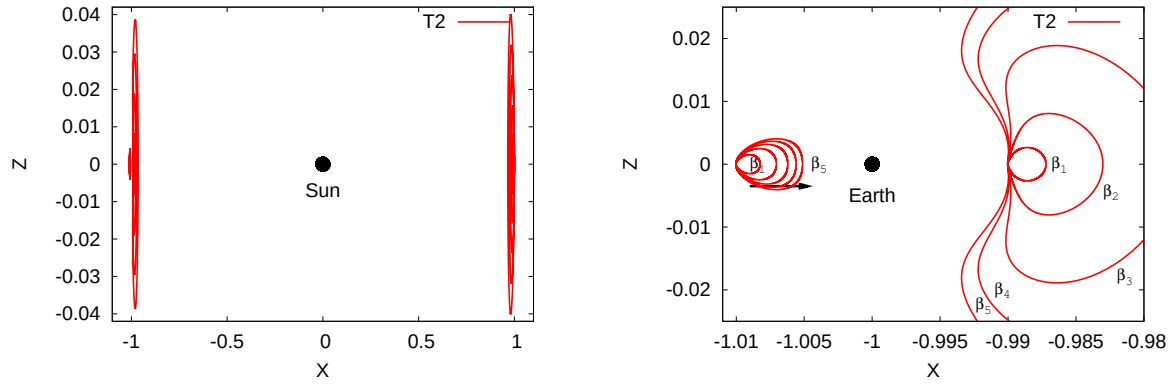

Figure 1.6: *Sections on the XZ plane of the surfaces of equilibria for different fixed values of β. All the equilibrium points are of class $\mathcal{T}_2$. On the right a zoom close to the Earth. Here $\beta_1 = 0.02, \beta_2 = 0.04, \beta_3 = 0.06, \beta_4 = 0.08, \beta_5 = 0.1$.*

equivalent to a cylinder, separating on the plane the motion for $X < L_2$ and $X > L_3$. The surface $\mathcal{S}_2$ is topologically equivalent to a sphere, and excludes the region between L_1 and the Earth. All of the five classical equilibrium points $L_{1,\ldots,5}$ lay on $\mathcal{S}_1 \cup \mathcal{S}_2$, and the rest of the equilibria lay in the interior of these surfaces. In general, the surfaces of equilibria for a fixed β tend to these boundaries as $\beta \to \infty$ [MMSM94, McI99].

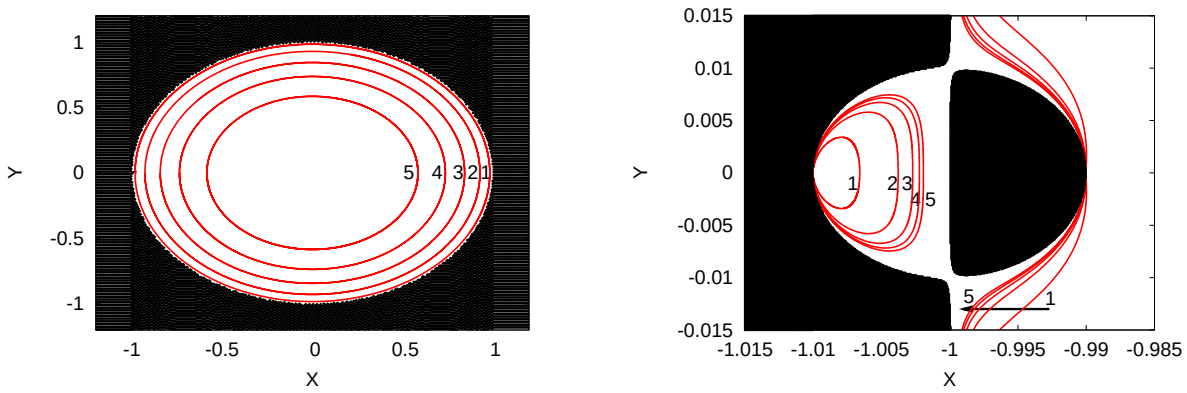

Figure 1.7: *Regions of the existence of equilibria on the XY plane. On the right a zoom close the Earth. In black: the forbidden regions for equilibria. In red: families of equilibrium points for different values of β. From 1 to 5: $\beta = 0.05, 0.2, 0.4, 0.6, 0.8$.*

In Figures 1.7 and 1.8 we can see the surfaces of equilibria on a section in the XY plane and the XZ plane respectively. In both figures we also show sections of the surfaces of equilibria for different β. In both pictures we have $\beta = 0.05, 0.2, 0.4, 0.6, 0.8$.

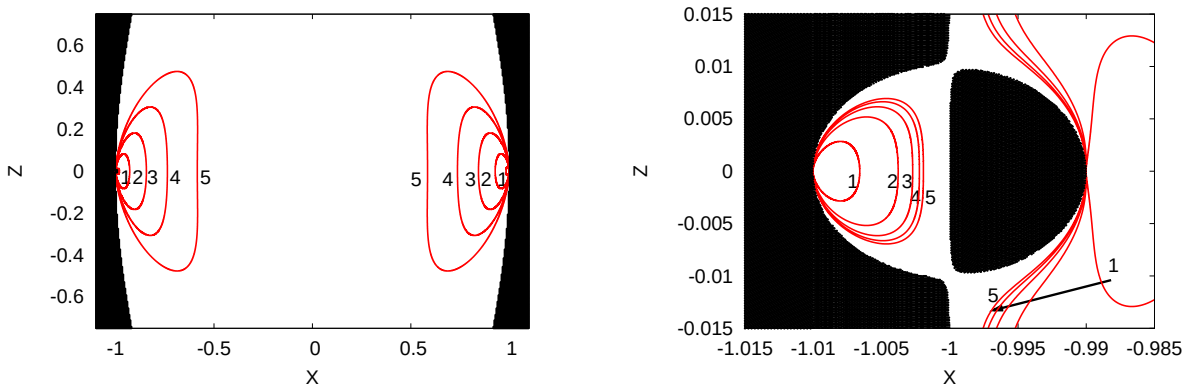

Figure 1.8: *Regions of the existence of equilibria on the XZ plane. On the right a zoom close to the Earth. In black: the forbidden regions for equilibria. In red: families of equilibrium points for different values of β. From 1 to 5: $\beta = 0.05, 0.2, 0.4, 0.6, 0.8$.*

1.4 Stability of Equilibrium Points

Once we have discussed the existence of the artificial equilibria we want to examine their stability. In general, the equilibrium points are unstable [MMSM94, McI99]. Nevertheless, as we will see, in some cases the rate of escape is very mild, having regions of practical stability.

We classify the equilibrium points (p_0) by the eigenvalues of the linearisation of the flow on the equilibrium points, $D_X f(p_0)$. Here we can find three different classes of equilibrium points:

- $\mathcal{T}_1$: $D_X f$ has three pairs of complex eigenvalues ($\nu_1 \pm \mathrm{i}\,\omega_1$, $\nu_2 \pm \mathrm{i}\,\omega_2$ and $\nu_3 \pm \mathrm{i}\,\omega_3$).
- $\mathcal{T}_2$: $D_X f$ has one pair of real eigenvalues ($\lambda_{1,2} \in \mathbb{R}$ with $\lambda_1 > 0$ and $\lambda_2 < 0$) and two pairs of complex eigenvalues ($\nu_1 \pm \mathrm{i}\,\omega_1$ and $\nu_2 \pm \mathrm{i}\,\omega_2$).
- $\mathcal{T}_3$: $D_X f$ has two pairs of real eigenvalues $\lambda_{1,\ldots,4} \in \mathbb{R}$ with $\lambda_1, \lambda_3 > 0$ and $\lambda_2, \lambda_4 < 0$) and one pair of complex eigenvalues ($\nu_1 \pm \mathrm{i}\,\omega_1$).

Notice that as the flow has zero divergence, the sum of all the eigenvalues must be zero. Then: $2(\nu_1 + \nu_2 + \nu_3) = 0$ for the class $\mathcal{T}_1$ of fixed points; $\lambda_1 + \lambda_2 + 2(\nu_1 + \nu_2) = 0$ for the class $\mathcal{T}_2$; and $\lambda_1 + \lambda_2 + \lambda_3 + \lambda_4 + 2\nu_1 = 0$ for the class $\mathcal{T}_3$.

For the particular cases of a perpendicular solar sail ($\alpha = \delta = 0$) the system is Hamiltonian, then the eigenvalues must come in pairs: if λ is an eigenvalue, then so are $-\lambda$ and $\bar{\lambda}$. Moreover, if $\alpha = 0$ the system is time reversible and three of the five $1D$ families of equilibrium points that appear share this same property due to the reversibility

of the model [Sev86, LR98]. We discuss this particular case in more detail in Section 4.1. For the rest of the cases ($\alpha \neq 0$) this restriction on the eigenvalues does not apply.

In Figures 1.4, 1.5 and 1.6 the fixed points of class $\mathcal{T}_1$ are represented in blue and the ones of class $\mathcal{T}_2$ are represented in red. The equilibrium points of class $\mathcal{T}_3$ are found above the ecliptic plane for large values of β [WM07].

In what follows we discuss in more detail the stability in a small neighbourhood of SL_i for $i = 1, \ldots, 5$ for $\beta = 0.05$. We have taken a set of fixed points close to each of them and computed their stability. In Figures form 1.9 to 1.13 we plot the values of the 3 pairs of eigenvalues for each of the equilibrium points in the region close to the SL_i. If one of the pairs is a complex eigenvalue ($\nu \pm \mathrm{i}\,\omega$) we just represent $\nu + \mathrm{i}\,\omega$, and if we have a pair of two real eigenvalues ($\lambda_{1,2}$) we just represent $\lambda_1 > 0$, as $\lambda_2 < 0$ is close to $-\lambda_1$. Finally, Figure 1.14 shows the $2D$ surfaces of equilibria close to the different SL_i that has been studied. Where a colour is associated to each point depending on its linear dynamics.

In Figure 1.9 we show the eigenvalues of a 2D family of fixed points close to SL_1. We can see that there is always a pair of real eigenvalues, $\lambda_1 > 0, \lambda_2 < 0$, and two pairs of complex eigenvalues $\nu_{1,2} \pm \mathrm{i}\,\omega_{1,2}$. Notice that, although in most cases $\nu_{1,2} \neq 0$, this one is very small compared to $|\lambda_{1,2}|$. In particular $|\nu_{1,2}| < 0.0015$ and $|\lambda_{1,2}| > 0.8$. Hence, close to SL_1 the main instability is given by the real eigenvalues. On the top left corner of Figure 1.14 we have the $3D$ representation of the surface of equilibria taken for the previous plots. Each point is associated with a colour depending on the eigenvalues. Red is for those equilibrium points where $\nu_{1,2} > 0$, green for those where $\nu_{1,2} < 0$ and blue for those with $\nu_{1,2} = 0$. Notice that the $Y = 0$ plane separates the two types of motions: at $Y > 0$ the trajectories spiral inwards, while for $Y < 0$ the trajectories spiral outwards. For $Y = 0$ we have $\nu_{1,2} = 0$.

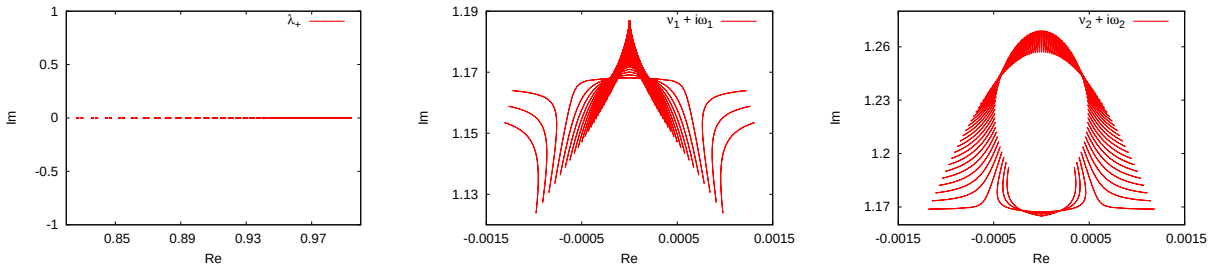

Figure 1.9: *Three of the six eigenvalues for different equilibrium points close to SL_1 for $\beta = 0.05$: $\lambda_1 > 0$ (left), $\nu_1 + \mathrm{i}\,\omega_1$ (middle) and $\nu_2 + \mathrm{i}\,\omega_2$ (right).*

In Figure 1.10 we have the eigenvalues of a 2D family of fixed points close to SL_2. As in the neighbourhood of SL_1, we also find two real eigenvalues, $\lambda_1 > 0, \lambda_2 < 0$, and two

pair of complex eigenvalues $\nu_{1,2} \pm \mathrm{i}\,\omega_{1,2}$, with $|\nu_{1,2}| < 8 \times 10^{-5}$ and $|\lambda_{1,2}| > 4$. The spiralling effect is almost negligible for short times. On the top right corner of Figure 1.14 we have the 3D representation of the surface of equilibria considered in the previous plots. The same criteria as before has been applied to paint each of the equilibrium points. Again, the $Y = 0$ plane separates the two different type of motions. For $Y > 0$ the trajectories spiral inwards in the centre projection, while they spiral outwards for $Y < 0$. For $Y = 0$ we have $\nu_{1,2} = 0$.

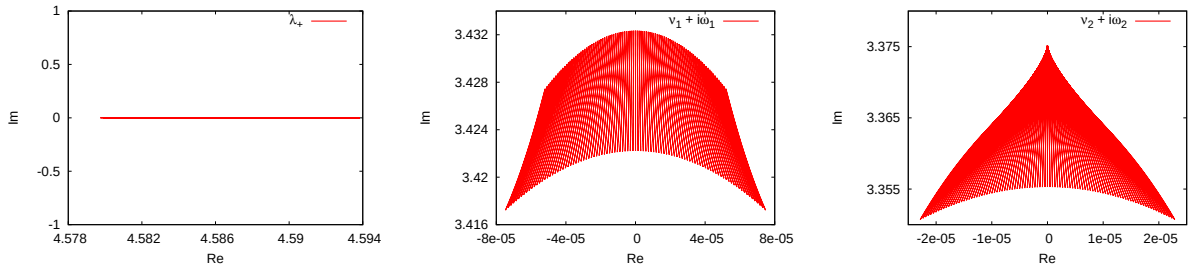

Figure 1.10: *Three of the six eigenvalues for different equilibrium points close to SL_2 for $\beta = 0.05$: $\lambda_1 > 0$ (left), $\nu_1 + \mathrm{i}\,\omega_1$ (middle) and $\nu_2 + \mathrm{i}\,\omega_2$ (right).*

In Figure 1.11 we find the eigenvalues for the fixed points close to SL_3. Again, we have two real eigenvalues, $\lambda_1 > 0, \lambda_2 < 0$, and two pair of complex eigenvalues $\nu_{1,2} \pm \mathrm{i}\,\omega_{1,2}$, with $|\nu_{1,2}|$ very small, less that 6×10^{-7}. Notice that the instability given by the real eigenvalues is very mild, as $|\lambda_i| < 0.003$. In the middle of Figure 1.14 we see the 3D representation of equilibrium points considered here, following the same colour criteria as before. We can also see that the $Y = 0$ plane separates the two types of motion.

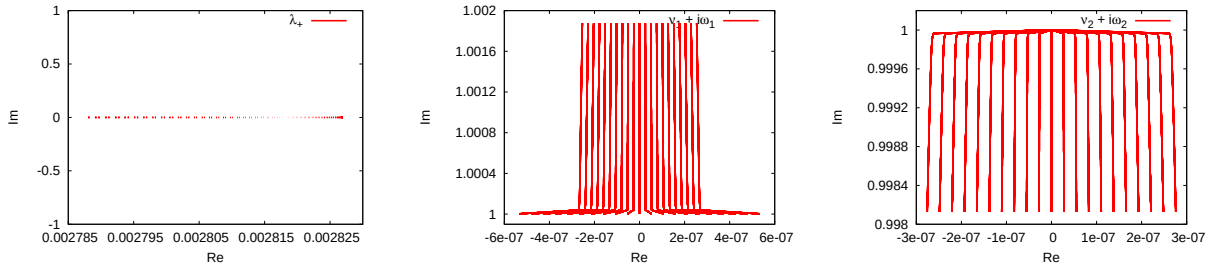

Figure 1.11: *Three of the six eigenvalues for different equilibrium points close to SL_3 for $\beta = 0.05$: $\lambda_1 > 0$ (left), $\nu_1 + \mathrm{i}\,\omega_1$ (middle) and $\nu_2 + \mathrm{i}\,\omega_2$ (right).*

Finally Figures 1.12 and 1.13 show eigenvalues for families of equilibrium points close to SL_4 and SL_5 respectively. Now there are three pair of complex eigenvalues $\nu_{1,2,3} \pm \mathrm{i}\,\omega_{1,2,3}$,

with $\nu_{1,2,3} \neq 0$ but small. Notice that here $|\nu_{1,2,3}| < 6 \times 10^{-7}$, so the rate of escape is extremely small (it would take the sail about 183863 years to double its distance to the fixed point). So these regions are of practical stability for a probe. On the bottom of Figure 1.14 we see the 3D representation of equilibrium points close to SL_4 (left) and SL_5 (right). Here green is for those equilibrium points whose linear dynamics is a cross product of two outwards spirals and one inwards, and the blue for those points with one outward spiral and two inwards.

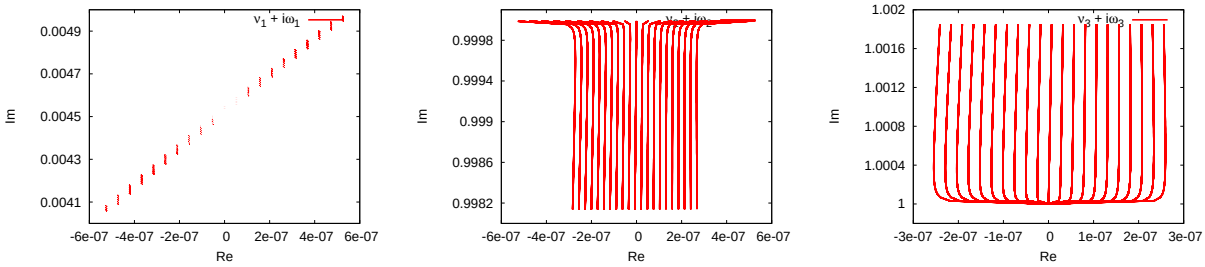

Figure 1.12: *Three of the six eigenvalues for different equilibrium points close to* SL_4 *for* $\beta = 0.05$*:* $\nu_1 + \mathrm{i}\,\omega_1$ *(left),* $\nu_2 + \mathrm{i}\,\omega_2$ *(middle) and* $\nu_3 + \mathrm{i}\,\omega_3$ *(right).*

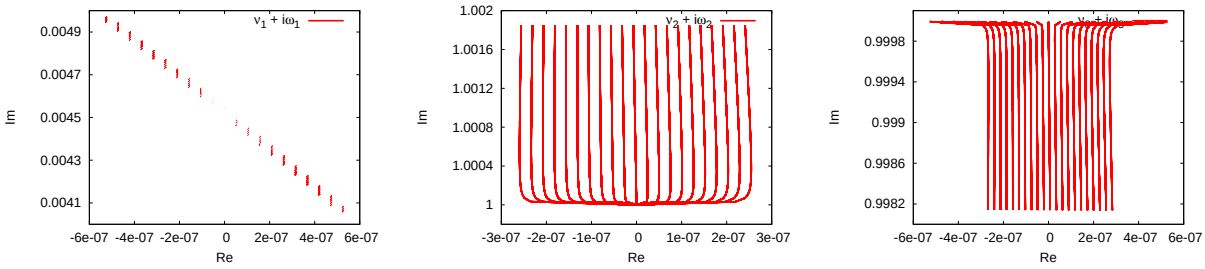

Figure 1.13: *Three of the six eigenvalues for different equilibrium points close to* SL_5 *for* $\beta = 0.05$*:* $\nu_1 + \mathrm{i}\,\omega_1$ *(left),* $\nu_2 + \mathrm{i}\,\omega_2$ *(middle) and* $\nu_3 + \mathrm{i}\,\omega_3$ *(right).*

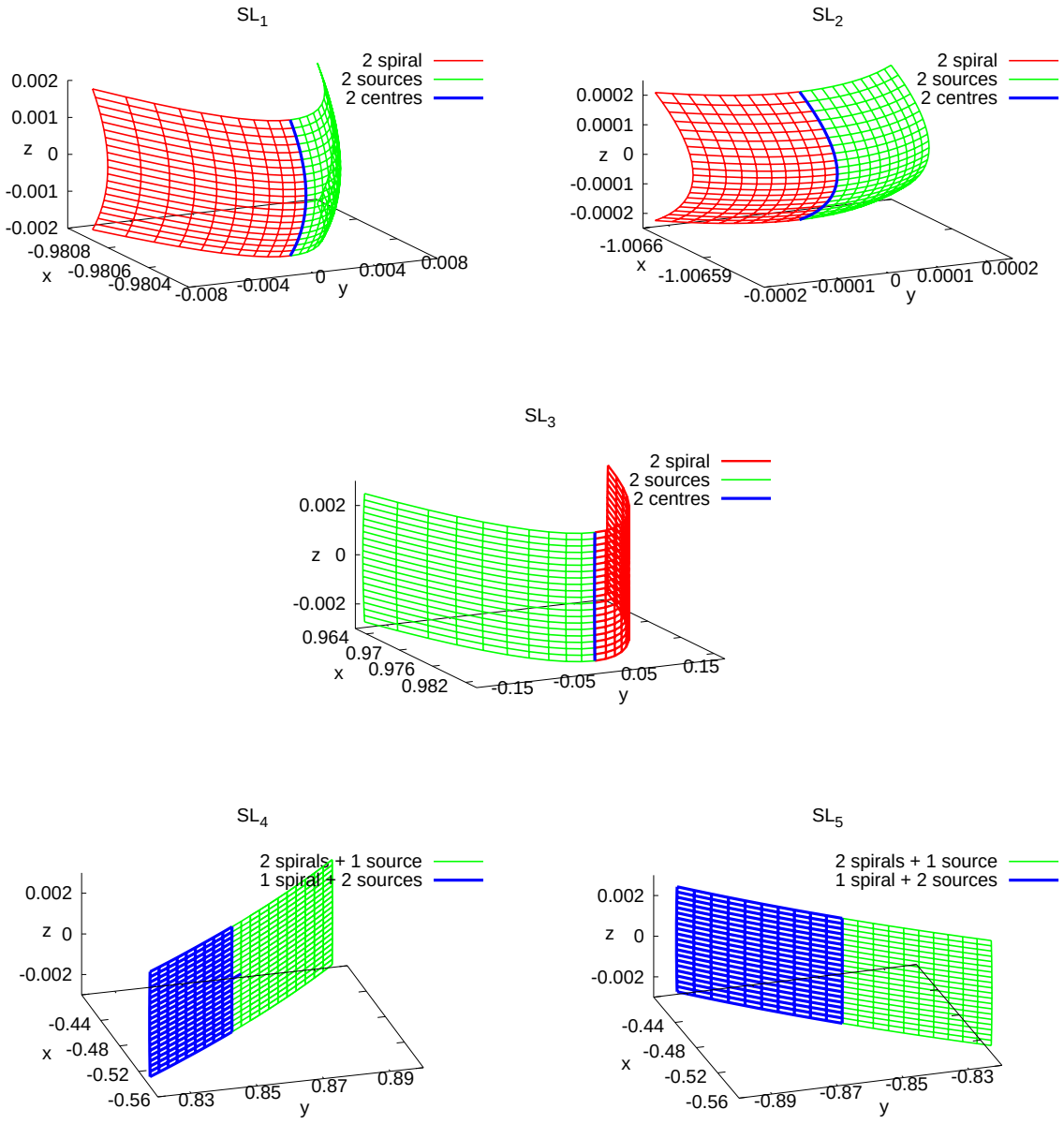

Figure 1.14: *Regions of fixed points close to SL_i for $i = 1, \ldots, 5$ and $\beta = 0.05$. From left to right, top to bottom: SL_1, SL_2, SL_3, SL_4 and SL_5.*

Chapter 2

Station Keeping Strategies Around Equilibria

In Chapter 1 we have seen that the effect of the solar radiation pressure on the Restricted Three Body Problem adds to the model a 2D family of equilibria parametrised by the sail orientation. These new equilibrium points open a wide range of possible mission applications that cannot be achieved by a conventional spacecraft. For example, we can place a spacecraft at an equilibrium point closer to the Sun than L_1, or maintain a satellite on a fixed location above the ecliptic plane.

We have also seen that most of these equilibrium points are unstable. According to [McI99], although the equilibrium solutions are in general unstable, they are controllable using either a feedback control to the sail attitude or trims of the sail area. In this Chapter we will discuss strategies for the station keeping of a solar sail around an equilibrium point. To derive such strategies we will use Dynamical System tools instead of Control Theory algorithms.

In Section 1.4 we have mentioned that the equilibrium points can be classified by their linear stability. From now on, we focus on the motion close to a linearly unstable equilibrium point of the class $\mathcal{T}_2$. We recall that these equilibrium points have two real eigenvalues $\lambda_1 > 0,\ \lambda_2 < 0$, and two pair of complex eigenvalues $\nu_{1,2} \pm \mathrm{i}\,\omega_{1,2}$. We will focus on those points where $|\nu_{1,2}| << |\lambda_{1,2}|$, so the instability of the region is mainly given by the real eigenvalues. As we have seen in Section 1.4 this holds for the equilibrium points close to SL_1 and SL_2.

Our aim is to use the information of the local dynamics to design strategies that maintain the trajectory of a sail close to an equilibrium point. We need to understand how the phase space varies when the sail orientation changes and find a way to make the

phase space act in our favour.

In Sections 2.1 we start by describing the local dynamics around an equilibrium point and how it varies when the sail orientation is changed. In Section 2.2 we describe the station keeping strategy that we have designed. We have tested our strategy on two different missions: The Geostorm Warning mission and Polar Observer mission. In Section 2.3 we discuss these results. Furthermore, in Section 2.4 we test the robustness of our strategies by introducing systematic errors on the position and velocity determination of the probe's trajectory as well as on the accuracy of the sail's orientation.

Finally, in Section 2.5 we present a way to move along a family of equilibrium points in a controlled way, using the local information of the variation of the phase space.

2.1 Preliminaries

When we are close to an equilibrium point, the dynamics is approximated by the linearisation of the equations of motion at this point. In Section 1.4 we can see that close to $SL_{1,2}$ the fixed points satisfy $|\nu_{1,2}| << |\lambda_{1,2}|$ and $|\lambda_1| \approx |\lambda_2|$. So, the main instability of the region is given by the positive real eigenvalue, and for short time spans, the rate of escape due to the complex eigenvalues is negligible. As a first approximation, we assume that $\nu_{1,2} = 0$ and $\lambda_2 = -\lambda_1$. Hence, the linear dynamics is of the type saddle $\times$ centre $\times$ centre.

Note that, if ν_1 or ν_2 are negative, our assumption adds extra complexity to the problem, as these directions are contracting. On the other hand, if ν_1 or ν_2 are positive, the probe may escape due to the effect of this expansion. In any case, we also try to decrease the centre behaviour. If this decreasing is bigger than the increasing factor due to ν_1 or ν_2, then the sail will be able to keep its trajectory close to the desired fixed point.

Let us call p_0 a fixed point for $\alpha = \alpha_0$ and $\delta = \delta_0$. From now on we describe the trajectory of the probe by its projection on three different 2D planes centred on p_0. The first plane is generated by the two eigenvectors related to the real eigenvalues ($\vec{v}_\lambda$, $\vec{v}_{-\lambda}$), where the saddle behaviour is described. The other two planes are generated by the real and imaginary part of the two pairs of complex eigenvectors ($\vec{v}_{\omega_i} \pm \mathrm{i}\,\vec{u}_{\omega_i}$ for $i = 1, 2$). The projection of the orbit on these two planes describes the central behaviour of the motion. Hence, we consider the reference system: $\{\ p_0;\ \vec{v}_\lambda, \vec{v}_{-\lambda}, \vec{v}_{\omega_1}, \vec{u}_{\omega_1}, \vec{v}_{\omega_2}, \vec{u}_{\omega_2}\ \}$ (see Figure 2.1).

In this reference system, when the sail is close to p_0 it escapes along the unstable direction ($\vec{v}_\lambda$) and rotates around the fixed point in the two centre projections. If we change the sail orientation then the fixed point, the eigenvalues and the eigenvectors vary.

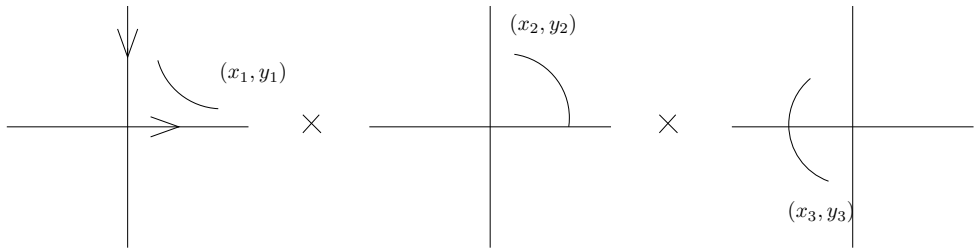

Figure 2.1: *Schematic representation of the trajectory of the sail in the* $\{ p_0;\ \vec{v}_\lambda, \vec{v}_{-\lambda}, \vec{v}_{\omega_1}, \vec{u}_{\omega_1}, \vec{v}_{\omega_2}, \vec{u}_{\omega_2} \}$ *reference system.*

Now the trajectory escapes along the new unstable direction. We want to change the sail orientation so that the unstable direction of this new fixed point sends the probe back to the neighbourhood of p_0. Once the probe is close to p_0, we restore the initial sail orientation and so on. This is graphically represented in Figure 2.2.

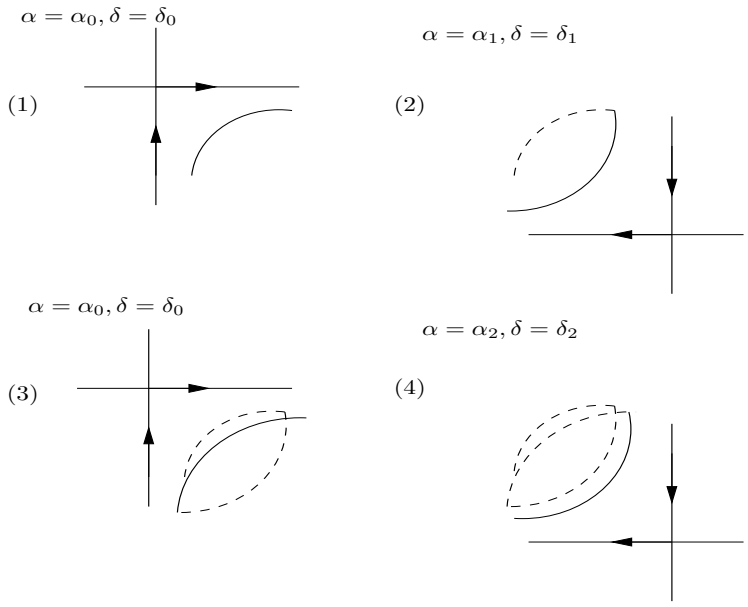

Figure 2.2: *Scheme of the idea to control the saddle instability around an equilibrium point.*

It is important to note that, during this process, the projection of the orbit on the central part of the equilibria can grow as the central behaviour is a sequence of rotations around each of the fixed points. The composition of central motions with different centre of rotation can result in an unbounded growth of motion. For this reason we have to be careful when we choose the new sail orientation. We have to control the instability given by the unstable direction and make sure that the two central projections do not grow.

Thus, we need to understand how the fixed points and eigenvectors change when we change the sail orientation, and see if there exists a new sail orientation that makes the sail's trajectory come close to p_0 and maintain the centre behaviour bounded. Notice that it is not obvious that there will always be an appropriate change of the sail orientation, as there are more unknowns than parameters to play with.

From now on, to simplify further formulations we consider $\vec{v}_1 = \vec{v}_\lambda$, $\vec{v}_2 = \vec{v}_{-\lambda}$, $\vec{v}_3 = \vec{v}_{\omega_1}$, $\vec{v}_4 = \vec{u}_{\omega_i}$, $\vec{v}_5 = \vec{v}_{\omega_2}$ and $\vec{v}_6 = \vec{u}_{\omega_2}$.

2.1.1 Variation of the phase space

We recall that we do not have an explicit expression for the position of an equilibrium point $p(\alpha, \delta)$. Nevertheless, as we deal with small changes on the sail's orientation, the linear approximation of these surfaces around a fixed point is enough. The same applies for the variation of the eigenvalues $\lambda_i(\alpha, \delta)$ and the eigenvectors $\vec{v}_i(\alpha, \delta)$.

Let us define $p_0 = p(\alpha_0, \delta_0)$ as the coordinates of the equilibrium point of $\dot{x} = f(x, \alpha, \delta)$, and let $\lambda_{i0} = \lambda_i(\alpha_0, \delta_0)$, $\vec{v}_{i0} = \vec{v}_i(\alpha_0, \delta_0)$ the eigenvalues and eigenvectors of $A_0 = D_x f(p_0, \alpha_0, \delta_0)$. Then,

$$p(\alpha, \delta) = p_0 + Dp \cdot h + o(||h||^2), \tag{2.1}$$

$$\lambda_i(\alpha, \delta) = \lambda_{i0} + D\lambda_i \cdot h + o(||h||^2), \tag{2.2}$$

$$\vec{v}_i(\alpha, \delta) = \vec{v}_{i0} + D\vec{v}_i \cdot h + o(||h||^2), \tag{2.3}$$

where,

$$Dp = \left[\frac{\partial p}{\partial \alpha}(\alpha_0, \delta_0) \quad \frac{\partial p}{\partial \delta}(\alpha_0, \delta_0)\right], \qquad Dv_i = \left[\frac{\partial \vec{v}_i}{\partial \alpha}(\alpha_0, \delta_0) \quad \frac{\partial \vec{v}_i}{\partial \delta}(\alpha_0, \delta_0)\right],$$

$$D\lambda_i = \left[\frac{\partial \lambda_i}{\partial \alpha}(\alpha_0, \delta_0) \quad \frac{\partial \lambda_i}{\partial \delta}(\alpha_0, \delta_0)\right] \qquad \text{and} \qquad h = \left[\alpha - \alpha_0 \quad \delta - \delta_0\right]^T.$$

If $|\alpha - \alpha_0| < \varepsilon_1$ and $|\delta - \delta_0| < \varepsilon_2$, with ε_1, ε_2 small enough, we can neglect the second order terms and just consider the linear approximation. Although we do not know explicitly these expressions, as we will see, it is not difficult to compute numerically Dp, $D\lambda$, $D\vec{v}$ for a given fixed point.

As we know, if p_0 are the coordinates of a fixed point for $\alpha = \alpha_0, \delta = \delta_0$, then

$f(p_0, \alpha_0, \delta_0) = 0$. By the Implicit Function Theorem, if $A_0 = D_x f(p_0, \alpha_0, \delta_0)$ is not singular, there exists a local expression for $p(\alpha, \delta)$ close to $(p_0, \alpha_0, \delta_0)$.

If we derive the equality, $f(p(\alpha_0, \delta_0), \alpha_0, \delta_0) = 0$ with respect to α and δ, then Dp satisfies:

$$\begin{aligned} A_0 \frac{\partial p}{\partial \alpha}(\alpha_0, \delta_0) + \frac{\partial f}{\partial \alpha}(p_0, \alpha_0, \delta_0) &= 0, \\ A_0 \frac{\partial p}{\partial \delta}(\alpha_0, \delta_0) + \frac{\partial f}{\partial \delta}(p_0, \alpha_0, \delta_0) &= 0. \end{aligned} \tag{2.4}$$

Notice that as A_0 is not singular we can solve these linear systems. Hence, we have an easy way to compute the linear variation of the fixed points with respect to the sail orientation (Dp).

The dependence of the eigenvalues and eigenvectors of a matrix with respect to parameters is a known topic that can be found in many places (for example, Chapter 2 of [Wil65]). Here we announce the main results we need to compute $D\lambda_i$ and $D\vec{v}_i$, for further details on the subject see [Wil65, Nel76, Lan64].

To fix notation: let us consider $A(\xi)$ an $n \times n$ matrix where its coefficients depend on a parameter $\xi \in \mathbb{R}$. In what follows, we assume that the elements of $A(\xi)$ are smooth in a neighbourhood of $\xi = \xi_0$. We call $\lambda_{i0} = \lambda_i(\xi_0)$ to the eigenvalues of $A_0 = A(\xi_0)$, $\vec{v}_{i0} = \vec{v}_i(\xi_0)$ to the right eigenvectors $(A_0\vec{v}_{0i} = \lambda_{i0}\vec{v}_{i0})$ and $\vec{u}_{i0} = \vec{u}_i(\xi_0)$ to the left eigenvectors $(\vec{u}_{i0}^T A_0 = \lambda_{i0}\vec{u}_{i0}^T)$ for $i = 1, \ldots, n$. Finally, let $D_\xi A(\xi)$ be the $n \times n$ matrix that have as elements the derivatives of the elements of $A(\xi)$ with respect to ξ.

Theorem 2.1.1 *Assume that $\lambda_{i0} = \lambda_i(\xi_0)$ is a simple eigenvalue with eigenvector $\vec{v}_{i0} = \vec{v}_i(\xi_0)$ of $A_0 = A(\xi_0)$; that A_0 diagonalises and that the elements of $A(\xi)$ are smooth in a neighbourhood of $\xi = \xi_0$.*

Then:

$$\frac{d\lambda_i}{d\xi}(\xi_0) = \frac{u_{i0}^T D_\xi A(\xi_0) v_{i0}}{u_{i0}^T v_{i0}}, \tag{2.5}$$

$$\frac{d\vec{v}_i}{d\xi}(\xi_0) = \sum_{k=0}^{n} c_k \vec{v}_k(\xi_0), \tag{2.6}$$

where the constants $c_k = \dfrac{u_k D_\xi A(\xi_0) v_i}{(\lambda_k - \lambda_i) u_k^T}$ for $k \neq i$ and $c_k = 1$ for $k = i$.

Notice that the coefficients c_k on equations (2.6) give the rate of variation of the eigen-

vectors in the eigenvector base. The details on the proof of this theorem can be derived from the explanations in [Wil65] or from the different results in [Nel76, Lan64].

Now taking $\xi = (\alpha, \delta)$ we can extend in an easy way equations (2.5) and (2.6) to compute $D\lambda_i(\alpha_0, \delta_0)$ and $D\vec{v}_i(\alpha_0, \delta_0)$.

2.1.2 An example

Let us consider one of the fixed points for $\beta = 0.05$ for a perpendicular sail orientation ($\alpha = 0, \delta = 0$); $SL_1 = p_0 = (\ -0.9804352, 0, 0, 0, 0, 0\ )$. We want to see how the phase space properties vary for small variations on the sail orientation.

Using equations (2.4) we compute Dp:

$$\begin{aligned} \frac{\partial p}{\partial \alpha}(0,0) &= [\ 0.0,\ -0.0127102,\ 0.0,\ 0.0,\ 0.0,\ 0.0\ ], \\ \frac{\partial p}{\partial \delta}(0,0) &= [\ 0.0,\ 0.0,\ 0.0036909,\ 0.0,\ 0.0,\ 0.0\ ]. \end{aligned} \tag{2.7}$$

Notice that up to first order, variations on α imply variations in the Y direction and variations on δ imply variations in the Z direction.

If we think of a station keeping strategy, our aim is to maintain the trajectory as close as possible to a given fixed point. We know that SL_1 is at a distance of ≈ 0.02AU from the Earth. From equality (2.7), one can check that at that distance an angular variation of $1.5°$ with respect to the Earth - SL_1 line give a variation of about $5.12 \times 10^{-4}\ AU = 76630.44\ km$ in position. Around SL_1 a variation on the sail orientation of about $0.23°$ in α or $0.79°$ in δ give variations of order 5×10^{-4} in the position of the fixed points. This is the magnitude of the maximum variation on the sail orientation that we should do to if we want to maintain an angular variation of the solar sail's trajectory less than $1.5°$.

Let us now check the linear dependence of the phase space properties around SL_1. Using equations (2.5) and (2.6) we have computed $D\lambda_i$ and $D\vec{v}_i$ for $i = 1, \ldots, 6$. In Table 2.1 we see the values of the eigenvalues and their variation with respect to the sail orientation. In Table 2.3 we see the eigenvectors and their variation with respect to the sail orientation expressed in the eigenvector base (i.e. $\partial\vec{v}_i/\partial\alpha = \sum_{j=1}^{6} c_{\alpha j}\vec{v}_j$, $\partial\vec{v}_i/\partial\delta = \sum_{j=1}^{6} c_{\delta j}\vec{v}_j$).

As we can see, the first order variation of the eigenvalues and eigenvectors is small. To get a better idea of the variation on the eigenvectors, we have computed the angles between $\vec{v}_i$ and $\partial\vec{v}_i/\partial\alpha$, and between $\vec{v}_i$ and $\partial\vec{v}_i/\partial\delta$ for $i = 1, \ldots, 6$, see Table 2.2. There we can see that the maximum variation is of the order of 0.03113684 rad. This behaviour

i	λ_i	$\partial\lambda_i/\partial\alpha$	$\partial\lambda_i/\partial\delta$
0	9.945411e-01	-2.065125e-02 + 0.000000e+00 i	0.000000e+00
1	-9.945411e-01	-2.065125e-02 + 0.000000e+00 i	0.000000e+00
2	1.256930e+00 i	2.065125e-02 - 2.773690e-18 i	0.000000e+00
3	-1.256930e+00 i	2.065125e-02 + 2.773690e-18 i	0.000000e+00
4	1.187114e+00 i	0.000000e+00 + 0.000000e+00 i	0.000000e+00
5	-1.187114e+00 i	0.000000e+00 + 0.000000e+00 i	0.000000e+00

Table 2.1: *For SL_1 and $\beta = 0.05$, the eigenvalues (λ_i) and their variation w.r.t. α ($\partial\lambda_i/\partial\alpha$) and δ ($\partial\lambda_i/\partial\delta$).*

i	$\langle\vec{v}_i, \partial\vec{v}_i/\partial\alpha\rangle$	angle	$\langle\vec{v}_i, \partial\vec{v}_i/\partial\delta\rangle$	angle
1	9.9951528761e-01	3.113684e-02	1.0000000000e+00	0.000000e+00
2	9.9951528761e-01	3.113684e-02	1.0000000000e+00	0.000000e+00
3	9.9969645328e-01	2.463989e-02	1.0000000000e+00	0.000000e+00
4	9.9969645328e-01	2.463989e-02	1.0000000000e+00	0.000000e+00
5	1.0000000000e+00	0.000000e+00	1.0000000000e+00	0.000000e+00
6	1.0000000000e+00	0.000000e+00	1.0000000000e+00	0.000000e+00

Table 2.2: *For SL_1 and $\beta = 0.05$, the scalar product and angles (in rad) between $\vec{v}_i$ and $\partial\vec{v}_i/\partial\alpha$ and between $\vec{v}_i$ and $\partial\vec{v}_i/\partial\delta$ for $i = 1, \ldots, 6$.*

also holds for most of the equilibrium points close to SL_1. For this reason, during the design of the control strategy, it will be enough to assume that there is no variation on the eigenvectors when we change the sail orientation, since this simplifies the algorithm. We will see that this assumption does not affect the controllability of the trajectory and that there are other more relevant effects.

Finally, we want to see how the fixed points vary on the $\{p_0; \vec{v}_1, \ldots, \vec{v}_6\}$ reference system. We express the variations $\partial p/\partial\alpha$ and $\partial p/\partial\delta$ in this reference system:

$$\begin{aligned} \partial p/\partial\alpha &= [\ -0.0499250,\ -0.0499250,\ 0.0,\ 0.0801638,\ 0.0,\ 0.0\ ], \\ \partial p/\partial\delta &= [\ 0.0,\ 0.0,\ 0.0,\ 0.0,\ 0.0,\ -0.0369099\ ]. \end{aligned}$$

Hence, variations in α give variations of the fixed points position on the saddle projection close to the $y = x$ line, and on the first centre projection close to the y axis. Variations in δ are only seen at first order on the second centre projections following the y axis. This can be graphically seen in Figure 2.3 where the projections of $\partial p/\partial\alpha$ and $\partial p/\partial\delta$ are plotted.

From these results we see that there are fixed points in both sides of the saddle plane if we change the sail orientation. Furthermore, the unstable directions of these new fixed points can bring the trajectory back to a neighbourhood of p_0 and control the saddle

Eigenvalue Base

$\vec{v}_1$
-4.077796276e-01 + 0.000000000e+00 i
5.800454128e-01 + 0.000000000e+00 i
0.000000000e+00 + 0.000000000e+00 i
-4.055535946e-01 + 0.000000000e+00 i
5.768789961e-01 + 0.000000000e+00 i
0.000000000e+00 + 0.000000000e+00 i

$\vec{v}_2$
4.077796276e-01 + 0.000000000e+00 i
5.800454123e-01 + 0.000000000e+00 i
0.000000000e+00 + 0.000000000e+00 i
-4.055535946e-01 + 0.000000000e+00 i
-5.768789964e-01 + 0.000000000e+00 i
0.000000000e+00 + 0.000000000e+00 i

$\vec{v}_3$
-6.910208352e-01 + 5.458900103e-17 i
6.899013069e-17 - 1.483922517e+00 i
0.000000000e+00 + 0.000000000e+00 i
4.038108119e-17 - 8.685647482e-01 i
1.865186579e+00 + 0.000000000e+00 i
0.000000000e+00 + 0.000000000e+00 i

$\vec{v}_4$
-6.910208352e-01 - 5.458900103e-17 i
6.899013060e-17 + 1.483922511e+00 i
0.000000000e+00 + 0.000000000e+00 i
4.038108119e-17 + 8.685647482e-01 i
1.865186571e+00 + 0.000000000e+00 i
0.000000000e+00 + 0.000000000e+00 i

$\vec{v}_5$
0.000000000e+00 + 0.000000000e+00 i
0.000000000e+00 + 0.000000000e+00 i
0.000000000e+00 - 1.563188613e+00 i
0.000000000e+00 + 0.000000000e+00 i
0.000000000e+00 + 0.000000000e+00 i
1.855682796e+00 + 0.000000000e+00 i

$\vec{v}_6$
0.000000000e+00 + 0.000000000e+00 i
0.000000000e+00 + 0.000000000e+00 i
0.000000000e+00 + 1.563188613e+00 i
0.000000000e+00 + 0.000000000e+00 i
0.000000000e+00 + 0.000000000e+00 i
1.855682796e+00 + 0.000000000e+00 i

Variation of the eigenvalues w.r.t. α, δ

	$\partial\vec{v}_1/\partial\alpha$	$\partial\vec{v}_1/\partial\delta$
c_1	1.000000000e+00 + 0.000000000e+00 i	1.000000000e+00 + 0.000000000e+00 i
c_2	-3.114691120e-02 - 0.000000000e+00 i	-0.000000000e+00 - 0.000000000e+00 i
c_3	-1.338519691e-02 - 8.79999378e-03 i	0.000000000e+00 - 0.000000000e+00 i
c_4	-1.338519691e-02 + 8.79999378e-03 i	-0.000000000e+00 - 0.000000000e+00 i
c_5	0.000000000e+00 + 0.000000000e+00 i	4.834368141e-03 + 5.770445554e-03 i
c_6	0.000000000e+00 + 0.000000000e+00 i	4.834368141e-03 - 5.770445554e-03 i

	$\partial\vec{v}_2/\partial\alpha$	$\partial\vec{v}_2/\partial\delta$
c_1	3.114691120e-02 - 0.000000000e+00 i	-0.000000000e+00 - 0.000000000e+00 i
c_2	1.000000000e+00 + 0.000000000e+00 i	1.000000000e+00 + 0.000000000e+00 i
c_3	-1.338519691e-02 + 8.79999378e-03 i	0.000000000e+00 + 0.000000000e+00 i
c_4	-1.338519691e-02 - 8.79999378e-03 i	-0.000000000e+00 + 0.000000000e+00 i
c_5	0.000000000e+00 + 0.000000000e+00 i	4.834368141e-03 - 5.770445554e-03 i
c_6	0.000000000e+00 + 0.000000000e+00 i	4.834368141e-03 + 5.770445554e-03 i

	$\partial\vec{v}_3/\partial\alpha$	$\partial\vec{v}_3/\partial\delta$
c_1	-1.246793485e-03 - 5.469755459e-02 i	0.000000000e+00 - 0.000000000e+00 i
c_2	-1.246793485e-03 + 5.469755459e-02 i	-0.000000000e+00 - 0.000000000e+00 i
c_3	1.000000000e+00 + 0.000000000e+00 i	1.000000000e+00 + 0.000000000e+00 i
c_4	7.621968644e-19 + 2.464487717e-02 i	-0.000000000e+00 + 0.000000000e+00 i
c_5	-0.000000000e+00 - 0.000000000e+00 i	-2.235393055e-17 - 2.829696728e-01 i
c_6	0.000000000e+00 + 0.000000000e+00 i	-6.385580992e-19 - 8.083257483e-03 i

	$\partial\vec{v}_4/\partial\alpha$	$\partial\vec{v}_4/\partial\delta$
c_1	-1.246793485e-03 + 5.469755459e-02 i	-0.000000000e+00 + 0.000000000e+00 i
c_2	-1.246793485e-03 - 5.469755459e-02 i	0.000000000e+00 + 0.000000000e+00 i
c_3	7.621968644e-19 - 2.464487717e-02 i	0.000000000e+00 + 0.000000000e+00 i
c_4	1.000000000e+00 + 0.000000000e+00 i	1.000000000e+00 + 0.000000000e+00 i
c_5	0.000000000e+00 + 0.000000000e+00 i	-6.385580992e-19 + 8.083257483e-03 i
c_6	0.000000000e+00 + 0.000000000e+00 i	-2.235393055e-17 + 2.829696728e-01 i

	$\partial\vec{v}_5/\partial\alpha$	$\partial\vec{v}_5/\partial\delta$
c_1	0.000000000e+00 + 0.000000000e+00 i	-2.754707078e-02 + 2.307840532e-02 i
c_2	-0.000000000e+00 + 0.000000000e+00 i	-2.754707078e-02 - 2.307840532e-02 i
c_3	0.000000000e+00 + 0.000000000e+00 i	-1.385009079e-17 - 3.115954634e-01 i
c_4	-0.000000000e+00 + 0.000000000e+00 i	3.956390413e-19 - 8.900976335e-03 i
c_5	1.000000000e+00 + 0.000000000e+00 i	1.000000000e+00 + 0.000000000e+00 i
c_6	0.000000000e+00 + 0.000000000e+00 i	0.000000000e+00 + 0.000000000e+00 i

	$\partial\vec{v}_6/\partial\alpha$	$\partial\vec{v}_6/\partial\delta$
c_1	-0.000000000e+00 + 0.000000000e+00 i	-2.754707078e-02 - 2.307840532e-02 i
c_2	0.000000000e+00 + 0.000000000e+00 i	-2.754707078e-02 + 2.307840532e-02 i
c_3	0.000000000e+00 + 0.000000000e+00 i	3.956390413e-19 + 8.900976335e-03 i
c_4	-0.000000000e+00 + 0.000000000e+00 i	-1.385009079e-17 + 3.115954634e-01 i
c_5	0.000000000e+00 + 0.000000000e+00 i	0.000000000e+00 + 0.000000000e+00 i
c_6	1.000000000e+00 + 0.000000000e+00 i	1.000000000e+00 + 0.000000000e+00 i

Table 2.3: *For SL_1 and $\beta = 0.05$, the eigenvectors ($\vec{v}_i$) and their variation w.r.t. α ($\partial\vec{v}_i/\partial\alpha$) and δ ($\partial\vec{v}_i/\partial\delta$) in the eigenvector base ($\sum_i^6 c_i\vec{v}_i$).*

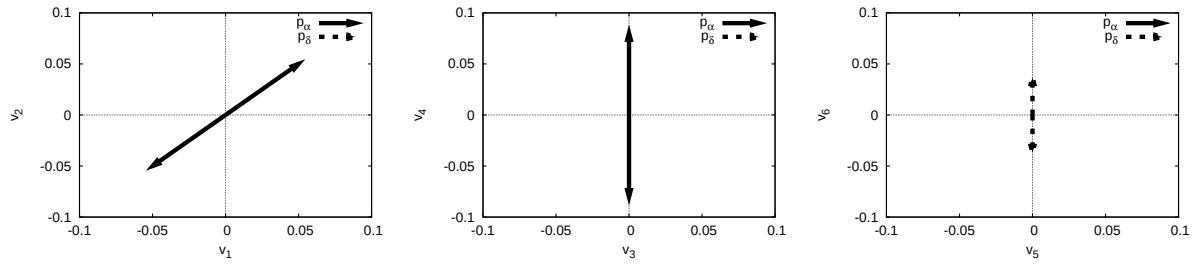

Figure 2.3: *Variation of the linear approximation of the fixed points $\partial p/\partial\alpha$ and $\partial p/\partial\delta$ on the reference system $\{p_0; \vec{v}_1, \ldots, \vec{v}_6\}$. From left to right: saddle projection $\{\vec{v}_1, \vec{v}_2\}$, first centre projection $\{\vec{v}_3, \vec{v}_4\}$ and second centre projection $\{\vec{v}_5, \vec{v}_6\}$.*

instability (see Figure 2.2). For instance, if the variation of the new fixed points on the saddle projection is far from the unstable direction ($\vec{v}_\lambda$) then it will not be possible to find a new fixed point to bring the trajectory back.

2.2 Station Keeping

In this section we give the details on the station keeping algorithm that we have designed. We will describe the effects on the linear dynamics when the sail orientation is changed and how to take advantage of this. At the end we will apply these strategies on the previous example.

2.2.1 Dynamics near an equilibrium point

We describe the trajectory of the probe by its projection on three different planes centred on p_0. The first plane describes the saddle behaviour and the other two describe the central behaviour of the motion. Using the reference system $R = \{\ p_0;\ \vec{v}_1,\ \ldots\ , \vec{v}_6\ \}$, we express the probe's trajectory as $(\ x_1(t), y_1(t), x_2(t), y_2(t), x_3(t), y_3(t)\ )$.

When we are close to the equilibrium point, the sail escapes along the unstable direction. We want to obtain a sail orientation such that the unstable direction of the new fixed point brings the probe back to the proximity of the initial fixed point p_0 (Figure 2.2). Moreover, we want to maintain the centre behaviour bounded. As we know the fixed points live in a 2D surface and we have a 6D phase space, so we have some limitations in the positions of the new fixed point.

To begin, we assume that we are free to choose the fixed points position. First we describe the saddle and centre behaviour of the trajectory when the sail orientation is

changed and where should the new fixed point be placed in order to deal with the instability. Latter on, we will show how to choose an appropriate sail orientation taking into account the limitations on the fixed points position.

Saddle behaviour

Suppose that for $\alpha = \alpha_0$ and $\delta = \delta_0$ the fixed point is at the origin. Hence, the motion on the saddle projection is,

$$\left.\begin{array}{rcl} x_1(t) & = & x_{10}e^{\lambda(t-t_0)} \\ y_1(t) & = & y_{10}e^{-\lambda(t-t_0)} \end{array}\right\}, \tag{2.8}$$

where (x_{10}, y_{10}) is the initial condition.

When the sail orientation is changed, $\alpha = \alpha_0 + \epsilon_\alpha$ and $\delta = \delta_0 + \epsilon_\delta$, the fixed point and the eigenvalues and eigenvectors change slightly. From now on, we consider that the eigenvectors are the same as the ones at the origin. Later on we will see that this approximation is good enough as the variations on the eigenvectors are very small. If (ξ_1, η_1) are the coordinates of the new fixed point on this projection and $\pm\bar{\lambda}$ are the real eigenvalues for (ξ_1, η_1), then the motion of the probe is given by,

$$\left.\begin{array}{rcl} \bar{x}_1(t) & = & \xi_1 + (\bar{x}_{10} - \xi_1)e^{\bar{\lambda}(t-t_0)} \\ \bar{y}_1(t) & = & \eta_1 + (\bar{y}_{10} - \eta_1)e^{-\bar{\lambda}(t-t_0)} \end{array}\right\}, \tag{2.9}$$

where $(\bar{x}_{10}, \bar{y}_{10})$ is the initial condition.

To control the saddle behaviour we define two bounds $B_1 = \{x_1 = \varepsilon_{min}\}$ (the minimal distance to the stable direction) and $B_2 = \{x_1 = \varepsilon_{max}\}$ (the maximal distance to the stable direction), that define the region of movement (between B_1 and B_2), see Figure 2.4. When the trajectory reaches one of these two bounds the sail orientation is changed. We will determine ε_{min} and ε_{max} depending on the mission interest and the phase space properties.

If the sail orientation is fixed to $\alpha = \alpha_0$ and $\delta = \delta_0$ the trajectory is given by equation (2.8) and goes from B_1 to B_2. When the sail orientation is changed to $\alpha = \alpha_1$ and $\delta = \delta_1$ the trajectory is given by equation (2.9). The initial condition of one movement is the end condition of the previous movement. From now on we refer to the points where we change the sail orientation as **change points**.

In order to control the instability the new fixed point (ξ_1, η_1) must be chosen so that $\xi_1 > \varepsilon_{max}$ (see Figure 2.4). As we are supposing that the eigenvectors do not depend on (ξ, η), then the unstable direction of the new fixed point will bring the probe back to B_1.

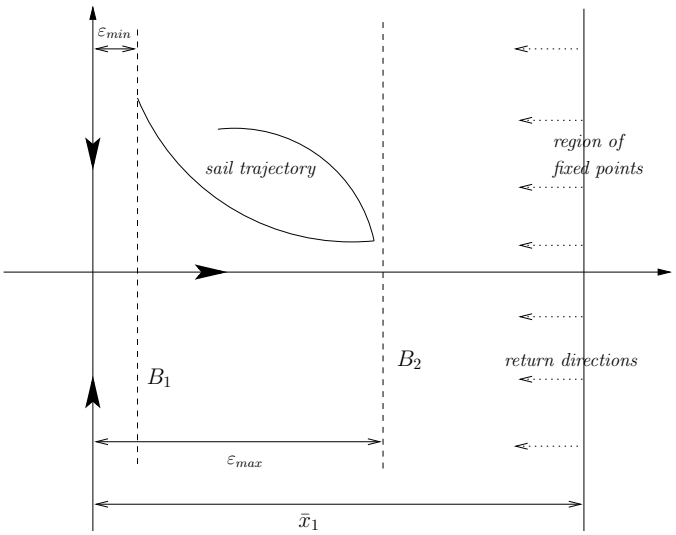

Figure 2.4: *Graphic representation of the relevant parameters to control the saddle projection.*

Notice that we can estimate the time (Δt_i) it takes to go from one bound to the other. From B_1 to B_2, the trajectories follow equation (2.8), with $x_{10} = \varepsilon_{min}$ and $x_1(t_f) = \varepsilon_{max}$. So $\varepsilon_{max} = \varepsilon_{min} e^{\lambda \Delta t_1}$ and we have that,

$$\Delta t_1 = \frac{1}{\lambda} \log \left(\frac{\varepsilon_{max}}{\varepsilon_{min}} \right). \tag{2.10}$$

From B_2 to B_1, the trajectories follow equation (2.9), with $\bar{x}_{10} = \varepsilon_{max}$ and $\bar{x}_1(t_f) = \varepsilon_{min}$. So $\varepsilon_{min} = \xi_1 + (\varepsilon_{max} - \xi_1) e^{\bar{\lambda} \Delta t_2}$ and we have that,

$$\Delta t_2 = \frac{1}{\bar{\lambda}} \log \left(\frac{\xi_1 - \varepsilon_{min}}{\xi_1 - \varepsilon_{max}} \right). \tag{2.11}$$

Notice that Δt_2 varies with the fixed point as it also depends on $\bar{\lambda}$ and ξ_1.

Let t_i for $i \in \mathbb{N}$ be the instant of time when the probe is at one of the bounds $B_{1,2}$. We can assume that $t_0 = 0$ and that the probe is initially placed in B_1. Then,

$$\begin{aligned} t_{2i+1} &= t_{2i} + \Delta t_1, \\ t_{2i+2} &= t_{2i+1} + \Delta t_2, \end{aligned}$$

for $i \in \mathbb{N}$, where t_{2i} is the time when the probe is placed at B_1 and t_{2i+1} when it is placed at B_2.

Let $(\zeta_1^{(i)}, \nu_1^{(i)})$ be the sequence of change points, where for i even the change points are in B_1 ($\zeta_1^{(i)} = \varepsilon_{min}$) and for i odd they are in B_2 ($\zeta_1^{(i)} = \varepsilon_{max}$). The following lemma shows a sequence of new fixed points $(\xi_1^{(i)}, \eta_1^{(i)})$ that control the saddle instability.

Lemma 2.2.1 *Let $(\xi_1^{(i)}, \eta_1^{(i)})$ be the sequence of new fixed points for the control strategy and $(\zeta_1^{(i)}, \nu_1^{(i)})$ the sequence of change points. If we choose $\eta_1^{(i)} = \nu_1^{(2i+1)}$ and $\xi_1^{(i)} = \xi^*$ with $\xi^* > \varepsilon_{max}$, then*

$$\lim_{i\to\infty} \eta_1^{(i)} = 0,$$

so the control strategy new fixed points tend to $(\xi^*, 0)$ and the saddle behaviour is stabilised.

Proof We will see by induction that $\nu_1^{(2n+1)} = \nu_1^{(0)} \left(\frac{\varepsilon_{min}}{\varepsilon_{max}}\right)^n$.

For $n = 1$,

$$\nu_1^{(1)} = y_1(t_0 + \Delta t_1) = \nu_1^{(0)} e^{-\lambda \Delta t_1} = \nu_1^{(0)} \left(\frac{\varepsilon_{min}}{\varepsilon_{max}}\right).$$

We suppose it is true for $n = i$, and we see it holds for $n = i + 1$.

$$\nu_1^{(2i+3)} = y_1(t_{2i+2} + \Delta t_1) = \nu_1^{(2i+2)} e^{-\lambda \Delta t_1} = \nu_1^{(2i+2)} \left(\frac{\varepsilon_{min}}{\varepsilon_{max}}\right), \tag{2.12}$$

where

$$\nu_1^{(2i+2)} = \bar{y}_1(t_{2i+1} + \Delta t_2) = \eta_1^{(i)} + (\nu_1^{(2i+1)} - \eta_1^{(i)}) e^{-\lambda \Delta t_2},$$

as we are considering $\eta_1^{(i)} = \nu_1^{(2i+1)} \Rightarrow \nu_1^{(2i+2)} = \nu_1^{(2i+1)}$. Then by the induction hypothesis equation (2.12) becomes,

$$\nu_1^{(2i+3)} = \nu_1^{(0)} \left(\frac{\varepsilon_{min}}{\varepsilon_{max}}\right)^{i+1}. \tag{2.13}$$

As $\varepsilon_{max} > \varepsilon_{min}$,

$$\lim_{n\to\infty} \eta_1^{(n)} = \lim_{n\to\infty} \nu_1^{(0)} \left(\frac{\varepsilon_{min}}{\varepsilon_{max}}\right)^n = 0.$$

□

In Figure 2.5 we have a graphical representation of the trajectory that the sail would follow if we chose the sequence of new fixed points satisfying the hypothesis on lemma 2.2.1.

Notice that if the sequence of new fixed points are as in lemma 2.2.1 but taking $\eta_1^{(i)}$ close to $\nu^{(2i+1)}$, then the saddle behaviour is also controlled, although the sequence of fixed points may not converge.

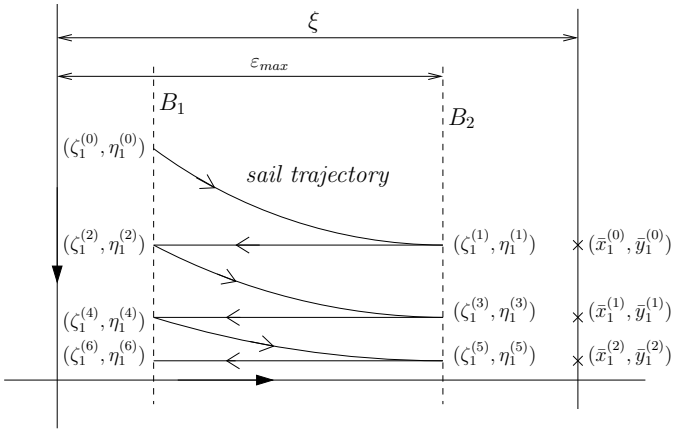

Figure 2.5: *Sequence of ideal fixed points and the projection of the probe's trajectory in the saddle plane.*

Centre behaviour

Suppose that for $\alpha = \alpha_0$, $\delta = \delta_0$ the fixed point is at the origin and let (x_{20}, y_{20}) be the initial condition. Then the motion on one of the centre projection is

$$\left.\begin{aligned} x_2(t) &= r_0 \cos(\omega(t - t_0) + \tau_0) \\ y_2(t) &= r_0 \sin(\omega(t - t_0) + \tau_0) \end{aligned}\right\}, \tag{2.14}$$

where $r_0 = \sqrt{x_{20}^2 + y_{20}^2}$ and $\tau_0 = \arctan\left(\dfrac{y_{20}}{x_{20}}\right)$.

When the sail orientation is changed to $\alpha = \alpha_0 + \epsilon_\alpha$ and $\delta = \delta_0 + \epsilon_\delta$, the fixed point changes as well as the eigenvalues and eigenvectors. As before we consider that the eigenvectors are the same as the ones at the origin. If (ξ_2, η_2) is the new fixed point and $\pm i\bar{\omega}$ are the pair of complex eigenvalues for (ξ_2, η_2), then the motion of the probe is given by

$$\left.\begin{aligned} \bar{x}_2(t) &= \xi_2 + \bar{r}_0 \cos(\bar{\omega}(t - t_0) + \bar{\tau}_0) \\ \bar{y}_2(t) &= \eta_2 + \bar{r}_0 \sin(\bar{\omega}(t - t_0) + \bar{\tau}_0) \end{aligned}\right\}, \tag{2.15}$$

where $\bar{r}_0 = \sqrt{(\xi_2 - \bar{x}_{20})^2 + (\eta_2 - \bar{y}_{20})^2}$, $\bar{\tau}_0 = \arctan\left(\dfrac{\eta_2 - \bar{y}_{20}}{\xi_2 - \bar{x}_{20}}\right)$ and $(\bar{x}_{20}, \bar{y}_{20})$ is the initial condition.

The control on the saddle part fixes the time between manoeuvres, previously we have seen how to estimate Δt_1 and Δt_2 (remember Δt_2 varies with the fixed point). So the movement in the centre part are a sequence of rotations around each of the fixed points.

The rotations around the origin are of angle $\theta_1 = \omega_1 \Delta t_1$ and the rotations around the different fixed points are of angle $\theta_2 = \bar{\omega} \Delta t_2$, where θ_2 varies with the fixed point.

The composition of rotations around different fixed points does not need to be bounded. We would like to place the fixed points so that this movement does not grow. In fact we will show a sequence of fixed points where the trajectory tends to the equilibrium point.

Let us assume that, for $\alpha = \alpha_0$, $\delta = \delta_0$ the fixed point is at the origin and the trajectory is an arc starting at the initial condition (x_{20}, y_{20}) and radius $r_0 = \sqrt{x_{20}^2 + y_{20}^2}$. Let (ζ_2, ν_2) be the change point, we want to find a fixed point (ξ_2, η_2) so that the arc described around this new fixed point ends closer to the origin than (x_{20}, y_{20}).

Depending on the position of (ξ_2, η_2) with respect to the (ζ_2, ν_2) the arc may or may not be totally included in the disk, D_0, centred at the origin and radius r_0. We are interested in choosing a fixed point so that the arc described by the probe is completely included in D_0 (see Figure 2.6).

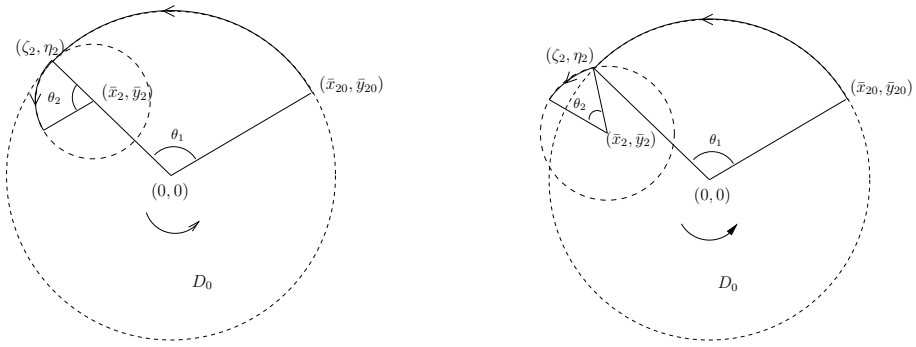

Figure 2.6: *Relative position of a fixed point where the arc described by the probe is not included in D_0 (right) and where it is included in D_0 (left).*

It is true that knowing the arc of rotation θ_2 there are lots of fixed points that can describe an arc completely included in D_0, however, we do not know θ_2 in advance, as it depends on the fixed point. Although we can have it bounded. Therefore, we need to find fixed points so that $\forall\ \theta_2 \in [0, 2\pi]$ the arc described is included in D_0.

Lemma 2.2.2 *Let D_0 be the disk centred at the origin and of radius $r_0 = \sqrt{x_{20}^2 + y_{20}^2}$ and (ζ_2, ν_2) the change point on ∂D_0. Then all the fixed points (ξ_2, η_2) such that $\xi_2 = s \cdot \zeta_2$, $\eta_2 = s \cdot \nu_2$ and $s \in [0, 1)$ describe an arc included in D_0 $\forall\ \theta_2 \in [0, 2\pi)$. If $s = 1/2$ the distance to the origin of the end point of the arc is minimal.*

Proof If two disks coincide in one point, one is included in the other if and only if these two disks are tangential and the centres are included in the biggest disk. So we are looking for arcs tangent to D_0 and with the centre included in D_0.

If (ζ_2, ν_2) is the change point and (ξ_2, η_2) is the fixed point, the arc will be tangential if only if $(\xi_2, \eta_2) = (s \cdot \zeta_2, s \cdot \nu_2)$. If the centre has to be included in D_0 then $s \in (-1, 1)$.

Then the arc described by the probe is given by,

$$\xi_2(T) = sr_0 \cos(\theta_1 + \tau) + (s-1)r_0 \cos(T + \bar{\tau}), \tag{2.16}$$

$$\eta_2(T) = sr_0 \sin(\theta_1 + \tau) + (s-1)r_0 \sin(T + \bar{\tau}), \tag{2.17}$$

which depends on the time $T \in [0, \theta_2]$.

We want,

$$\xi_2(\theta_2)^2 + \eta_2(\theta_2)^2 = r_0^2(2s^2 + 2s - 1 + 2s(s-1)\cos(\theta_1 - \theta_2 + \tau - \bar{\tau})) < r_0^2 \tag{2.18}$$

Let us consider $f(s) = 2s(s-1)(1 + \cos(\theta_1 - \theta_2 + \tau - \bar{\tau}))$. Solving equation (2.18) is equivalent to finding s such that $f(s) < 0$. It is easy to see that $f(s) < 0$ for $s \in (0, 1)$ independent to the value of θ_2.

Notice that if $f(s)$ is minimal the distance to the origin is also minimal. It is easy to see that this is achieved when $s = 1/2$.

□

As before, let us define $(\zeta_2^{(i)}, \nu_2^{(i)})$ as the change points, having for i odd change points from equation (2.14) to equation (2.15) and for i even change points from equation (2.15) to equation (2.14). As we have already said we want to find a sequence of fixed points $(\xi_2^{(i)}, \eta_2^{(i)})$ that makes the trajectory tend to the origin.

Lemma 2.2.3 *Let $(\xi_2^{(i)}, \eta_2^{(i)})$ be the sequence of new fixed points for the control strategy and $(\zeta_2^{(i)}, \nu_2^{(i)})$ the sequence of fixed points. If we choose $\xi_2^{(i)} = \zeta_2^{(2i+1)}/2$ and $\eta_2^{(i)} = \nu_2^{(2i+1)}/2$ then the sequence of change points $(\zeta_2^{(i)}, \nu_2^{(i)})$ tend to the origin and so does the trajectory.*

Proof Let us consider $r^{(i)} = \sqrt{(\zeta^{(i)})^2 + (\nu^{(i)})^2}$. It is easy to see that $r^{2i} = r^{(2i+1)}$ as the change points (ζ^{2i}, ν^{2i}) and $(\zeta^{2i+1}, \nu^{2i+1})$ belong to the same arc centred on the origin.

Using Lemma 2.2.2 we can see that taking $(\xi_2^{(i)}, \eta_2^{(i)}) = (\zeta^{(2i+1)}/2, \nu^{(2i+1)}/2)$ we get, $r^{2i+1} > r^{2i+2}$. Then $r^{2i} > r^{2i+2}$ and the sequence for change points tend to the origin and so does the projection of the trajectory.

□

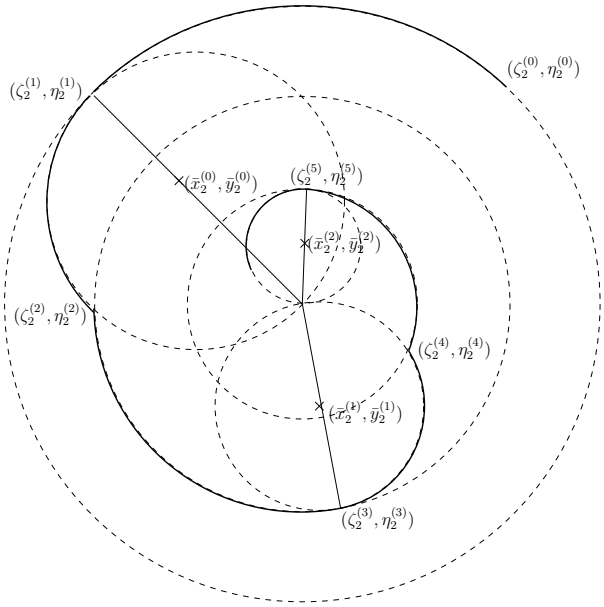

Figure 2.7: *Sequence of ideal fixed points to minimise the centre projection and the projection of the probe's trajectory in the centre plane.*

In Figure 2.7 we have a graphical representation of the trajectory that the sail would follow if we take the sequence of new fixed points $(\xi_2^{(i)}, \eta_2^{(i)}) = (\zeta_2^{(2i+1)}/2, \nu_2^{(2i+1)}/2)$. As we see, the trajectory tends to the origin.

Notice that if $(\xi_2^{(i)}, \eta_2^{(i)}) = (s \cdot \zeta_2^{(2i+1)}, s \cdot \nu_2^{(2i+1)})$ with $s \in [0, 1)$ the trajectory also decreases. There are also other choices, close to these ones, that make the centre behaviour decrease or at least keep it bounded.

2.2.2 Choosing the new sail orientation (α, δ)

We have just seen an ideal sequence of fixed points to control the instability of p_0. As we have already said the fixed points live on a 2D surface parametrised by α and δ in a 6D phase space. So we might not be able to find a sail orientation α_1 and δ_1 where the fixed point is one of the ideal positions described before. Nevertheless, we have also seen that if the new fixed point is close enough to this ideal new equilibria, we are also able to maintain the trajectory close to the desired fixed point.

We use the linear approximation of the 2D surface of fixed points, $p(\alpha, \delta)$, seen in Section 2.1.1. We want to find $h = (\alpha - \alpha_0, \delta - \delta_0)^T$ such that,

$$\bar{p} - p_0 = Dp \cdot h, \tag{2.19}$$

where $\bar{p}$ is the desired new fixed point, described above. Note that although equation (2.19) has 6 equations and 2 unknowns, under general conditions we can still find α_1, δ_1 such that $\|\bar{p} - p(\alpha_1, \delta_1)\|$ is small enough.

Notice that although $\|\bar{p} - p(\alpha_1, \delta_1)\|$ is small, $p(\alpha_1, \delta_1)$ may not be able to control the instability due to the saddle part. If the projection of $p(\alpha_1, \delta_1)$ on the saddle plane is on the left hand side of B_2 then the unstable direction of $p(\alpha_1, \delta_1)$ will not bring the probe back (see Figure 2.8). To avoid this we fix one of the components of the fixed point $\bar{p}$ on the saddle projection. Now we have to find the fixed points in a 1D surface.

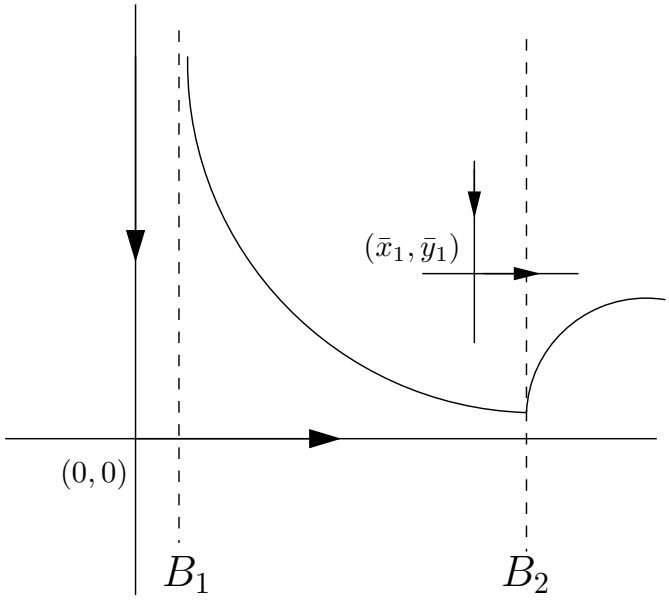

Figure 2.8: *Position of the new fixed point $p(\alpha_1, \delta_1)$ in the saddle projection that will not control the unstable behaviour.*

We now give more details of the process described above. Let $\bar{p}$ be the the ideal position for the new fixed point. The coordinates of $\bar{p}$ are given in a certain reference system $\{p_0; \vec{v}_1, \ldots, \vec{v}_6\}$ (Section 2.2.1) and equation (2.19) is in synodical coordinates. So we first have to change coordinates. Let M_v be the matrix that has $\vec{v}_i$ for $i = 1, \ldots, 6$ as columns and $s = (s_1, \ldots, s_6)$ are the coordinates of the desired new fixed point ($\bar{p}$) in this coordinate system. Then if $A = M_v^{-1} Dp$ equation (2.19) becomes,

$$s^T = A \cdot h. \tag{2.20}$$

To assure the controllability of the saddle behaviour we fix s_1:

1. If $a_{11} = a_{12} = 0$ (i.e. $\dfrac{\partial p}{\partial \alpha}, \dfrac{\partial p}{\partial \delta} \perp \vec{v}_1$):

In this case there are no fixed points using the linear approximation for which its saddle behaviour brings the sail back.

2. If $a_{11} = \max(|a_{11}|, |a_{12}|)$:

$$s_1 = a_{11}h_1 + a_{12}h_2 \Rightarrow h_1 = \frac{s_1 - a_{12}h_2}{a_{11}}, \tag{2.21}$$

3. If $a_{12} = \max(|a_{11}|, |a_{12}|)$:

$$s_1 = a_{11}h_1 + a_{12}h_2 \Rightarrow h_2 = \frac{s_1 - a_{11}h_1}{a_{12}}, \tag{2.22}$$

This reduces equation (2.20) into $\hat{s} = \hat{A} \cdot \hat{h}$ (5 equations and 1 unknown). Then the $\hat{h}$ so that $\|\hat{s} - \hat{A} \cdot \hat{h}\|$ is minimal is,

$$\hat{h} = (\hat{A}^T \hat{A})^{-1} \hat{A}^T s. \tag{2.23}$$

Hence, we have the variation that must be done to the sail orientation.

2.2.3 Summary of the station keeping algorithm

Let p_0 be a fixed point for $\alpha = \alpha_0, \delta = \delta_0$, that is linearly unstable. We assume that the eigenvalues are $\pm\lambda, \pm\mathrm{i}\,\omega_1, \pm\mathrm{i}\,\omega_2$, and take the reference system, $R = \{p_0; \vec{v}_1, \ldots, \vec{v}_6\}$ where,

- p_0 is the fixed point.
- $\vec{v}_1, \vec{v}_2$ are the unstable and stable eigenvector respectively ($\pm\lambda$).
- $\vec{v}_3, \vec{v}_4$ is a couple of real vectors that define the first central motion ($\pm i\omega_1$).
- $\vec{v}_5, \vec{v}_6$ is a couple of real vectors that define the second central motion ($\pm i\omega_2$).

During the station keeping algorithm the trajectories in this reference system is $\Phi(t) = \sum s_i(t)\ \vec{v}_i$, where $(s_1(t), \ldots, s_6(t))$ are the coordinates of the trajectory.

We start with the probe close to the fixed point p_0 with $\alpha = \alpha_0$, $\delta = \delta_0$. Due to the unstable character of the equilibrium point the trajectory escapes from its vicinity. When $|s_1(t^*)| > \varepsilon_{max}$ the probe is considered to be far from p_0 and we choose the appropriate α_1, δ_1 that brings the probe back to a neighbourhood of p_0 and change the sail orientation

($\alpha = \alpha_1$, $\delta = \delta_1$). When $|s_1(t^*)| < \varepsilon_{min}$, the sail is close to p_0 and we change the sail orientation back to $\alpha = \alpha_0$, $\delta = \delta_0$. This process is then restarted.

Notice that we have to fix ε_{max} and ε_{min}, the maximal and minimal distance to the fixed point respectively. These constants depend on the mission objectives and the dynamical properties around the equilibrium point.

On the one hand, ε_{max} is the maximum distance to the fixed point allowed and should be chosen within a range where the linear approximation of the flow gives is accurate description of the motion. And ε_{min} is the minimal distance used to determine when the probe is close enough to the stable direction of the target fixed point. On the other hand, these two quantities determine the time between manoeuvres, and as a consequence determine the angles of rotation on the centre projections. We can play with these two constants and find ranges where we are able to control the trajectory of the sail. Although in some case the time between manoeuvres might not be feasible. We always need to taking into account the nature of the fixed point: instability rate, frequency of the rotations, position of the new fixed points, etc.

We remark that we only use the linear approximation of the set of equations to find the appropriate change on the sail's orientation. During the simulations, we use the whole set of equations. In Section 2.3 we show how this algorithm works for two particular missions, but let us first illustrate how it works with an example.

2.2.4 An example

We take the same equilibrium point as the example in Section 2.1.2. Hence, $\beta = 0.05$ and SL_1 is the fixed point for $\alpha = \delta = 0$. We will take an arbitrary initial condition and apply the station keeping strategy described in the previous sections for at least 15 years. As we know to start the algorithm we need to fix the parameters ϵ_{max} (the maximum distance to the fixed point allowed), ϵ_{min} (the distance to return) and $\bar{x}_1$ (the distance on the saddle plane where we want to fix the new sail orientation), see Figure 2.4 for a graphical representation of these parameters. In our programs we define $\bar{x}_1 = d \cdot \epsilon_{max}$ and ask the user to enter the parameters ϵ_{max}, ϵ_{min} and d.

For a first simulation we take $\epsilon_{max} = 10^{-4}$, $\epsilon_{min} = 5 \times 10^{-6}$ and $d = 1.5$. In Figure 2.9 we have the projection on the trajectory on the XY, XZ planes and its XYZ projection. We can see how the trajectory remains close to the desired equilibria. Moreover, we can see that the station keeping strategy decrease the Z oscillation.

In Figure 2.10 we have the projection of the trajectory on the planes defining the saddle and the two centre directions. Notice that the behaviour on the saddle projection

is a sequence of arcs between two saddles. The first centre plane corresponds to the planar oscillation and the second centre is related to the vertical oscillation. In both centres the projection of the trajectory remains bounded. Moreover, the vertical oscillation decreases quickly. Finally, in Figure 2.11 we can see the variation on the sail orientation along time.

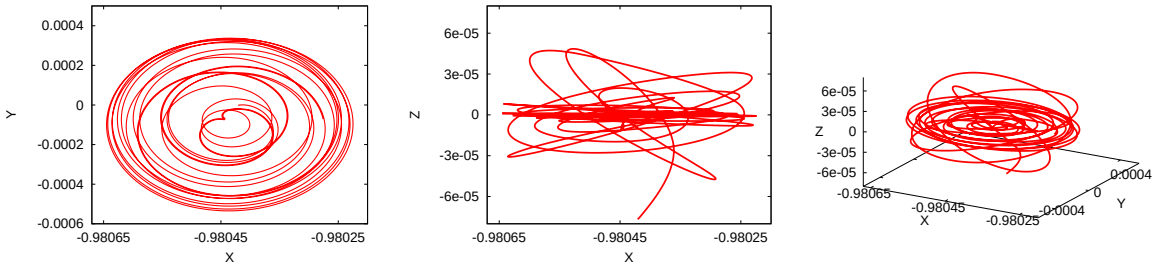

Figure 2.9: *For simulation 1: projections of the trajectory on the position space. From left to right: XY projection, XZ projection and XYZ projection.*

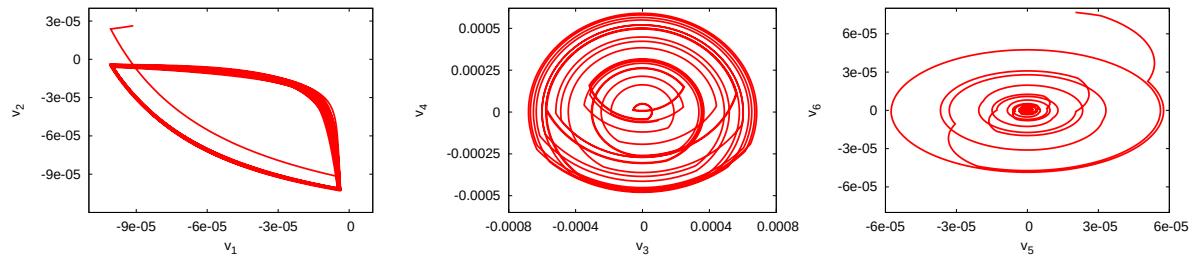

Figure 2.10: *For simulation 1: projections of the trajectory on the three reference planes used on the station keeping strategy. From left to right: saddle projection and the two centre projections.*

For a second simulation we take $\epsilon_{max} = 5 \times 10^{-4}$, $\epsilon_{min} = 5 \times 10^{-6}$ and $d = 1.5$. As before, in Figure 2.12 we have the projection on the trajectory on the XY and XZ planes and its XYZ projection. In Figure 2.13 we find the projection of the trajectory on the saddle plane and the two centre directions, and Figure 2.14 shows the variation on the sail orientation along time.

Now the trajectory escapes after 4360.93 days, the station keeping algorithm has failed. Notice that before the escape time the trajectory on the saddle projection has a fuzzy aspect. If we look at the projection of the trajectory on the first centre direction, we see the rotations have a high amplitude. Hence, the linear approximation in not good enough, what brings the algorithm to fail.

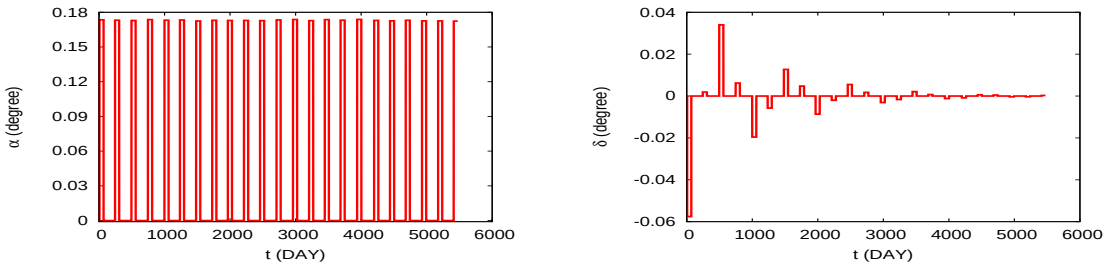

Figure 2.11: *For simulation 1: variation on the sail orientation along time. From left to right variation of α and δ.*

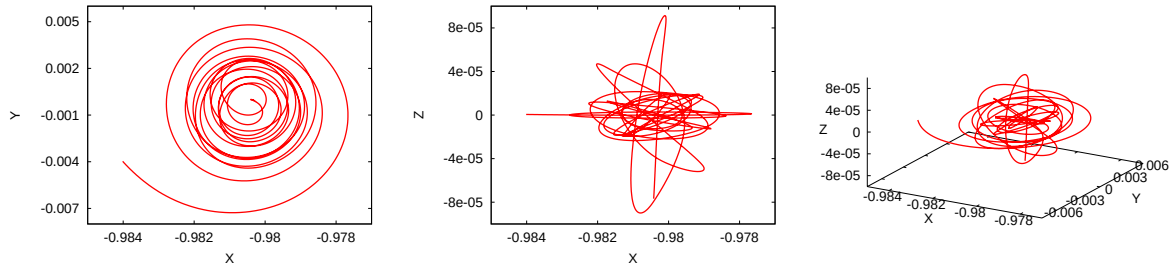

Figure 2.12: *For simulation 2: projections of the trajectory on the position space. From left to right: XY projection, XZ projection and XYZ projection.*

The only difference between the first simulation and the second one is ϵ_{max}, which is larger in the second simulation. Apart from letting the trajectory get further away from the fixed point p_0, taking a larger ϵ_{max} increases the time between manoeuvres and also the angles of rotation on the centre behaviour. Having large rotation angles makes it harder for the algorithm to control the centre projection. In the second simulation, if we increased ϵ_{min}, we would decrease the time between manoeuvres and the rotation angle, managing to control the probe's trajectory.

We want to make clear that as long as variation of the fixed points on the saddle projection allow us to find new fixed points whose unstable manifold bring the probe close to the target fixed point, we can find ranges of values for ϵ_{max} and ϵ_{min} where the rotations on the keep the centre projection bounded. Nevertheless, the time between manoeuvres might not be feasible for a real mission.

On the other hand, notice that in order to control the saddle projection we have two parameters to play with, ϵ_{max} and $\bar{x}_1$ (the x coordinate of the fixed point on the saddle direction). In our strategies this ones have to be chosen in advance and remains fixed during all the simulation. Hence, the place where the manoeuvre takes place is fixed. We could consider these variables within a certain range and choose at each step the best place

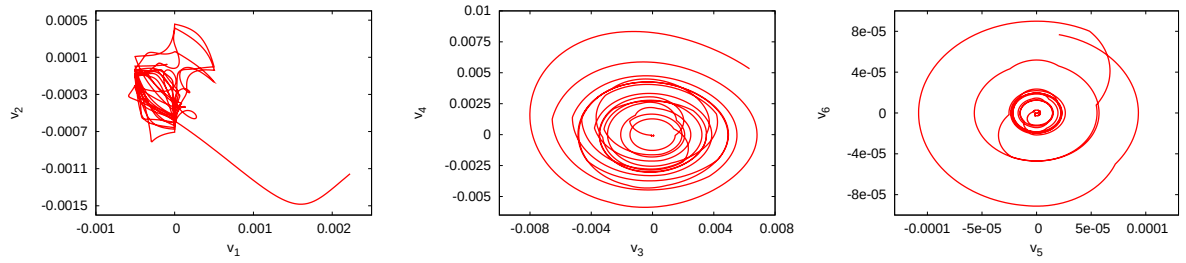

Figure 2.13: *For simulation 2: projections of the trajectory on the three reference planes used on the station keeping strategy. From left to right: saddle projection and the two centre projections.*

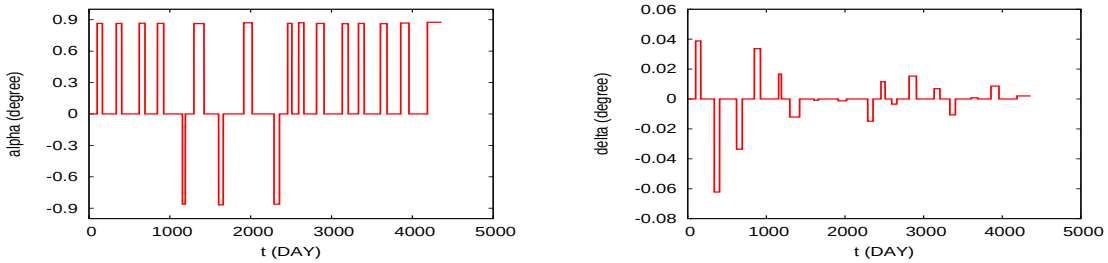

Figure 2.14: *For simulation 2: variation on the sail orientation along time. From left to right variation of α and δ.*

to change, in order to maintain the central projection small. This makes the algorithm a little more complex and we have not considered it as an option for the moment, but it could be a possibility if we had problems maintaining the centre projection bounded.

Now we want to test our station keeping strategies in regions of equilibria that have been considered for possible mission applications. If the natural behaviour around these equilibrium points is similar to the behaviour around SL_1 we will not have problems controlling the trajectory.

2.3 Mission Application

Now we would like to see how the station keeping technique described in the previous section behaves with two proposed missions the Geostorm Warning and the Polar Observer Missions. For each mission we start giving a brief introduction on the mission scenario and its main goal. Then we give some details on the variation of the phase space properties of the region where the mission is applied. Finally, several simulations have been done and the results are discussed.

2.3.1 Geostorm Mission

Its primary goal is to provide enhanced warning of geomagnetic storms to allow operation teams to take preventive actions to protect vulnerable systems. Geomagnetic storms are principally the result of Coronal Mass Ejections (CME), the violent release of large volumes of plasma from the solar corona. The impact of CME on the Earth's magnetosphere can change its magnetic field and produce electromagnetic storms.

Currently predictions of future activity are made by the National Oceanic Atmospheric Administration (NOAA) Space Environment Centre in Colorado using terrestrial data and real-time solar wind data obtained from the Advanced Compositions Explorer (ACE) spacecraft. The ACE spacecraft is stationed on a halo orbit near L_1, at about 0.01 AU from the Earth. From this position the spacecraft has continuous view of the Sun and communication with the Earth. Since the spacecraft is located towards the Sun, the solar wind disturbances sensed by the instruments on board the ACE spacecraft are used to provide early warning of the impinging geomagnetic storms. Typically predictions of order 1 hour can be made from the L_1 Lagrange point.

The enhanced storm warning provided by ACE is limited by the need to orbit the L_1 point. However, since solar sails add an extra force to the dynamics of the orbit, the location of L_1 can be artificially displaced, as it has been shown. The goal of Geostorm is to station a solar sail twice as far from the Earth than L_1 while remaining close to the Earth-Sun line as can be seen in Figure 2.15. Since the CME will be detected earlier than by ACE the warning times and alerts will be at least doubled.

For this mission the solar sail is firstly transfered to a conventional halo orbit at L_1. There the sail would be deployed and transfered to its location at 0.98 AU from the Sun. Once we arrive near close to SL_1 a control strategy must be applied to deal with the instability of the region.

Several studies on this mission have been made [McI99, MM04, Yen04, Lis05, Wes04] Where we can see that a characteristic acceleration of at least $a_0 = 0.3\text{mm/s}^2$ is required so that the spacecraft is placed at a double distance from the Earth-Sun L_1 point. A a total solar sail loading of order 29.6 g/m^2 is considered. To achieve this a $67m \times 67m$ square solar sail is required for a total spacecraft mass of order $130kg$.

Mission orbit

We want to displace the spacecraft at a double distance from the Earth-Sun L_1 point. To avoid interferences with the solar disc, the solar sail will be displaced away from the Sun -

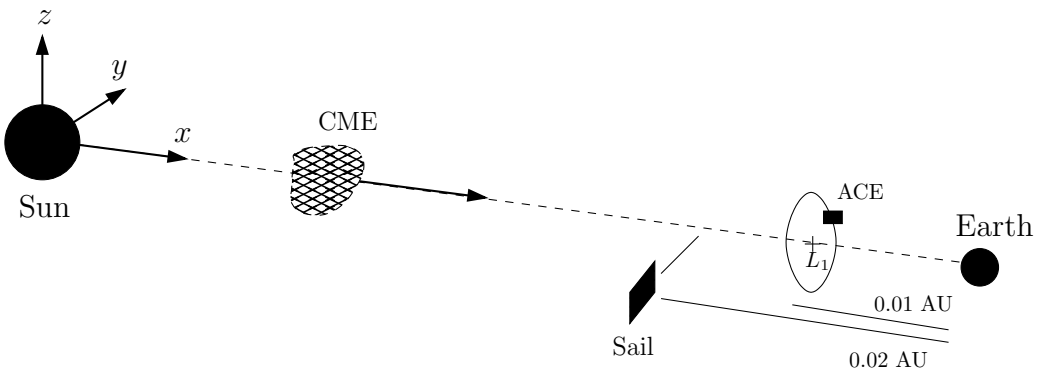

Figure 2.15: *Schematic representation of the position of the Geostorm Mission (not to scale).*

Earth line. A variation of 5° from this line is considered to be enough [McI99, MM04]. Taking into account that we want to be at a distance of $0.02AU$ from the Earth and displaced about 5° from the Sun - Earth line, we required $\beta = 0.051689$, see [McI99, Yen04, MM04]. In Figure 2.16 we have plotted the position of the equilibrium points for different sail orientations and sail lightness numbers close to the Sun - Earth line.

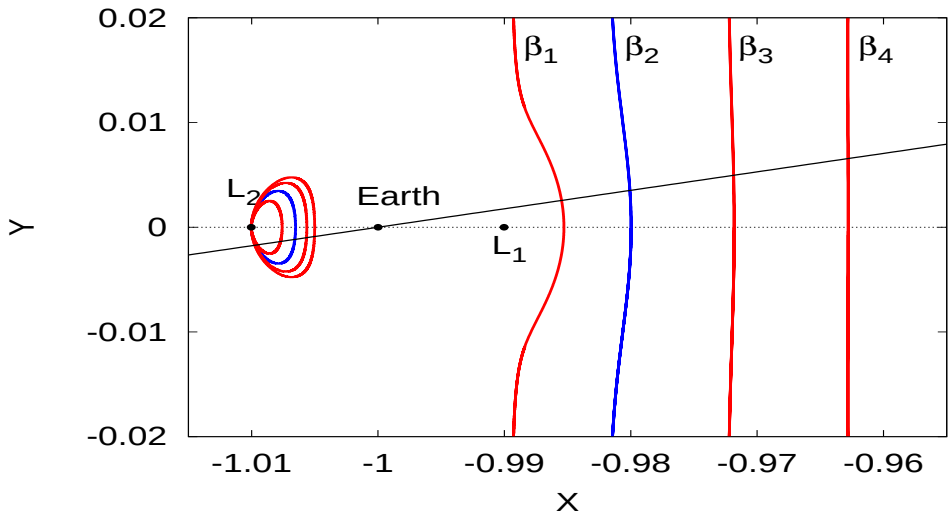

Figure 2.16: *Relation of the fixed point for different sail lightness numbers:* $\beta_1 = 0.03$, $\beta_2 = 0.051689$, $\beta_3 = 0.0786$ *and* $\beta_4 = 0.1055$

We have considered $p_0 = (-0.9800028, 0, 0, 0, 0, 0)$ with an initial sail orientation of $\alpha = 0.0137829$ rad and $\delta = 0$ rad. In Table 2.4 we have the linear variation of the fixed point with respect to α and δ in the synodical reference system and in the eigenvector reference system.

$p_\alpha^\star$	-4.610276e-03	-1.450990e-01	0.000000e+00	0.000000e+00	0.000000e+00	0.000000e+00
$p_\alpha^\dagger$	-5.480083e-02	-6.003004e-02	-2.026453e-03	8.797829e-02	0.000000e+00	0.000000e+00
$p_\delta^\star$	0.000000e+00	0.000000e+00	3.905014e-02	0.00000e+00	0.000000e+00	0.000000e+00
$p_\delta^\dagger$	0.000000e+00	0.000000e+00	0.000000e+00	0.000000e+00	0.000000e+00	-3.905014e-02

Table 2.4: *For the Geostorm mission: linear variation of the position of the fixed point p_0 w.r.t. α and δ, in the synodical reference system (*) and in the eigenvector reference system (†). Where p_α stands for $\partial p/\partial\alpha$ and p_δ stands for $\partial p/\partial\delta$.*

Notice that, at first order, variations on α imply variations on the XY plane, and variations on δ imply variations on the Z direction. In both cases, these variations are small. Regarding the saddle projection we can see that by varying α we have fixed points at both sides of the saddle projection. Hence, there will be no problem in finding appropriate equilibrium point.

We have also computed the linear variation of the eigenvalues and eigenvectors around p_0. In Table 2.5 we have the variation of the eigenvalues. We can see that although one of the complex eigenvalues has a positive real part, the main instability is given by the positive real eigenvalue. Notice that at first order the eigenvalues do not vary with δ and the variations with respect to α are small enough not to vary the nature of the fixed points. In Table 2.6 we have the angles between the eigenvectors and their linear variation with respect to α and δ ($\partial\vec{v}_i/\partial\alpha$, $\partial\vec{v}_i/\partial\delta$). We can see that the maximum is around 0.00344 radians, almost negligible for small variations on the sail orientation.

i	λ_i	$\partial\lambda_i/\partial\alpha$	$\partial\lambda_i/\partial\delta$
0	9.519682e-01 + 0.000000e+00 i	-5.780020e-05 - 0.000000e+00 i	0.000000e+00
1	-9.525896e-01 + 0.000000e+00 i	-1.054805e-04 + 0.000000e+00 i	0.000000e+00
2	3.106890e-04 + 1.236480e+00 i	8.164037e-05 + 1.507482e-05 i	0.000000e+00
3	3.106890e-04 - 1.236480e+00 i	8.164037e-05 - 1.507482e-05 i	0.000000e+00
4	0.000000e+00 + 1.173860e+00 i	-0.000000e+00 + 2.336396e-06 i	0.000000e+00
5	0.000000e+00 - 1.173860e+00 i	0.000000e+00 - 2.336396e-06 i	0.000000e+00

Table 2.5: *For the Geostorm mission, the eigenvalues (λ_i) and their variation w.r.t. α ($\partial\lambda_i/\partial\alpha$) and δ ($\partial\lambda_i/\partial\delta$).*

Results

We have done a Monte Carlo simulation, using 1000 initial conditions chosen in a random way. The control strategy has been applied up to 30 years and we have measured for each simulation the time between manoeuvres, the variation of the sail orientation (α, δ) and the variation of the trajectory with respect to p_0.

i	$\langle \vec{v}_i, \partial\vec{v}_i/\partial\alpha \rangle$	angle	$\langle \vec{v}_i, \partial\vec{v}_i/\partial\delta \rangle$	angle
1	9.9940579569e-01	3.447501e-02	1.0000000000e+00	0.000000e+00
2	9.9934429451e-01	3.621539e-02	1.0000000000e+00	0.000000e+00
3	9.9962467659e-01	2.739879e-02	1.0000000000e+00	0.000000e+00
4	9.9962467659e-01	2.739879e-02	1.0000000000e+00	0.000000e+00
5	9.9999996229e-01	2.746195e-04	1.0000000000e+00	0.000000e+00
6	9.9999996229e-01	2.746195e-04	1.0000000000e+00	0.000000e+00

Table 2.6: *For the Geostorm mission: the scalar product and the angle (in rad) between* $\vec{v}_i$ *and* $\partial\vec{v}_i/\partial\alpha$ *and between* $\vec{v}_i$ *and* $\partial\vec{v}_i/\partial\delta$ *for* $i = 1, \ldots, 6$.

In Figure 2.17 (left) we can see for each simulation the maximum and minimum time between manoeuvres. As we can see the mean value of the minimum time between manoeuvres is around 24 days and the maximum time between manoeuvres is around 45 days. In Figure 2.17 (right) we have the maximum angular variation between the fixed point (p_0) and the probe's trajectory seen from the Earth for each simulation. The mean value of the angular variation of the probe is $\approx 1.43°$, this corresponds to a variation in position of $75399.97km$. The mean valued for the maximum variation in the sail orientation is around $0.27°$ for α and $0.03°$ for δ.

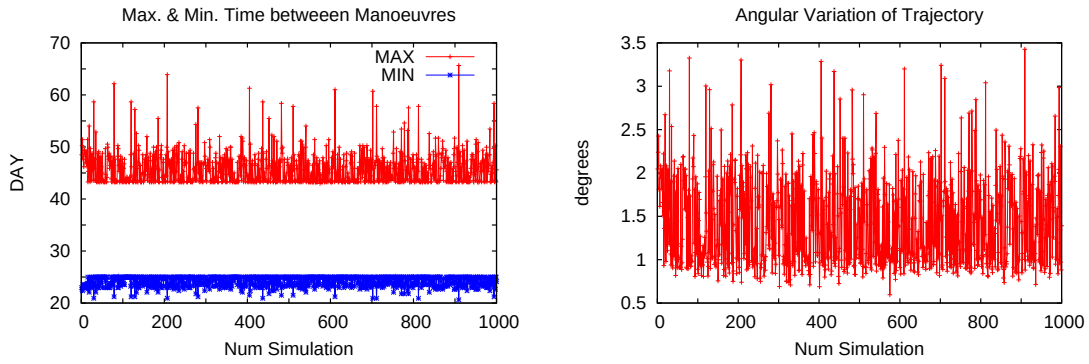

Figure 2.17: *For the Geostorm mission: maximum and minimum time between manoeuvres* vs *number of simulation (left). Maximum angular variation between* p_0 *and the probe's trajectory* vs *number of simulation (right).*

In Figure 2.18 we have different projections of the trajectory given by an arbitrary initial condition after applying the control strategy scheme. Figure 2.19 shows the projection of the orbit on the saddle plane and the two central planes. Finally in Figure 2.20 we see the variation of the sail orientation along time.

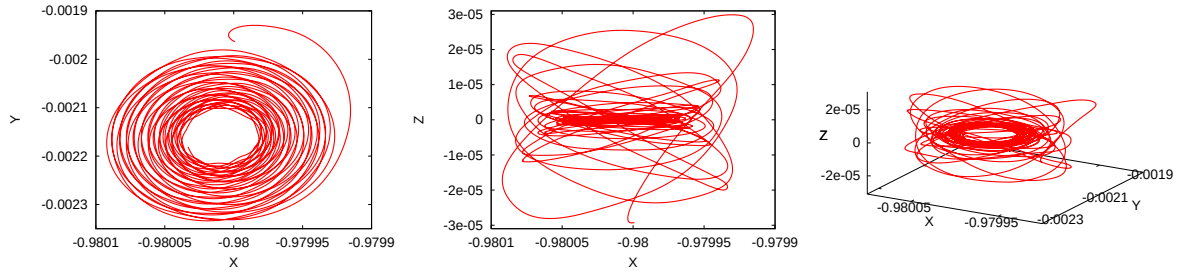

Figure 2.18: *For the Geostorm mission: projections of the probe's trajectory for 30 years on the position space. From left to right: XY projection, XZ projection and XYZ projection.*

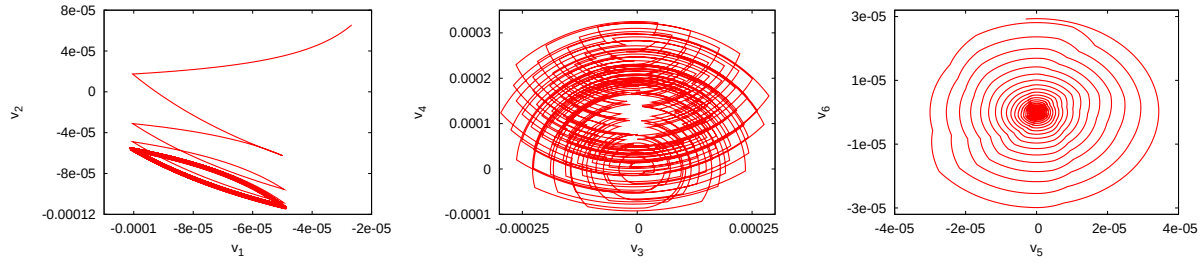

Figure 2.19: *For the Geostorm mission: projections of the probe's trajectory for 30 years on the three reference planes. From left to right: saddle projection, projection on the centre plane generated by $(\vec{v}_3, \vec{v}_4)$ and projection on the centre plane generated by $(\vec{v}_5, \vec{v}_6)$.*

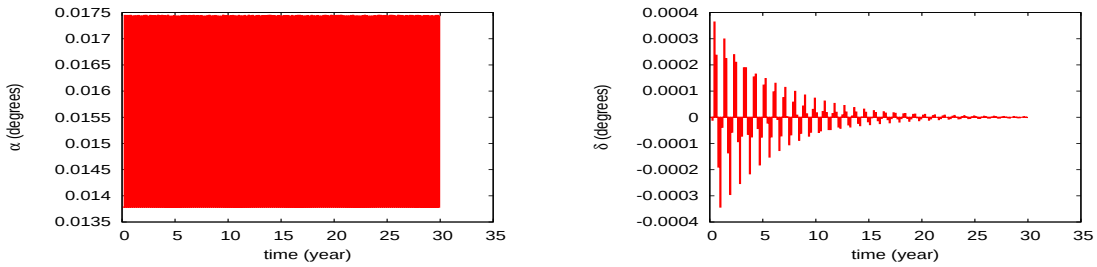

Figure 2.20: *For the Geostorm mission: variation of the sail orientation along time. From left to right variation of α and δ.*

2.3.2 Polar Observer

High latitude regions are of importance for a number of commercial and environmental interests. During the cold war the Arctic was a strategically important region, also the growing interest for the oil and mineral extraction of these regions may lead to a growing demand for communication services. The Arctic and Antarctic are also of great environmental importance and there is a requirement for relaying data from remote weather

stations and automated monitoring platforms. Additional environmental requirements for polar services include continuous imaging of polar weather systems and monitoring of polar ice coverage for climate studies between others.

The limitation of geostationary orbits for such applications may overcome to some extent using satellites in polar orbits. These orbits require the use of various satellites for a complete mapping or having to wait between imaging. Similarly communications services can be provided using high inclination Molniya orbits or through constellation satellites in low Earth orbits. While such systems are well suited for infrequent communications, they are too expensive for real-time relaying data.

In Chapter 1, we have seen that when the effect of the solar radiation pressure is include, there are families of equilibrium points above the ecliptic plane. Placing a solar sail close to one of this points would enable to have constant viewing of the Polar regions of the Earth. As the Earth's inclination is of about 23.4^o we must place the solar sail at 66.6^o from the ecliptic plane. Notice that as the Earth orbits around the Sun, the sail will maintain its fixed position with respect to the Earth but it will not always have the same view at the pole due to the Earth's inclination, see Figure 2.21. Having the sail perfectly situated on the north pole during the summer solstice, and during the winter solstice the sail will appear displaced over the horizon, having still some imaging of the north pole.

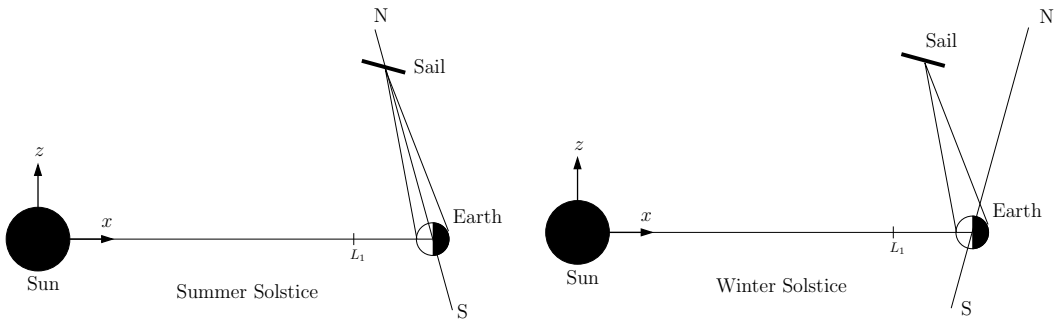

Figure 2.21: *Schematic representation of the Polar Observer Mission (not to scale).*

More details on the Polar Observer can be found in [McI99, McI03, MM04]. Nevertheless, this mission has not been as studied as the Geostorm mission, probably because that the sail must be displaced at about 3.9 million km from the Earth, having then low resolution imaging of the Poles. High performance solar sails are required to reduce this distance, not available for a near - term solar sail mission.

Mission orbit

In Figure 2.22 we have the position of the fixed points on the $Y = 0$ plane for different sail lightness numbers β. Notice that as the sail performance increases the equilibrium points come closer to the Earth. For our simulations we have considered $\beta = 0.14$.

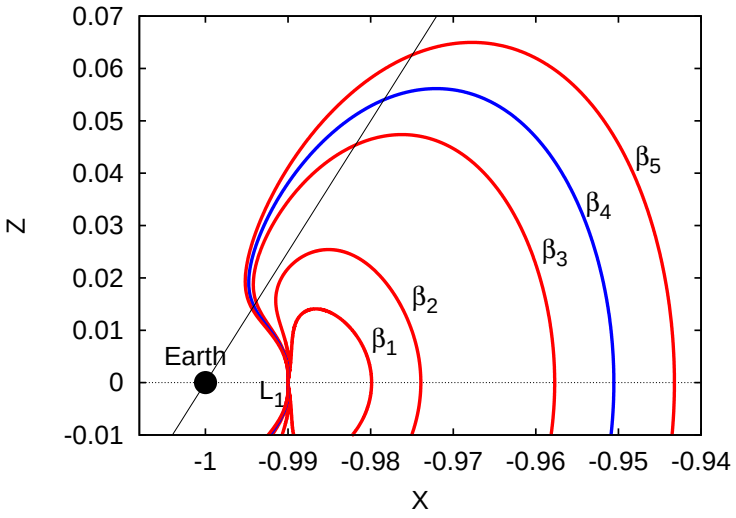

Figure 2.22: *Relation of the fixed point for different sail lightness numbers:* $\beta_1 = 0.052$, $\beta_2 = 0.072$, $\beta_3 = 0.12$, $\beta_4 = 0.14$, $\beta_5 = 0.16$.

We consider the fixed point $p_0 = (-0.9939071, 0, 0.01385977, 0, 0, 0)$ for $\alpha = 0$ and $\delta = 1.100593$ radians. In Table 2.7 we have the variation of the fixed point with respect to α and δ in the synodical reference system and in the eigenvector reference system. We can see that at first order, variations on α imply variations on the Y direction, while

$p^\star_\alpha$	0.000000e+00	-1.471302e-02	0.000000e+00	0.000000e+00	0.000000e+00	0.000000e+00
$p^\dagger_\alpha$	-5.154633e-03	5.154633e-03	-1.228042e-19	8.647821e-03	-3.134312e-19	-8.373897e-03
$p^\star_\delta$	8.685808e-01	-0.000000e+00	-2.450515e+00	0.000000e+00	0.000000e+00	0.000000e+00
$p^\dagger_\delta$	-6.135351e-03	-6.135351e-03	-5.413341e-02	3.816095e-17	-2.592667e+00	-1.145288e-16

Table 2.7: *For the Polar Observer: linear variation of the position of the fixed point* p_0 *w.r.t.* α *and* δ*, in the synodical reference system* (*) *and in the eigenvector reference system* (†)*. Where* p_α *stands for* $\partial p/\partial\alpha$ *and* p_δ *stands for* $\partial p/\partial\delta$*.*

variations in δ imply variation on X and Z. Notice that the variation on the Z direction is big, i.e. small variations on δ imply big variations on the vertical displacement of the fixed points. This can affect the controllability of the trajectory. If we look at the variation on the saddle projection, now variations on α and δ give variations on the 4 quadrants of this

plane, hence we have more choices to find appropriate equilibrium points by varying the sails orientation (remember that in the Geostorm Mission variation on the saddle plane where only given by variations in α). On the other hand, notice that on the second centre plane, the position of the fixed points is very sensitive to small changes on δ. This needs to be taken into account to maintain this centre projection small.

In Table 2.8 we have the eigenvalues and their variation w.r.t. α and δ. We can see that for small variations on the sail orientation the main instability of the region is given by the positive real eigenvalue. In Table 2.9 we can find the angles between the eigenvectors $\vec{v}_i$ and their linear variations $\partial\vec{v}_i/\partial\alpha$ and $\partial\vec{v}_i/\partial\delta$. We can see that the maximum variations are of order 0.01 radians, negligible for small variations on the sail orientation. Hence, the assumptions made on the control strategy also hold in this region.

i	λ_i	$\partial\lambda_i/\partial\alpha$	$\partial\lambda_i/\partial\delta$
0	1.105381e+00	6.962362e-05 - 0.000000e+00 i	-3.032041e-06 - 0.000000e+00 i
1	-1.105381e+00	6.962362e-05 - 0.000000e+00 i	3.032041e-06 - 0.000000e+00 i
2	1.787265e+00 i	1.340332e-04 + 0.000000e+00 i	0.000000e+00 - 9.773455e-07 i
3	-1.787265e+00 i	1.340332e-04 + 0.000000e+00 i	0.000000e+00 + 9.773455e-07 i
4	1.670802e-01 i	-2.036569e-04 + 5.221389e-20 i	-1.482689e-21 - 1.017370e-05 i
5	-1.670802e-01 i	-2.036569e-04 - 5.221389e-20 i	-1.482689e-21 + 1.017370e-05 i

Table 2.8: *For the Polar Observer: the eigenvalues (λ_i) and their variation w.r.t. α ($\partial\lambda_i/\partial\alpha$) and δ ($\partial\lambda_i/\partial\delta$).*

i	$\langle\vec{v}_i, \partial\vec{v}_i/\partial\alpha\rangle$	angle	$\langle\vec{v}_i, \partial\vec{v}_i/\partial\delta\rangle$	angle
1	9.9999970553e-01	7.674266e-04	9.9977511466e-01	2.120820e-02
2	9.9999970553e-01	7.674266e-04	9.9977511466e-01	2.120820e-02
3	9.9999488867e-01	3.197290e-03	9.9983102602e-01	1.838362e-02
4	9.9999488867e-01	3.197290e-03	9.9983102602e-01	1.838362e-02
5	9.9957615184e-01	2.911625e-02	9.7764425730e-01	2.118468e-01
6	9.9957615184e-01	2.911625e-02	9.7764425730e-01	2.118468e-01

Table 2.9: *For the Polar Observer: the scalar product and the angle (in rad) between $\vec{v}_i$ and $\partial\vec{v}_i/\partial\alpha$ and between $\vec{v}_i$ and $\partial\vec{v}_i/\partial\delta$ for $i = 1, \ldots, 6$.*

Results

We have done a Monte Carlo simulation using 1000 initial conditions chosen in a random way. For each simulations we have applied the control strategy up to 30 years and measured the time between manoeuvres, the variation of the sail orientation (α, δ) and the angular variation of the trajectory with respect to p_0.

On Figure 2.23 (left) we can see for each simulation the maximum and minimum time between manoeuvres. The mean minimum time between manoeuvres is always around 30 days and the mean maximum time is around 91 days. On Figure 2.23 (right) we have the maximum angular variation between the fixed point (p_0) and the probe's trajectory for each simulation, where the maximum variation experienced is around 0.51 degrees, that corresponds to a variation of 25209.69km. In these simulations we have seen that, at each manoeuvre, the maximum variation of α is of 0.56° and for δ it is of 0.0016°.

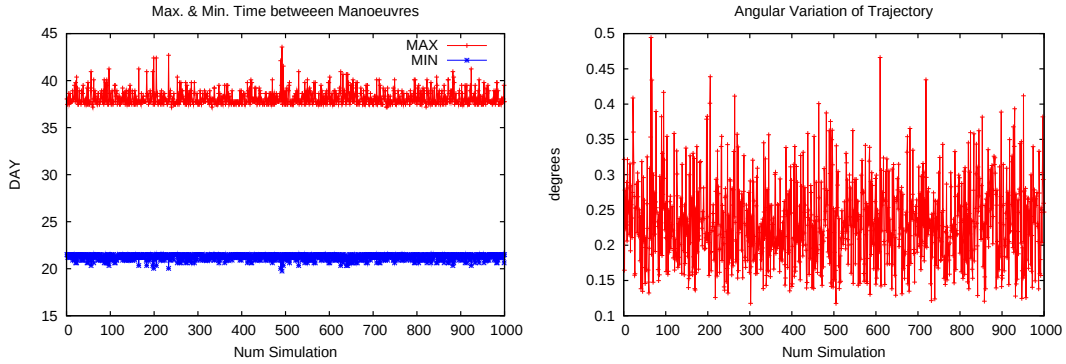

Figure 2.23: *For the Polar Observer: maximum and minimum time between manoeuvres* vs *number of simulation (left). Maximum angular variation between* p_0 *and the probe trajectory* vs *number of simulation (right).*

In Figure 2.24 we can see different projections of the trajectory of the probe for an arbitrary initial condition after applying the station keeping strategy for 30 years. Figure 2.25 we have the projection of the orbit on the saddle plane and the two centre directions. Finally, Figure 2.26 shows the variation of the sail orientation along time.

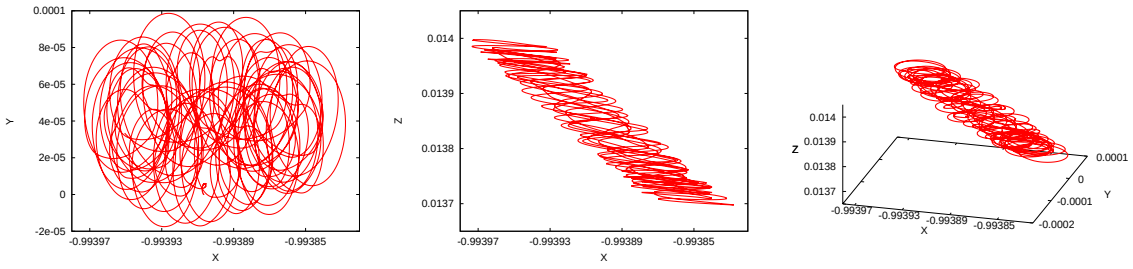

Figure 2.24: *For the Polar Observer: projections of the probe's trajectory for 30 years on the position space. From left to right:* XY *projection,* XZ *projection and* XYZ *projection.*

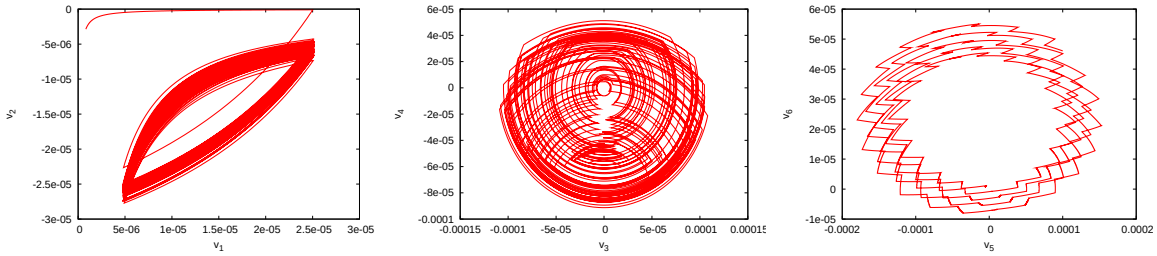

Figure 2.25: *For the Polar Observer: projections of the probe's trajectory for 30 years on the three reference planes. From left to right: saddle projection, projection on centre the plane generated by* $(\vec{v}_3, \vec{v}_4)$ *and projection on the centre plane generated by* $(\vec{v}_5, \vec{v}_6)$.

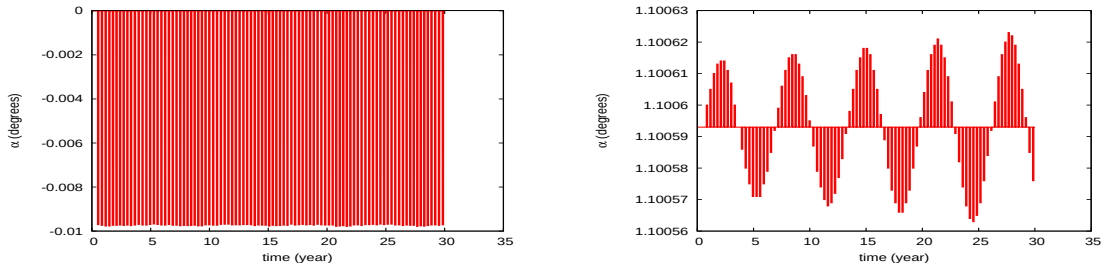

Figure 2.26: *For the Polar Observer: variation of the sail orientation along time. From left to right: variation of* α *and* δ.

2.4 Sensitivity to Errors

It is a known fact that during a mission the position and velocity of the probe will not be determined exactly, this has an effect on the decisions taken by the control algorithm. Errors on the sail orientation will also be made and have an important effect in the probe's trajectory. We will see the effect of these errors in our control strategy.

Let us start by only considering errors on the position and velocity determination of the probe. As we have seen in previous sections the sail orientation is changed when the probe is at a certain distance of the fixed point in the saddle plane projection. Each time the algorithm asks itself if the sail orientation has to be changed, the probe's position in the phase space has some small error. So errors on the measurement of the probe's position can make the algorithm change the sail orientation when not desired and the new fixed points position can also be modified. If this errors are not very big the difference between changing the sail orientation a little earlier or latter in time will not affect the control of the probe.

We have considered that all the errors follow a normal distribution with zero mean.

We have considered a precision on the position of the probe of $\approx$ 1m in the space slant and $\approx 2 - 3$milli-arc-seconds in the angle determination of the probe. The precision in speed is around $20 - 30$microns/seconds. These errors are introduced every time the control algorithm asks for the position of the probe to decide if a manoeuvre should be done or not. The effect of these errors turns out to be almost negligible.

We have performed more Monte Carlo simulations, using the same initial conditions as before but adding the uncertainty in the position and velocity. The results obtained are similar. For all the simulations (in both missions) the probe's trajectory does not escape after 30 years. The average time between manoeuvres is slightly changed and so are the angular variation in the trajectories position with respect to the initial fixed point (see Table 2.10 and 2.11).

Let us now consider errors on the sail orientation. Each time the sail orientation is changed an error in its orientation is made ($\alpha = \alpha_1 + \epsilon_\alpha$, $\delta = \delta_1 + \epsilon_\delta$). Then the new fixed point p_1 is shifted $p(\alpha, \delta) = p(\alpha_1, \delta_1) + \epsilon_p$ and so do the stable and unstable directions $\vec{v}_{1,2}(\alpha, \delta) = \vec{v}_{1,2}(\alpha_1, \delta_1) + \epsilon_v$. These variations can make the probe's trajectory not come close to p_0, as $p(\alpha, \delta)$ can be placed on the incorrect side of the saddle or the central behaviour can blow up. These errors have an important effect on the sail trajectory and on the controllability of the probe. Depending on the nature of the region close to the fixed point the control strategy will be able to deal with bigger errors in the sail orientation. It will all depend on the variation of the fixed point and the eigenvectors with respect to the sail orientation.

We have performed Monte Carlo simulations, taking the same initial conditions as before and introducing the uncertainties on sail orientation and the probe's position and velocity determination (see Table 2.10 and 2.11). We have considered that the errors on the sail orientation also follow a normal distribution with zero mean. For each mission we have taken different values for the sail orientation precision to check the robustness of our algorithm.

In Tables 2.10 and 2.11 we find the results of all these simulations for the Geostorm and Polar Observer missions respectively. In each table: the first line has the results for the simulations when no errors are taken into account; the second line has the results when only error on the position and velocity determination are made; the third and fourth line contains the results when all the errors are taken into account (sail orientation and position + velocity determination). Column 2 shows the % of simulations that succeed to control the probe; columns 3 and 4 have the average maximum and minimum time between manoeuvres respectively and column 5 has the average angular variation of the

trajectory seen from the Earth.

	% Success	Max. Time	Min. Time	Ang. Vari.
No Error	100 %	45.87 days	24.13 days	1.43°
Error Pos.	100 %	45.85 days	24.13 days	1.43°
Error Pos. & Orient. *	100 %	53.90 days	21.59 days	1.42°
Error Pos. & Orient. †	97 %	216.47 days	15.54 days	1.67°

Table 2.10: *Statistics for the Geostorm mission taking 1000 simulations. Considering errors on the sail orientation of order* 0.5° *(***) and* 2.2° *(*†*).*

	% Success	Max. Time	Min. Time	Ang. Vari.
No Error	100 %	91.10 days	30.61 days	0.51°
Error Pos.	100 %	91.12 days	30.60 days	0.51°
Error Pos. & Orient. *	100 %	94.03 days	30.04 days	0.56°
Error Pos. & Orient. †	93.1 %	152.32 days	28.61 days	1.32°

Table 2.11: *Statistics for the Polar Observer mission taking 1000 simulations. Considering errors on the sail orientation of order* 0.05° *(***) and* 0.28° *(*†*).*

In Table 2.10 we have the results for the Geostorm mission. We see that we have a 100 % of success on the 1000 simulations as long as the error on the sail orientation are less than 1.5°. We can also check that the errors on the position and velocity determination are negligible, and there is hardly any change on the final result if we only consider this sources of error. When we include larger errors on the sail orientation, we have no indicator if our station keeping algorithm will be able to maintain the probe close to the equilibrium point. Taking errors of 2.2° on the sail orientation we have a 97% percent of success.

Figures 2.27 and 2.28 show different projections of the trajectory of the probe when all the errors are considered, and Figure 2.29 shows the variation of the sail orientation along time. For this simulation we have considered errors on the sail orientation of order 0.5°.

For the Polar Observer mission, Table 2.11 shows that we have a 100% of success as long as the error on the sail orientation are less than 0.05°. A 6.9% of the 1000 simulations fail if we consider the errors on the sail orientation of order 0.28°. Again we can see that if we only consider errors on the position and velocity determination, the results are practically the same, only small changes on the time between manoeuvres.

Notice that the precision on the sail orientation required to have a 100% of success for the Geostorm Mission is less that the precision for the Polar Observer. This is due to the

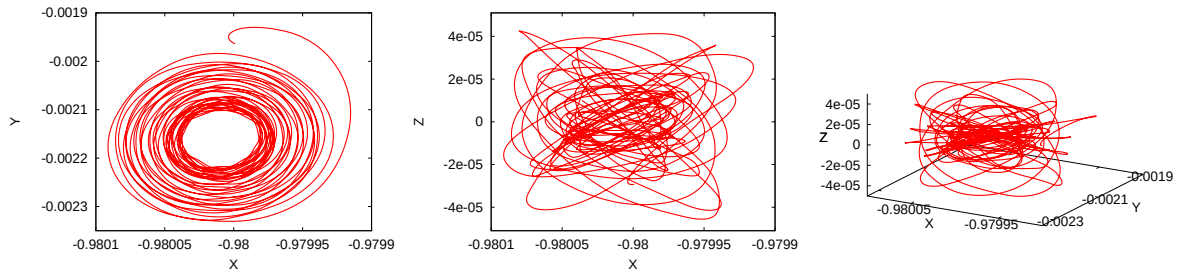

Figure 2.27: *For the Geostorm mission including all sources of error: projections on the position space of the probe's trajectory. From left to right: XY projection, XZ projection and XYZ projection.*

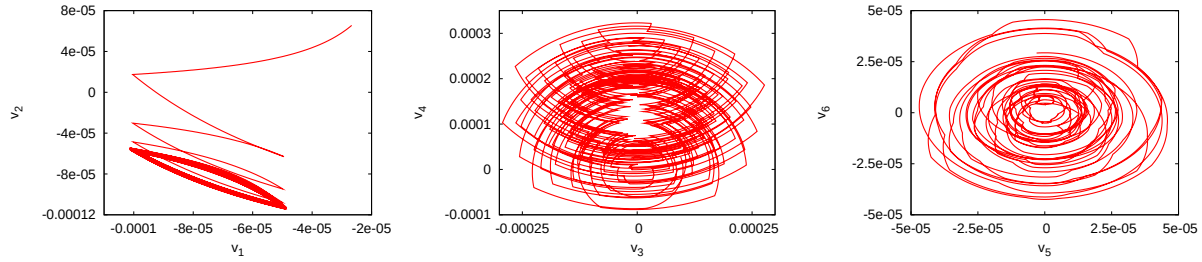

Figure 2.28: *For the Geostorm mission including all sources of error: projections on the three reference planes of the probe's trajectory. From left to right: the saddle projection, the centre projection defined by* $(\vec{v}_3, \vec{v}_4)$ *and the centre projection defined by* $(\vec{v}_5, \vec{v}_6)$.

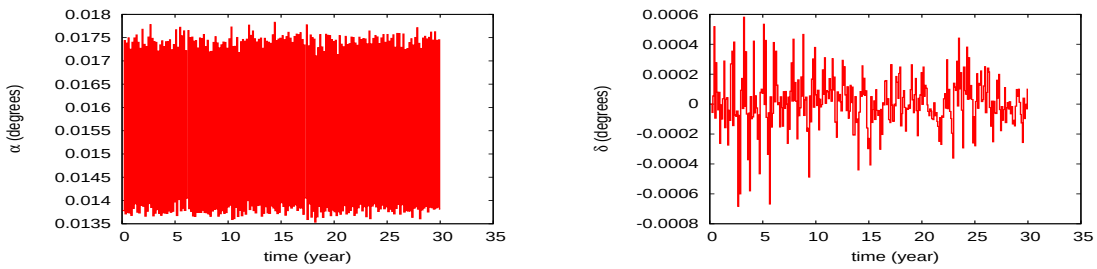

Figure 2.29: *For the Geostorm mission including all sources of error: variation of the sail orientation along time. From left to right: variation of* α *and* δ.

variation of the phase space properties when the sail orientation changes. As we have seen in the previous section, for the Polar Observer, small variations on δ give large vertical variation of the fixed points position. This makes it harder to deal with poor precision on the sail orientation as one of the centre projections will quickly grow. This is not the case for the Geostorm mission, where the variations on δ produce a better behaviour.

Finally, Figures 2.30 and 2.31 show different projections of the trajectory of the probe

when all the errors are considered, and in Figure 2.32 we have the variation of the sail orientation along time. For this simulation we have considered errors on the sail orientation of order 0.05°.

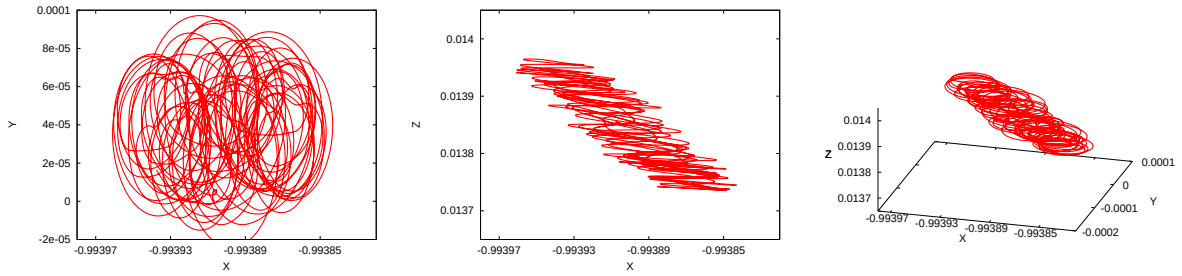

Figure 2.30: *For the Polar Observer including all sources of error: projections on the position space of the probe's trajectory. From left to right: XY projection, XZ projection and XYZ projection.*

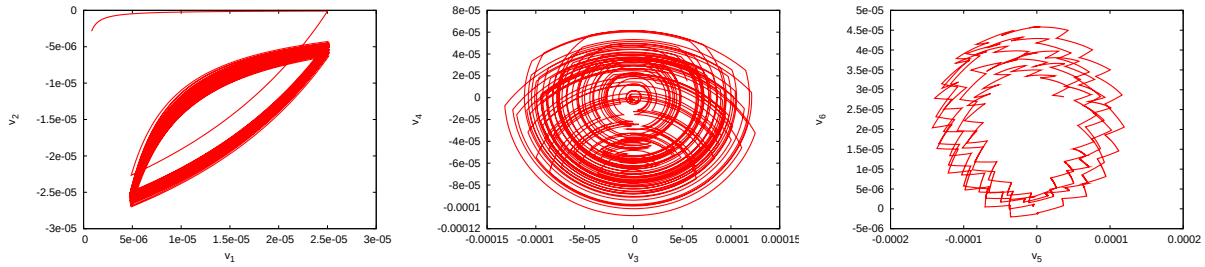

Figure 2.31: *For the Polar Observer including all sources of error: projections on the three reference planes of the probe's trajectory. From left to right: the saddle projection, the centre projection defined by $(\vec{v}_3, \vec{v}_4)$ and the centre projection defined by $(\vec{v}_5, \vec{v}_6)$.*

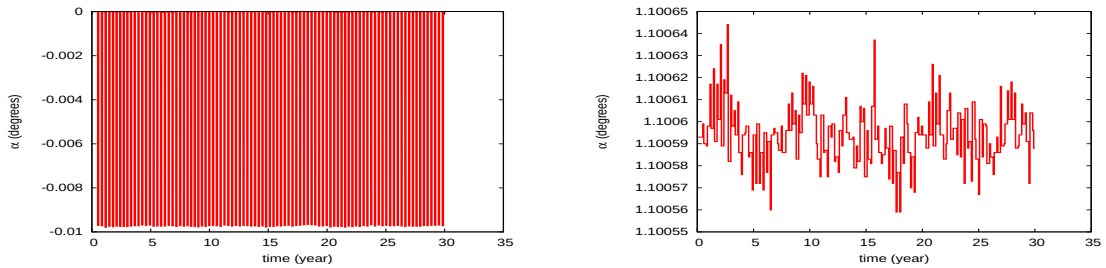

Figure 2.32: *For the Polar Observer including all sources of error: variation of the sail orientation along time. From left to right: variation of α and δ.*

2.5 Surfing Along the Families of Equilibria

Using the same ideas, we can derive strategies to drift along the families of equilibria in a controlled way. In the same philosophy as before, we use the invariant manifolds to move in the phase space. In this section we discuss how this can be done and we apply it to a couple of examples.

2.5.1 Surfing strategy

Let us assume that we are close to an equilibrium point p_0 and we want to reach the vicinity of another equilibrium point p_f. When we reach the final point p_f, we want to be able to remain there for a long time, i.e. to be able to apply a station keeping strategy with success.

As we know, when the probe is close to p_0 the trajectory escapes along the unstable direction. We want to find a sequence of changes on the sail orientation (α_i, δ_i) (i.e. a sequence of fixed points p_i) so that the sequence of stable/unstable directions of p_i guide the probe to the final point (see Figure 2.33).

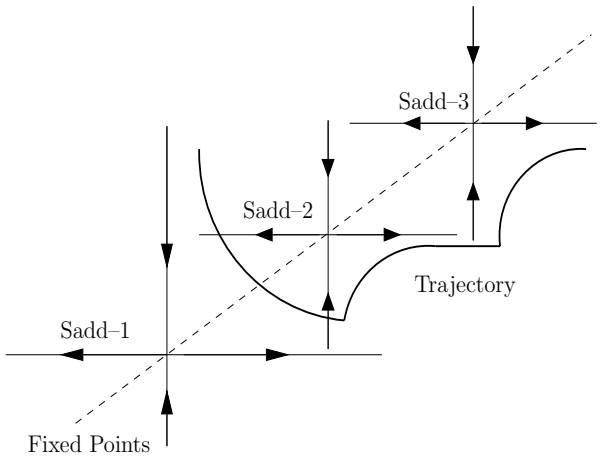

Figure 2.33: *Scheme of the idea to surf along the family of equilibria using the stable and unstable directions.*

It is not trivial to determine that given two equilibrium points, p_0 and p_f there will always be a sequence of changes on the sail orientation that can take us there. We need to have a connecting path between the stable and unstable direction of the sequence of fixed points, that take us to the final point p_f. Hence, we need to understand the dynamics of the region. Once we have the sequence of points, we can "surf" along the unstable manifolds, jumping from one equilibrium point to the other. We must never forget that

we need to take into account the centre behaviour, otherwise it may grow in an unbounded way.

We can define similar parameters as for the station keeping strategies to decide where we have to change to the new sail orientation. We will change the sail orientation once we reach the vicinity of the new equilibrium point in the sequence, or when we are escaping from the equilibrium point p_i. Using similar ideas as in Section 2.2.1 we find ideal positions for the new equilibrium point whose stable/unstable direction allows to move along the family.

We must not forget the centre behaviour of the trajectory. When the sail orientation varies, on the centre projection we have rotations around the different equilibrium points. These rotations can also produce an unbounded trajectory. Notice that if the changes on the sail orientation are small, the changes on the fixed point are also small, and the projection of the trajectory on a centre direction will be a spiral along the family of fixed points (see Figure 2.34). Nevertheless, we can use similar ideas as in Section 2.2.1 to find new sail orientations that minimise the centre oscillation. In any case, if the central behaviour starts to grow we could stop the "surfing" along the family of equilibrium points and perform a control strategy around the equilibrium point to try to reduce the central projection, and continue once this has been achieved.

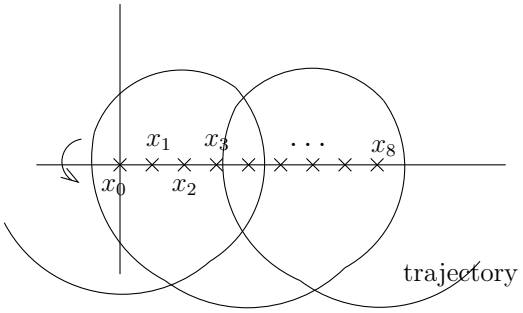

Figure 2.34: *Scheme of the centre projection of the trajectory when small changes in the sail orientation are made.*

2.5.2 Applications

Let us take the Geostorm scenario: a solar sail with a lightness number $\beta = 0.051689$ placed close to an equilibrium point displaced 5° from the Earth - Sun line at about $0.02AU$ from the Earth.

We propose two applications:

- **Mission 1:** Lets suppose that there has been a problem during the mission and that the sail is only displaced 2.5° from the Earth - Sun line. We want to surf along the family of equilibria to get close to an equilibrium point displaced 5° from the Earth - Sun line. On the left - hand side of Figure 2.35 we have a schematic representation of the main goal.

- **Mission 2:** Let us suppose that we have the sail close to an equilibrium point at about $0.02AU$ from the Earth displaced 5° from the Earth - Sun line on the ecliptic plane. We want to surf along the family to get close to a final point placed 5° above the ecliptic plane. On the right - hand side of Figure 2.35 we have a schematic representation of the main goal.

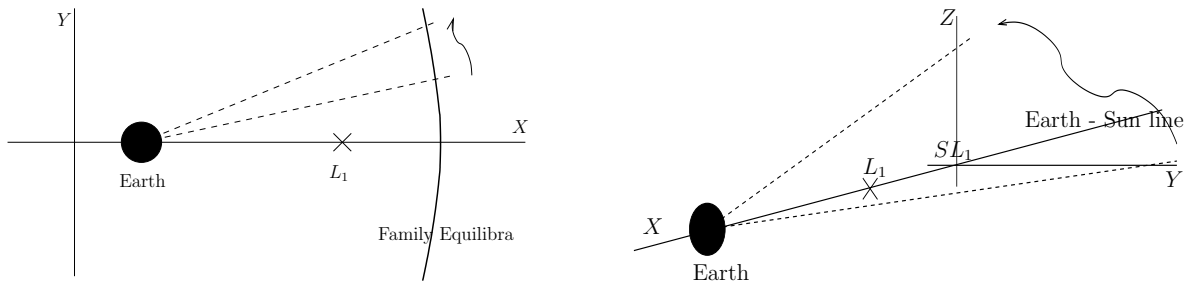

Figure 2.35: *Schematic representation of the two surfing mission applications. Mission 1 (right) and Mission 2 (left).*

Mission 1

We consider as initial and final equilibrium points, $p_0 = (-0.9799771, 0.0008283, 0, 0, 0, 0)$ and $p_f = (-0.9799984, 0.0018189, 0, 0, 0, 0)$ respectively. That are equilibrium points for a sail orientation $\alpha_0 = -0.335°$, $\delta_0 = 0°$ and $\alpha_f = -0.733°$, $\delta_f = 0°$. We have taken an arbitrary initial condition close to p_0 and applied the surfing strategy explained above, jumping from the vicinity of one equilibrium point to the other, until we get close to p_f.

It takes around 548 days to get to a close neighbourhood of p_f. Changes on the sail orientation have been done approximately every 145 days. In Figure 2.36 we show the variation of the sail orientation along time.

In Figures 2.37 we have different projections of the trajectory followed by the sail on the synodical reference system. Notice how the trajectory is always close to the family of equilibria, presenting small Z oscillations. In Figure 2.38 we have the projection of the trajectory on the reference system $\{p_0;\ \vec{v}_1, \cdots, v_6\}$. In the saddle projection $(\vec{v}_1, \vec{v}_2)$ we

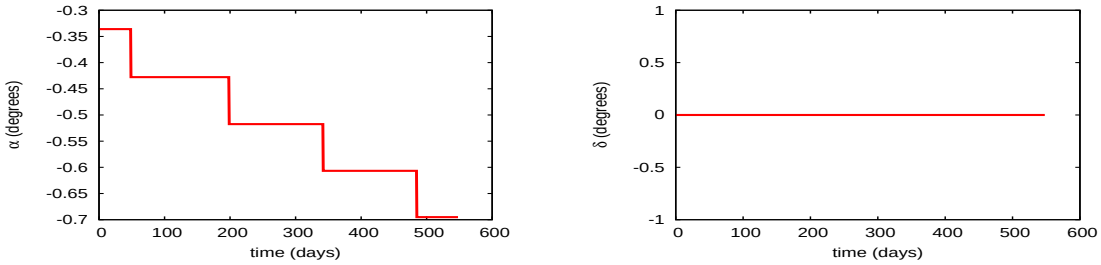

Figure 2.36: *For mission 1: variation of the sail orientation along time. From left to right: variation of α and δ.*

see the sequence of saddles that guide the trajectory along the family of equilibria. In the first centre projection $(\vec{v}_3, \vec{v}_4)$ we see that the trajectory rotates around the different equilibrium points and that it does not grow significantly along time.

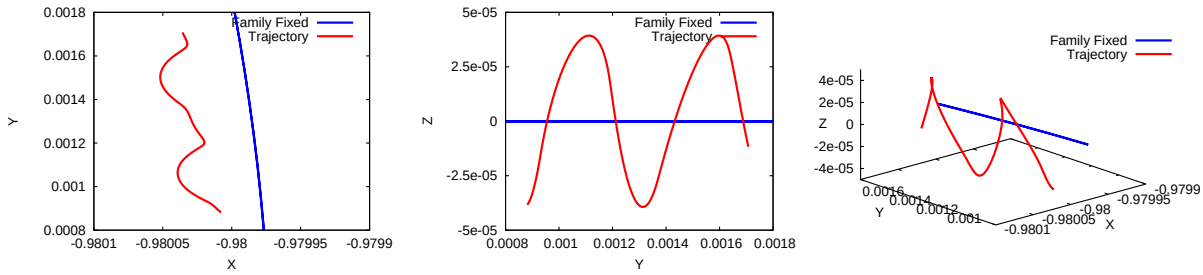

Figure 2.37: *For mission 1: projection of the trajectory on the position space. From left to right: XY projection, YZ projection and XYZ projection.*

Mission 2

Here we consider as initial equilibrium point $p_0 = (-0.9799984, 0.0018189, 0, 0, 0, 0)$ for $\alpha_0 = -0.733°$ and $\delta_0 = 0°$ on the ecliptic plane. We want to get to a final point above the ecliptic plane $p_f = (-0.9800368, 0, 0.0017395, 0, 0, 0)$ for $\alpha_f = 0°$ and $\delta_f = 2.564°$.

As in mission 1 we have taken an arbitrary initial condition and applied the surfing strategy to move along the family from the neighbourhood of p_0 until we get to a neighbourhood of p_f.

For this mission, it takes around 764 days to get from p_0 to p_f, having to change the sail orientation every $105 - 120$ days. In Figure 2.39 we see the variation of the sail orientation along time. In Figure 2.40 we have different projections of the trajectory followed by the sail on the synodical reference system. Notice how the trajectory increases the Z coordinate as the sail orientation is changed, which is mainly affected by the changes

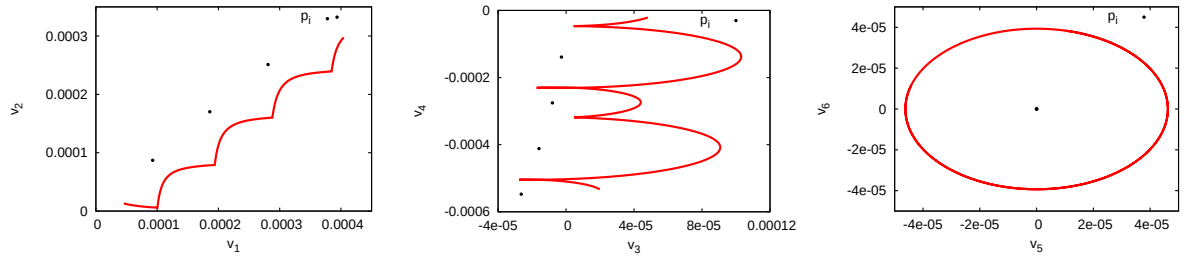

Figure 2.38: *For mission 1: projection of the trajectory on the three reference planes around p_0. From left to right: the saddle projection and the two centre projections.*

in the angle δ. Finally, in Figure 2.41 we have the projection of the sail trajectory on the eigenvector reference system close to p_0. Here we can also observe how the unstable directions guide the trajectory along the family of equilibria and the centre projections of the trajectory remains close to sequence of equilibrium points p_i at all time.

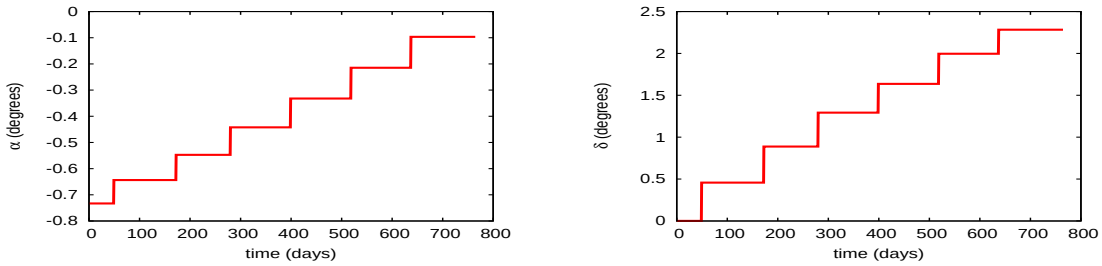

Figure 2.39: *For mission 2: variation of the sail orientation along time. From left to right: variation of α and δ.*

2.6 Conclusions

In this Chapter we have presented a station keeping technique for a solar sail close to an unstable equilibrium point using dynamical system tools. We have studied the natural dynamics of the system close to an equilibrium point and its variation when the sail orientation (α, δ) is changed. This knowledge has permitted us to derive a station keeping strategy to maintain a probe's trajectory close to an unstable equilibrium.

We have tested this strategy with two different missions, the 'Geostorm Warning Mission' and the 'Polar Observer'. In both cases the probe manages to stay close to the fixed point for at least 30 years. We have also tested the controllability of the algorithm including systematic errors in the prediction of the sail's position and velocity, and errors

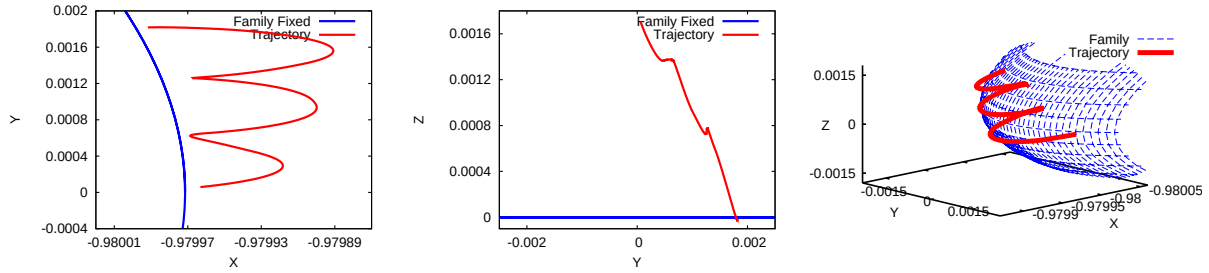

Figure 2.40: *For mission 2: projection of the trajectory on the position space. From left to right: XY projection, YZ projection and XYZ projection.*

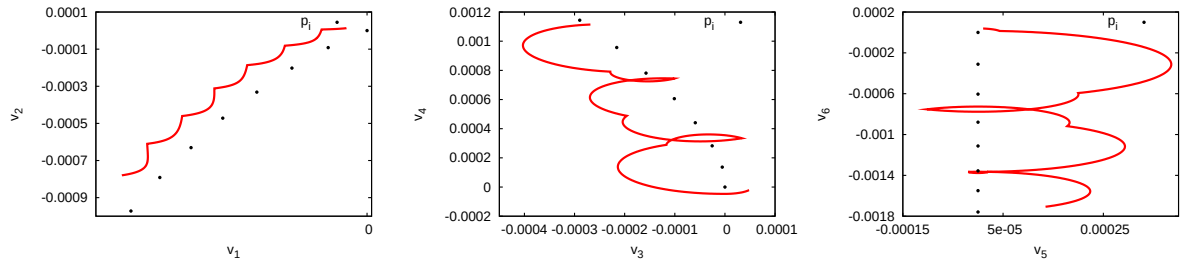

Figure 2.41: *For mission 2: projection of the trajectory on the three reference planes around p_0. From left to right: the saddle projection and the two centre projections.*

in the sail orientation angles (α, δ). We have seen that the errors on the position and velocity do not produce important changes in the sail's trajectory and its controllability. On the other hand, errors on the sail's orientation are more relevant and give more variations on the final probe's trajectory.

In the literature we find studies related with the controllability of the sail close to SL_1, specially for the Geostorm mission application. All these station keeping strategies use optimisation techniques. The main difference appears in the final result, the steering law obtained. With our strategies we find discrete changes on the sail orientation, while using optimisation tools one usually finds a continuous function for the variation of the sail orientation. But the magnitude of variation on the sail orientation is essentially the same. It is yet to decide which kind of strategy is more feasible from a practical point of view. On the other hand, we have not found studies on the robustness of these strategies with different sources of errors. Hence we have not been able to compare our results. Further studies should be done if we want to deal with more imprecision on the sails orientation.

We have seen that the controllability of the sail is strictly related to the nature of the neighbourhood of the fixed point where we want to keep the sail. If the variations

of the fixed points and the eigenvectors are understood, we can understand the dynamics and, therefore, the reasons that make the control more or less difficult to implement. For instance, in the Polar Observer Mission, more precision on the sail orientation is required to be able to control the probe, as the position of the fixed points is very sensitive to variations in one of the angles. Further studies should be done to modify our control algorithm to deal with larger errors. Second order approximations of the invariant manifolds and fixed point surfaces could be considered.

Let us mention that the strategy proposed here does not require previous planning, the decisions taken by the probe depend only on its position in phase space, that is known at each moment. In this way, it is not necessary to have to plan the control strategy in advance and errors made during the manoeuvres can be rectified easily.

Finally, we have used these ideas to derive a way to move along the family of unstable equilibrium points. As a particular case we have chosen to go from a fixed point displaced 5^o on the Sun - Earth line to a fixed point at 10^o of this line. Nevertheless, the same techniques are valid to move along the family of unstable equilibrium points, as long as there is a path of stable and unstable manifolds that leads us from one place to the other.

All the strategies presented here are based on the knowledge of the natural dynamics of the system. Understanding how the invariant manifolds vary as the sail orientation is changed has been the key of to this work. In this work we have only used the information given by linear dynamics. This is useful if we want to be close to the equilibrium points, but might be a constraint in some cases. We should use higher order terms to go further away of the equilibrium point.

Chapter 3

Reduction to the Centre Manifold

In this Chapter, we will focus on the equilibrium points whose linear dynamics is of the type centre $\times$ centre $\times$ saddle. Most of these points are found close to the Earth - Sun line. Our aim is to have a complete understanding of the dynamics on an extended neighbourhood of them. We are interested in finding trajectories that remain close to the equilibrium point. It is a known fact that if we take arbitrary initial conditions and just integrate them numerically, the solution will escape from a vicinity of the point with probability one, due to the unstable character of the fixed point. For this reason, we propose to do the reduction to the centre manifold around one of these equilibrium points. The centre manifold is an invariant manifold tangent, at the equilibrium point, to the two centre directions. In general, the centre manifold is not unique, but its Taylor series at the equilibrium point is, for further details see [Car81, Sij85, Van89].

To approximate the centre manifold, we expand the equations of motion around the equilibrium point and uncouple up to high order the hyperbolic directions from the elliptic ones. Then, neglecting the reminder we have a high order approximation of the centre manifold. We use this approximation for numerical integrations and to have a good understanding of the bounded motions.

Classically, in celestial mechanics, e.g. the RTBP, the system is Hamiltonian. Hence, one can take advantage of the Hamiltonian character of the system to compute the reduction to the centre manifold. This is usually done expanding the Hamiltonian around the equilibrium point and performing canonical transformations on the Hamiltonian to uncouple the two behaviours. This procedure is similar to the computation of the normal form, but here we suppress less monomials. In [GJMS01, Jor99, JM99] one can find the methodology to compute the reduction to the centre manifold for a collinear point of the RTBP. Moreover, in [Jor] we can find a public domain library that deals with this

problem.

Nevertheless, in Chapter 1 we have seen that when the sail is not perpendicular to the Sun - line, the system is no longer Hamiltonian, but there are still centre $\times$ centre $\times$ saddle equilibrium points. Hence, we need to develop a tool that is also useful for these other cases.

In this Chapter we use an alternative way to do the reduction to the centre manifold, that does not take into account the Hamiltonian character of the system. We will take the whole set of equations and compute, formally, the power series representation of the graph of the centre manifold at the equilibrium point. This is called the graph transform method and it is a more general procedure that can be used for a more general set of equations [Sim90]. Moreover, we compare the efficiency of our method with the classical approach for Hamiltonian systems [Jor99]. We have considered the problem when the sail is perpendicular to the Sun - line, i.e the system is Hamiltonian, and computed the reduction to the centre manifold using both methods.

In Section 3.1 we give the details for the computation of the centre manifold using the graph transform method. We also discuss some tricks that we have implemented to have an efficient algorithm. In Section 3.2 we give the main ideas for the reduction to the centre manifold using a Lie series approach. Here we have taken the software in [Jor] and modified it to deal with our problem. Finally, we test and compare both methods. Surprisingly as it might seem, as we will see in Section 3.3, the direct application of the graph transform method is more efficient than taking into account the Hamiltonian structure of the system. In Chapter 4 we will use the reduction to the centre manifold to understand the non - linear dynamics close to equilibria.

For the sake of simplicity, we always consider that we have a fixed point of the type centre $\times$ centre $\times$ saddle, as this is the case for the displaced collinear points $SL_{1,2,3}$. However, the same techniques can be extended in an easy way for a more general case when the system has several "centres" and "saddles" [Sim90].

As the commercial algebraic manipulators are not efficient enough to deal with big expansions, we have written our own software from scratch, using ANSI C language. The algebraic manipulator used here is explained in full detail in [Jor99]. The programs are built in different layers. In the bottom layer we have the routines to handle polynomials. Built on top, are the routines using the algorithms for the actual reduction to the centre manifold that we will explain in what follows.

To fix notation, if $z = (z_1, \ldots, z_\ell)$ is a vector of complex numbers and $k = (k_1, \ldots, k_\ell)$ a vector of natural numbers, we denote $z^k = z_1^{k_1} \cdots z_\ell^{k_\ell}$ (here, $0^0 = 1$). Moreover, we

define $|k| = k_1 + \cdots + k_\ell$.

3.1 Graph Transform

Let $\dot{z} = F(z)$, $z \in \mathbb{R}^6$ be an ordinary differential equation with a fixed point of the type centre $\times$ centre $\times$ saddle. Without loss of generality we can assume that the fixed point is at the origin. It is well known that with an appropriate linear transformation, the equations of motion can be written as:

$$\begin{aligned} \dot{x} &= Ax + f(x, y), \\ \dot{y} &= By + g(x, y), \end{aligned} \tag{3.1}$$

where $x \in \mathbb{R}^4$, $y \in \mathbb{R}^2$, all the eigenvalues of the matrix A have zero real part and all the eigenvalues of the matrix B are real. The functions f and g are sufficiently smooth and satisfy,

$$f(0,0) = 0, \qquad Df(0,0) = 0, \qquad g(0,0) = 0, \qquad Dg(0,0) = 0.$$

Note that $y = 0$ is the linear approximation to the centre manifold. We want to find $y = v(x)$ with $v(0) = 0$ and $Dv(0) = 0$, the local expression of the centre manifold. If we substitute this on equations (3.1), we have that $v(x)$ must satisfy:

$$Bv(x) + g(x, v(x)) = Dv(x)[Ax + f(x, v(x))], \tag{3.2}$$

and the flow restricted to the manifold is given by,

$$\dot{x} = Ax + f(x, v(x)). \tag{3.3}$$

For more details see for instance [Car81]. Although the centre manifold might not be unique, its Taylor expansion at the equilibrium point is.

We want to find the Taylor expansion of the graph of the centre manifold at the equilibrium point, $v(x)$, truncated at high order. We call this high order approximation $\widehat{v}(x)$. Then we can take,

$$\dot{x} = Ax + f(x, \widehat{v}(x)), \tag{3.4}$$

to have a high order approximation of the motion on the centre manifold.

3.1.1 Scheme of the computation

Let us assume that we have already made a linear change of variables and set the equations as in (3.1) and let $\pm\lambda$, $\pm \mathrm{i}\,\omega_1$ and $\pm \mathrm{i}\,\omega_2$ be the eigenvalues of $D_x F$. We want to find $y = v(x)$ that satisfies equation (3.2).

We take $v(x) = \sum_{|k|\geq 2} v_k x^k$, with $v_k \in \mathbb{R}^2$, the formal power expansion of $v(x)$ around the origin. We are interested in knowing the values $v_k = (v_k^1, v_k^2)$ up to high order to have a good approximation of the centre manifold near the point. For instance, if we have $\widehat{v}(x) = \sum_{|k|=2}^{N} v_k x^k$ that satisfies equation (3.2) up to order N, then $\widehat{v}(x)$ approximates the graph of the centre manifold up to the same order, i.e. $||v(x) - \widehat{v}(x)|| = O(||x||^N)$.

Notice that equation (3.2) can be rewritten as,

$$Dv(x)Ax - Bv(x) = g(x, v(x)) - Dv(x)f(x, v(x)), \tag{3.5}$$

where, the left - hand side of this equation is a linear operator w.r.t. $v(x)$ and the right - hand side a non linear one.

If we assume A and B to be in diagonal form, $A = \mathrm{diag}(\mathrm{i}\,\omega_1, -\mathrm{i}\,\omega_1, \mathrm{i}\,\omega_2, -\mathrm{i}\,\omega_2)$ and $B = \mathrm{diag}(\lambda, -\lambda)$, then the left - hand side of equation (3.5) also takes a diagonal form,

$$Dv(x)Ax - Bv(x) = \begin{pmatrix} \displaystyle\sum_{|k|\geq 2} (\mathrm{i}\,\omega_1 k_1 - \mathrm{i}\,\omega_1 k_2 + \mathrm{i}\,\omega_2 k_3 - \mathrm{i}\,\omega_2 k_4 - \lambda)\ v_{1,k}\ x^k \\ \\ \displaystyle\sum_{|k|\geq 2} (\mathrm{i}\,\omega_1 k_1 - \mathrm{i}\,\omega_1 k_2 + \mathrm{i}\,\omega_2 k_3 - \mathrm{i}\,\omega_2 k_4 + \lambda)\ v_{2,k}\ x^k \end{pmatrix}. \tag{3.6}$$

Let $h(x) = g(x, v(x)) - Dv(x)f(x, v(x))$ be the right hand side of equation (3.5). We take its expansion $h(x) = \sum_{|k|\geq 2} h_k x^k$ around the origin ($h_k = (h_k^1, h_k^2)$), where the coefficients h_k depend on the coefficients v_k in a known way. As we will see in Lemma 3.1.2 the coefficients h_k for $|k| = n$ depend on v_k with $|k| < n$. This allows us to find the v_k in an iterative way.

Let us see how to arrange the terms v_k of degree 2. We take the power expansion of $f(x, y)$ and $g(x, y)$ around the origin,

$$f(x,y) = \sum_{|k_1|+|k_2|\geq 2} f_{k_1,k_2} x^{k_1} y^{k_2}, \qquad g(x,y) = \sum_{|k_1|+|k_2|\geq 2} g_{k_1,k_2} x^{k_1} y^{k_2},$$

where the $f_{k_1,k_2} \in \mathbb{R}^4$ and $g_{k_1,k_2} \in \mathbb{R}^2$ are known. Now we take $v(x)$ up to degree 2,

$$v(x) = \sum_{|k|=2} v_k x^k,$$

and we substitute this on equation (3.5) and equalise the terms of degree 2. As $Dv(x)$ and $f(x, v(x))$ start with monomials of degree 1 and 2 respectively, their product $Dv(x)f(x, v(x))$ starts with monomials of degree 3. Hence, for $|k| = 2$, $h_k = g_{k,0}$. Then the degree 2 terms on equation (3.5) satisfy,

$$\sum_{|k|=2} (\mathrm{i}\,\omega_1 k_1 - \mathrm{i}\,\omega_1 k_2 + \mathrm{i}\,\omega_2 k_3 - \mathrm{i}\,\omega_2 k_4 \mp \lambda) v_k x^k = \sum_{|k|=2} g_{k,0} x^k,$$

as $\lambda \neq 0$, we can find all the coefficients v_k, by equalising each of the monomials with $|k| = 2$. Having:

$$v_k^1 = \frac{g_{k,0}^1}{\mathrm{i}\,\omega_1 k_1 - \mathrm{i}\,\omega_1 k_2 + \mathrm{i}\,\omega_2 k_3 - \mathrm{i}\,\omega_2 k_4 - \lambda}, \quad v_k^2 = \frac{g_{k,0}^2}{\mathrm{i}\,\omega_1 k_1 - \mathrm{i}\,\omega_1 k_2 + \mathrm{i}\,\omega_2 k_3 - \mathrm{i}\,\omega_2 k_4 + \lambda}.$$

To arrange the higher order terms we proceed in the same way. For a given degree $\ell > 2$, we:

1. Take $v(x)$ up to degree ℓ, $\left(\sum_{|k|\geq 2}^{\ell} v_k x^k\right)$.

2. Substitute it on equation (3.5) and find the values of the coefficients h_k for $|k| = \ell$. Notice that the coefficients h_k depend on the coefficients f_{k_1,k_2}, g_{k_1,k_2} with $|k_1|+|k_2| \leq \ell$ and v_k with $|k| < \ell$.

3. Finally, we equalise the degree ℓ terms on equation (3.5), and solve the diagonal system to find the coefficients v_k for $|k| = \ell$.

This process is carried out for $\ell = 3, 4, \ldots$, up to a sufficiently high order N. In the end we have the expansion $\widehat{v}(x)$ up to degree N, a high order approximation of the centre manifold ($||v(x) - \widehat{v}(x)|| = O(x^N)$):

$$\widehat{v}(x) = \sum_{|k|\geq 2}^{N} v_k x^k. \tag{3.7}$$

Once we have $\widehat{v}(x)$, we are ready to explore the phase space. We will use equation (3.4) to integrate the flow, as it gives a high order approximation of the motion on the centre

manifold. Notice that during the reduction process we also compute $f(x, \widehat{v}(x))$, so we can store it while we are computing it.

We must recall, that we can find the coefficients v_k in an iterative way solving a diagonal linear system degree by degree, because the coefficients h_k for $|k| = \ell$, depend on the coefficient of v_k with $|k| < \ell$ (Lemma 3.1.2) and the matrices A and B are in diagonal form.

Remark The linear system can be solved if and only if

$$\mathrm{i}\,\omega_1 k_1 - \mathrm{i}\,\omega_1 k_2 + \mathrm{i}\,\omega_2 k_3 - \mathrm{i}\,\omega_2 k_4 \mp \lambda \neq 0.$$

Which is always true as $\lambda \in \mathbb{R}\backslash\{0\}$ and $\mathrm{i}\,\omega_1, \mathrm{i}\,\omega_2$ are pure imaginary numbers.

Remark It is not necessary to have A and B in their diagonal form, but then the linear part of equation (3.5) will not take a diagonal form. Then, as we increase the degree, the dimension of the linear system we have to solve increases and so does the computational cost and error propagation to solve it.

Remark To have A in its diagonal form, we need to take an initial complex change of variables. Hence, we need to apply the inverse of this change to the final representation $\widehat{v}(x)$ in the real set of coordinates.

Remark To have an efficient algorithm, we need to find an efficient way to compute the coefficients h_k. These coefficients come from the expansion around the origin of

$$h(x) = g(x, v(x)) - Dv(x)f(x, v(x)).$$

Expanding $g(x, y)$ and $f(x, y)$ and then composing with $v(x)$ is NOT an option, the composition of multivariate series is very expensive in terms of computational time. Instead, we propose to find recurrent expressions for the expansion of these functions and use them to obtain a more efficient algorithm. See the next section for further details.

3.1.2 Efficiency considerations

Let us see how to use recurrent expressions for the expansion of functions $f(x, y)$ and $g(x, y)$ around the origin to derive an efficient algorithm to compute the coefficients h_k of the Taylor expansion of $h(x) = g(x, v(x)) + Dv(x)f(x, v(x))$.

Let us assume, that we have:

$$f(x,y)=\sum_{n\geq 2}F_n(x,y),\qquad g(x,y)=\sum_{n\geq 2}G_n(x,y),$$

where $F_n(x,y)$ and $G_n(x,y)$ are homogeneous polynomials of degree n that are found in a recurrent way. This means, that there exist two functions $R_1(\zeta_1,\ldots,\zeta_j)$ and $R_2(\zeta_1,\ldots,\zeta_j)$ such that,

$$F_{n+1}=R_1(F_n,\ldots,F_{n-j}),\qquad G_{n+1}=R_2(G_n,\ldots,G_{n-j}),\tag{3.8}$$

where the $F_2,\ldots,F_j$ and $G_2,\ldots,G_j$ are known, and R_1 and R_2 only contain simple arithmetic operations between polynomials $(+/-/\times)$.

Let us start with a couple of lemmas on these recurrences and polynomial expressions.

Lemma 3.1.1 *Let $f:\ \mathcal{U}_1=\overset{\circ}{\mathcal{U}_1}\subset\mathbb{R}^4\times\mathbb{R}^2\mapsto\mathbb{R}^m$, with $0\in\mathcal{U}_1$, $m>0$, and $v:\ \mathcal{U}_2=\overset{\circ}{\mathcal{U}_2}\subset\mathbb{R}^4\mapsto\mathbb{R}^2$, with $0\in\mathcal{U}_2$ be two $\mathcal{C}^\infty$ functions, such that,*

$$f(x,y)=\sum_{n\geq 2}F_n(x,y),\quad v(x)=\sum_{n\geq 2}V_n(x),\quad \textit{on a neighbourhood of 0,}$$

where $F_n(x,y)$ and $V_n(x)$ are homogeneous polynomials of degree n. Then,

(a) $F_n(x,v(x))$ is a polynomial that starts at degree n.

(b) the coefficients of $F_n(x,v(x))$ that depend on the coefficients of $v(x)$ are of degree $r\geq n+1$.

(c) the coefficients of $F_n(x,v(x))$ of degree r depend on the coefficients of $v(x)$ of degree $k<r$.

It immediately follows that the coefficients of $f(x,v(x))$ of degree r depend on the coefficients of $v(x)$ of degree $k<r$.

Proof Let us start by taking a homogeneous polynomial of $f(x,y)$ of degree n. It is clear that $F_n(x,y)$ can be expressed as,

$$F_n(x,y)=\sum_{|k_1|+|k_2|=n}f_{k_1,k_2}x^{k_1}y^{k_2},\qquad k_1\in(\mathbb{N}\cup\{0\})^4,\ k_2\in(\mathbb{N}\cup\{0\})^2$$

where f_{k_1,k_2} are the coefficients of the homogeneous polynomial. Then,

$$F_n(x,v(x)) = \sum_{|k_1|+|k_2|=n} f_{k_1,k_2} x^{k_1} \left(\sum_{i\geq 2} V_i(x)\right)^{k_2}.$$

Notice that $\left(\sum_{i\geq 2} V_i(x)\right)^{k_2}$ is a polynomial that starts at degree $2|k_2|$. Hence, the coefficients of $F_n(x,v(x))$ have at least degrees $|k_1|+2|k_2|$. Assuming that $|k_1|+|k_2|=n$, the minimum takes place for $|k_2|=0$, hence $F_n(x,v(x))$ is a homogeneous polynomial that starts at degree n.

Let us now take a look on which coefficients of $F_n(x,v(x))$ depend on the coefficients of $v(x)$. It is clear that the monomials that depend on the coefficient of $v(x)$ come from the terms $f_{k_1,k_2}x^{k_1}\left(\sum_{i\geq 2} V_i(x)\right)^{k_2}$ with $|k_2|\neq 0$. As we have already seen, these terms have degree at least $|k_1|+2|k_2|$. As $|k_1|+|k_2|=n$, then $|k_1|+2|k_2| = n+|k_2|$. Hence, the terms $f_{k_1,k_2}x^{k_1}\left(\sum_{i\geq 2} V_i(x)\right)^{k_2}$ that depend on the coefficients of $v(x)$ are of degree at least $n+1$.

Let $\widetilde{f}_k x^k$ be a monomial of $F_n(x,v(x))$ of degree $|k|=r\geq n+1$. Hence, as already seen, it depends on the coefficients of $v(x)$. We want to see that $\widetilde{f}_k$ depends on coefficient of $v(x)$ of degree less that r.

Let us take a coefficient v_k of degree $|k|=s$ on $v(x)$, and see to what degree it corresponds after the composition. Notice that if we take a coefficient of degree s on $(\sum_{i\geq 2} V_i(x))^{k_2}$, it ends up appearing in different monomials. As $1\leq |k_2|\leq n$, we can say that the monomials of minimum degree in which it will appear are of degree s for $|k_2|=1$ and $s+1$ for $|k_2|>1$.

We take $f_{k_1,k_2}x^{k_1}\left(\sum_{i\geq 2} V_i(x)\right)^{k_2}$. Now the coefficients of $v(x)$ are being multiplied by x^{k_1}, hence the minimal degrees s for $|k_2|=1$ and $s+1$ for $|k_2|>1$, are now, $s+|k_1|$ for $|k_2|=1$ and $s+1+|k_1|$ for $|k_2|>1$. Finally, as $|k_1|+|k_2|\geq 2$ we can assure that a coefficient of degree s on $v(x)$ will end up appearing on a coefficient of degree $s+1$ on $F_n(x,v(x))$. Hence, if $\widetilde{f}_k$ is a coefficient of degree $|k|=r$ on $F_n(x,v(x))$, it can only depend on coefficients of $v(x)$ of degree at most $r-1$.

□

Lemma 3.1.2 *Let* $h:\mathcal{U}=\mathring{\mathcal{U}}\subset\mathbb{R}^4\mapsto\mathbb{R}^2$, *with* $0\in\mathcal{U}$ *be a* C^∞ *function defined as:*

$$h(x) = g(x,v(x)) - Dv(x)f(x,v(x)),$$

where $f:\mathcal{U}_1=\mathring{\mathcal{U}}_1\subset\mathbb{R}^4\times\mathbb{R}^2\mapsto\mathbb{R}^4$, $g:\mathcal{U}_2=\mathring{\mathcal{U}}_2\subset\mathbb{R}^4\times\mathbb{R}^2\mapsto\mathbb{R}^2$, $v:\mathcal{U}_3=\mathring{\mathcal{U}}_3\subset\mathbb{R}^4\mapsto\mathbb{R}^2$,

with $0 \in \mathcal{U}_i$ *for* $i = 1, 2, 3$, $f, g, v \in \mathcal{C}^\infty$ *and that satisfy,*

$$f(0,0) = 0,\ Df(0,0) = 0; \quad g(0,0) = 0,\ Dg(0,0) = 0; \quad v(0) = 0,\ Dv(0) = 0.$$

Then, the coefficients of the Taylor expansion of $h(x)$*, of degree* n *depend on the Taylor coefficients of* $v(x)$ *of degree* $k < n$*.*

Proof It is clear that the Taylor expansions of $f(x, y)$, $g(x, y)$ and $v(x)$ around the origin can be written as:

$$g(x,y) = \sum_{n\geq 2} G_n(x,y), \quad f(x,y) = \sum_{n\geq 2} F_n(x,y), \quad v(x) = \sum_{n\geq 2} v_n(x),$$

where $G_n(x, y)$, $F_n(x, y)$ and $V_n(x)$ are homogeneous polynomials of degree n. From Lemma 3.1.1 we have that the coefficients of the Taylor expansion of $g(x, v(x))$ and $f(x, v(x))$ of degree n depend only on the coefficients of the Taylor expansion of $v(x)$ of degree $r < n$.

It is also clear that the coefficients on the Taylor expansion of $Dv(x)$ of degree n now depend on the coefficients of $v(x)$ of degree $n + 1$. To prove the lemma we just need to see that the coefficients of degree n of $Dv(x)f(x, v(x))$ depend only on the coefficients of $v(x)$ of degree $k < n$.

Notice that $f(x, v(x))$ starts at degree 2, then if you take an element of degree s on $Dv(x)$, it will be of degree at least $s + 2$ on $Dv(x)f(x, v(x))$. Hence, the coefficients of n on $v(x)$, will appear only on the coefficients of degree at least $n + 1$ on $Dv(x)f(x, v(x))$.

□

Lemma 3.1.2 assures that the algorithm for the reduction to the centre manifold, explained above, can be applied in an iterative way.

Now, let us focus on the efficient computation of the coefficients of $h(x)$. We recall that

$$h(x) = g(x, v(x)) + Dv(x)f(x, v(x)). \tag{3.9}$$

We will use the recurrent expressions (3.8) for the coefficients of $g(x, y)$ and $f(x, y)$.

Let us assume that we know $v(x)$ up to degree r and we want to find the coefficients of degree $r + 1$. Hence, as mentioned in Section 3.1.1 we first need to find the coefficients of $h(x)$ of degree $r + 1$ and then solve the diagonal linear system (3.5). We start by finding the coefficients of $f(x, v(x))$ and $g(x, v(x))$ of degree $r + 1$. Once this is done, we

can compute the coefficients of degree $r+1$ of $h(x)$ using equation(3.9). Let us focus on $f(x, v(x))$, the same ideas apply for $g(x, v(x))$.

We recall that $f(x,y) = \sum_{n\geq 2} F_n(x,y)$, where the $F_n(x,y)$ are homogeneous polynomials of degree n. From lemma 3.1.1 we have that $F_n(x, v(x))$ is a polynomial that starts at degree n, hence, if we want the coefficients of $f(x, v(x))$ of degree $r+1$, we just need to find, $F_2(x, v(x)), \ldots, F_{r+1}(x, v(x))$. Here is where the recurrent expressions for F_j play an important role.

For the sake of simplicity, let us assume that $F_2(x,y)$ and $F_3(x,y)$ are known, and that

$$F_n(x,y) = R_1(F_{n-1}(x,y), F_{n-2}(x,y)), \qquad \text{for } n > 3,$$

where R_1 are basic arithmetic operation between polynomials. We use this expression to find the polynomials, $F_2(x, v(x)), \ldots, F_{r+1}(x, v(x))$ and then add them up to have $f(x, v(x))$ up to degree $r+1$.

Once we have $f(x, v(x))$ and $g(x, v(x))$ up to degree $r+1$, we easily compute $h(x)$ up to degree $r+1$ using equation (3.9) and operating with the full polynomials.

This process will be repeated up to the desired final degree N. At each step we need to run this recurrent scheme up to the desired degree. For some particular recurrences one can take advantage of its properties to save computational time. Notice that for each degree r we are recomputing the terms of degree $s < r$ that we already have.

In Appendix A we show how to expand the RTBPS equations in a recurrent way. We have used the Legendre polynomial recurrences to find such expressions. Nevertheless, there are other ways of expanding the equations in a recurrent way, one can considered, for instance, automatic differentiation tools [Knu81, Har08].

3.1.3 Results

We have applied these algorithms to the collinear points SL_1 and SL_2, taking $\beta = 0.051689$. This value of β corresponds to a solar sail with loading parameter of $30g/m^2$, and is considered to be realistic for a short term mission application, as the Geostorm Mission. We recall that SL_1 and SL_2 are the displaced collinear points when the sail is perpendicular to the Sun - line direction (see Appendix B).

We have computed the reduction to the centre manifold, finding $y = \widehat{v}(x)$ up to degree $N = 32$. In Tables 3.1 and 3.2 we can find the first terms of the expansion around SL_1 and SL_2 respectively.

To have an approximate idea of the radius of convergence of these series, we have

computed numerically the values,

$$r_{i,n} = \sqrt[n]{||v_n^i||_1}, \quad \text{where} \quad ||v_n^i||_1 = \sum_{|k|=n} |v_k^i|, \quad \text{for } 3 \leq n \leq N,\ i = 1, 2, \tag{3.10}$$

where the v_k^i are the coefficients of the monomials of exponent x^k. In Figure 3.1 we can see how these values behave for SL_1 (left) and SL_2 (right). They give an idea of the radius of convergence of the series, we can appreciate that the divergence is very mild. We can see that the radius of convergence around SL_2 is larger than for SL_1, but in both cases, for $N = 32$, we have a big neighbourhood where $\widehat{v}(x)$ gives a good approximation of the centre manifold.

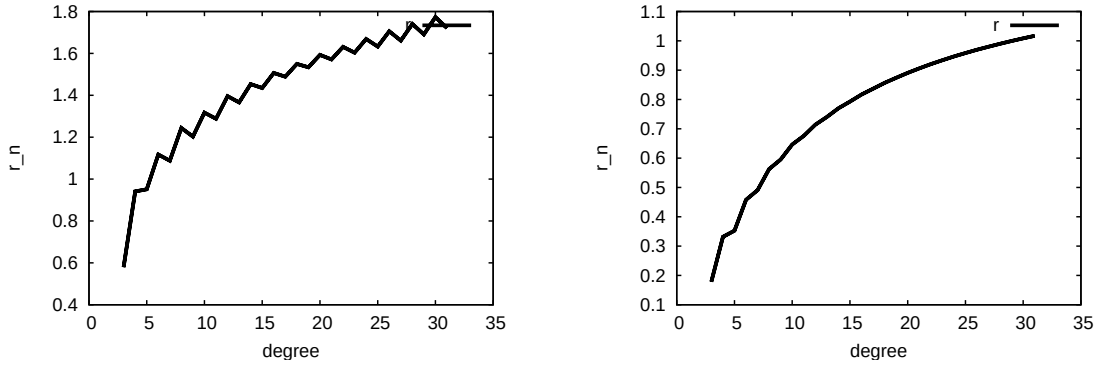

Figure 3.1: *In both pictures, the horizontal axis corresponds to the value of n and the vertical axis the values of $r_{i,n}$ (note that due to the symmetries $r_{1,n} = r_{2,n}$). From left to right: SL_1 and SL_2.*

3.2 A Lie Series Approach

Let H be a real analytic Hamiltonian of 3 degrees of freedom, that has an equilibrium point of the type centre $\times$ centre $\times$ saddle. Without loss of generality we can assume that the fixed point is at the origin. We start by expanding H as a power series around the origin,

$$H(q, p) = H_2(q, p) + H_3(q, p) + H_4(q, p) + \cdots, \tag{3.11}$$

where $H_j(q, p)$ are homogeneous polynomials of degree j in the variables (q, p) (q corresponds to the position and p to the momentum).

To save computational effort, we perform the changes of variables on the Hamiltonian (one equation) instead of doing it to the whole set of equations. To do this, we need the

k_1	k_2	k_3	k_4	v_1	v_2
2	0	0	0	3.5503156002936700e-02	-3.5503156002936700e-02
1	1	0	0	1.7843417171635231e-02	1.7843417171635231e-02
0	2	0	0	-2.6573244051375060e-03	2.6573244051375060e-03
0	0	2	0	3.8147437616048621e-02	-3.8147437616048621e-02
0	0	1	1	2.3407017142791586e-02	2.3407017142791586e-02
0	0	0	2	2.8553303366754226e-02	-2.8553303366754226e-02
3	0	0	0	5.4460164162132164e-03	5.4460164162132164e-03
2	1	0	0	5.6846959570042113e-02	-5.6846959570042113e-02
1	2	0	0	2.0967349558704437e-02	2.0967349558704437e-02
0	3	0	0	1.0668187765301932e-02	-1.0668187765301932e-02
1	0	2	0	7.8717031446172217e-03	7.8717031446172217e-03
0	1	2	0	4.3276556790009330e-02	-4.3276556790009330e-02
1	0	1	1	2.2839087896562357e-02	-2.2839087896562357e-02
0	1	1	1	5.0473597730196974e-02	5.0473597730196974e-02
1	0	0	2	-2.0822825309227966e-02	-2.0822825309227966e-02
0	1	0	2	2.0724575602143303e-02	-2.0724575602143303e-02

Table 3.1: *Coefficients of the series $y = v(x)$ truncated at degree 3 at SL_1 for $\beta = 0.051689$. The exponents (k_1, k_2, k_3, k_4) refer to the variables (x_1, x_2, x_3, x_4).*

k_1	k_2	k_3	k_4	v_1	v_2
2	0	0	0	-1.7506883374566809e-02	1.7506883374566816e-02
1	1	0	0	-1.2343035113662425e-02	-1.2343035113662429e-02
0	2	0	0	-7.2504422613208584e-03	7.2504422613208618e-03
0	0	2	0	-7.3684573354681898e-03	7.3684573354681907e-03
0	0	1	1	-5.2066907353733706e-03	-5.2066907353733715e-03
0	0	0	2	-3.8210740887108276e-03	3.8210740887108284e-03
3	0	0	0	9.3579427535247063e-04	9.3579427535247226e-04
2	1	0	0	7.3357172296303003e-03	-7.3357172296303046e-03
1	2	0	0	3.9348506952868612e-03	3.9348506952868630e-03
0	3	0	0	-9.2663856231447583e-04	9.2663856231447615e-04
1	0	2	0	3.9174272108506583e-04	3.9174272108506638e-04
0	1	2	0	1.9200159376202099e-03	-1.9200159376202108e-03
1	0	1	1	1.1589233890467723e-03	-1.1589233890467725e-03
0	1	1	1	1.8215774769214797e-03	1.8215774769214806e-03
1	0	0	2	-1.0501465169187070e-04	-1.0501465169187056e-04
0	1	0	2	-4.7627117583130449e-04	4.7627117583130439e-04

Table 3.2: *Coefficients of the series $y = v(x)$ truncated at degree 3 at SL_2 for $\beta = 0.051689$. The exponents (k_1, k_2, k_3, k_4) refer to the variables (x_1, x_2, x_3, x_4).*

changes of variables to be canonical as we need to preserve the Hamiltonian form.

In [GJMS01, Jor99, JM99] this procedure is applied to the RTBP around the collinear points $L_{1,2,3}$, and [Rol07] shows how to implement these algorithms using parallel computation. For this problem we have adapted the public software in [Jor] to our model. Let us

explain the main ideas of this algorithm, for further details on the algorithm see [Jor99].

3.2.1 Canonical transformations

Let $H(p,q)$ be a Hamiltonian function, and let us consider a change of variables $(p,q) = \Psi(x,y)$. Notice that the Hamilton equation obtained from $H \circ \Psi$ can be different from the ones obtained by applying directly the transformation Ψ to the Hamilton equation related to H. When these ones coincide we say that the transformation preserves the Hamiltonian form.

A change of variables is called *canonical* when it preserves the Hamilton form for any Hamiltonian function. It is known that a transformation is canonical if and only if the differential of the change of variables ($D\Psi$) is symplectic on any point.

To produce canonical transformations is not an easy task, since we need to impose the differential to be a symplectic matrix. Nevertheless, there are several techniques to produce such transformations. Here we use one that is based on several properties of Hamiltonian flows:

1. Let $\Phi_t(x,y)$ be the time t flow of a Hamiltonian system, then $(p,q) = \Phi_t(x,y)$ is a canonical transformation.

2. Let $G(q,p)$ be a Hamiltonian system, and let $(q_0(t), p_0(t))$ be a solution of G. Then

$$\frac{d}{dt} f(q_0(t), p_0(t)) = \{f, G\}(q_0(t), p_0(t)), \tag{3.12}$$

   for any smooth function f. Where $\{f, G\}$ is the Poisson bracket between the two functions f and G. We remind that the Poisson bracket between the functions $f(q,p)$, $g(q,p)$ is defined as:

$$\{f,g\} \;=\; \nabla f^T J \nabla g \;=\; \frac{\partial f}{\partial q}\frac{\partial g}{\partial p} - \frac{\partial f}{\partial p}\frac{\partial g}{\partial q}.$$

From these two affirmations one can see that: if H is a Hamiltonian and $G(q,p)$ is the time 1 flow of a Hamiltonian, the result of applying this transformation on H is,

$$\widehat{H} = H + \{H,G\} + \frac{1}{2!}\{\{H,G\},G\} + \frac{1}{3!}\{\{\{H,G\},G\},G\} + \cdots . \tag{3.13}$$

G is usually called the generating function of the transformation (3.13).

3.2.2 Scheme of the computation

Let us assume that we have already expanded the Hamiltonian around the origin as in equation (3.11). In order to simplify the following steps, it is convenient to have $H_2(p,q)$ in a canonical form.

Let A be the linearisation of the Hamiltonian flow around the origin ($A = J\nabla H_2(0,0)$). Let $\pm\lambda$, $\pm \mathrm{i}\,\omega_1$, $\pm \mathrm{i}\,\omega_2$ be the eigenvalues of A. We reduce A to its canonical form $\widetilde{A} = C^{-1}AC$, where C is a real matrix and $\widetilde{A} = diag(A_1, A_2, A_3)$ with,

$$A_1 = \begin{pmatrix} -\lambda & 0 \\ 0 & \lambda \end{pmatrix}, \qquad A_2 = \begin{pmatrix} 0 & \omega_1 \\ -\omega_1 & 0 \end{pmatrix}, \qquad A_3 = \begin{pmatrix} 0 & \omega_2 \\ -\omega_2 & 0 \end{pmatrix}.$$

It is not difficult to check that this change can be taken canonical by introducing some scaling. If we call (x,y) the new set of coordinates, x for the positions and y for the momenta, H_2 takes the form,

$$H_2(x,y) = \lambda x_1 y_1 + \frac{\omega_1}{2}(x_2^2 + y_2^2) + \frac{\omega_2}{2}(x_3^2 + y_3^2). \tag{3.14}$$

In order to simplify the computations during the centre manifold calculation (mainly, the computation of the generating functions) we perform a symplectic linear change of variables that takes the system to its diagonal form. Notice that x_1, y_1 are already in their diagonal form, so we just need to change the other 4 variables. Taking,

$$\begin{aligned} x_1 &= q_1, & x_2 &= \frac{q_2 + \mathrm{i}\,p_2}{\sqrt{2}}, & x_3 &= \frac{q_3 + \mathrm{i}\,p_3}{\sqrt{2}}, \\ y_1 &= p_1, & y_2 &= \frac{p_2 + \mathrm{i}\,q_2}{\sqrt{2}}, & y_3 &= \frac{p_3 + \mathrm{i}\,q_3}{\sqrt{2}}, \end{aligned} \tag{3.15}$$

H_2 now writes as,

$$H_2(p,q) = \lambda p_1 q_1 + \mathrm{i}\,\omega_1 p_2 q_2 + \mathrm{i}\,\omega_2 p_3 q_3. \tag{3.16}$$

Notice that the linear hyperbolic character is given by the couple (p_1, q_1) while the other variables define the centre behaviour. In order to decouple the hyperbolic direction from the elliptic one up to high order, we do not need to kill all the possible monomials, just the ones such that the exponent of p_1 is different from the one of q_1. There are other killing criteria that can be considered, (see [GJMS01, JL]), but this one also allows us to end up having a first integral.

Now we can start the reduction to the centre manifold. The main idea is to perform a sequence of transformations like (3.13) in order to kill degree by degree the desired

monomials of H. To see how this is done, let us show how to arrange degree three.

Let us select as a generating function $G_3(q,p)$, a homogeneous polynomial of degree three. The result of transforming H by the time 1 flow of G_3,

$$\widehat{H} = H + \{H, G_3\} + \frac{1}{2!}\{\{H, G_3\}, G_3\} + \cdots .$$

It is not difficult to see that if P and Q are two homogeneous polynomials of degree r and s respectively, then $\{P, Q\}$ is also a homogeneous polynomial of degree $r + s - 2$. Hence, the terms of $\widehat{H}$ satisfy

degree 2: $\widehat{H}_2 = H_2$,

degree 3: $\widehat{H}_3 = H_3 + \{H_2, G_3\}$,

degree 4: $\widehat{H}_4 = H_4 + \{H_3, G_3\} + \frac{1}{2!}\{\{H_2, G_3\}, G_3\}$,

$\vdots$

Therefore, to kill the desired monomials of degree 3 one has to look for a G_3 such that $\{H_2, G_3\} + H_3$ has these monomials equal to zero. The terms G_3 and H_3 can be expressed as,

$$G_3(q,p) = \sum_{|k_q|+|k_p|=3} g_{k_q,k_p} q^{k_q} p^{k_p}, \qquad H_3(q,p) = \sum_{|k_q|+|k_p|=3} h_{k_q,k_p} q^{k_q} p^{k_p}.$$

If we take $\eta_1 = \lambda$, $\eta_2 = \mathrm{i}\,\omega_1$ and $\eta_3 = \mathrm{i}\,\omega_2$, then $H_2(q,p) = \sum_{i=1}^{3} \eta_i q_i p_i$. As,

$$\{H_2, G_3\} = \sum_{|k_p|+|k_q|=3} \langle k_p - k_q, \eta\rangle g_{k_q,k_p} q^{k_q} p^{k_p}, \quad \eta = (\eta_1, \eta_2, \eta_3),$$

it is immediate to obtain that,

$$G_3(q,p) = \sum_{|k_q|+|k_p|=3} \frac{-h_{k_q,k_p}}{\langle k_p - k_q, \eta\rangle} q^{k_q} p^{k_p},$$

that is well defined because the condition $|k_p| + |k_q| = 3$ implies that $\langle k_p - k_q, \eta\rangle \neq 0$.

As we have already said, we do not want to kill all the monomials of degree three, just the ones where the exponents on p_1 and q_1 are different. So for the coefficients that we

do not want to kill we take the coefficient $g_{k_p,k_q} = 0$. Having,

$$G_3(q,p) = \sum_{(k_p,k_q)\in S_3} \frac{-h_{k_q,k_p}}{\langle k_p - k_q, \eta\rangle} q^{k_q} p^{k_p},$$

where S_n, $n \geq 3$ is the set of indexes (k_p, k_q) such that $|k_p| + |k_q| = n$ and have the first component of k_p different from the first component of k_q.

We end up having,

$$\widehat{H}(q,p) = H_2(q,p) + \widehat{H}_3(q,p) + \widehat{H}_4(q,p) + \cdots,$$

where $\widehat{H}_3(q,p)$ has the prescribed form. Now we proceed in an iterative way, killing the monomials $q^{k_q}p^{k_p}$ with $(k_q,k_p) \in S_n$, for $n = 4, 5, \ldots$. This process is carried up to sufficiently high order N. Hence, the transformed Hamiltonian $\widehat{H}(q,p)$ for $n = 3, \ldots, N$ has all its monomials in the desired form.

We must mention that as $\lambda \in \mathbb{R} \setminus \{0\}$, if $(k_p,k_q) \in S_n$ then $|\langle k_q - k_p, \nu\rangle| \geq 1|\lambda|$. This also assures us that we do not have small divisors in G_n.

After all the transformations the Hamiltonian takes the form,

$$\widehat{H} = H^{(N)}(q_1p_1, q_2, p_2, q_3, p_3) + R(q_1, p_1, q_2, p_2, q_3, p_3),$$

where $H^{(N)}$ is the part of the Hamiltonian that we have arranged and R denotes the remainder. If we neglect the remainder and take $q_1p_1 = 0$, we are skipping the hyperbolic part of $H^{(N)}$. The resulting Hamiltonian represents the flow inside an approximation of the centre manifold. So near the origin the phase space of the original Hamiltonian must be the phase space of $H^{(N)}(0, q_2, p_2, q_3, p_3)$ times a hyperbolic direction. To visualise the phase space on the centre manifold, one can fix the value of the Hamiltonian and then use a suitable Poincaré section.

It is important to notice the absence of small divisors in all the process. The divergence of this process is very mild (for a discussion of this process see [JL]), this makes the remainder to be small in a sufficiently large neighbourhood of the equilibrium point when this process is stopped for a certain N.

We recall that to have H_2 in a diagonal form we entered the complex phase space. So once we have finished the reduction process we need to apply the inverse change of variables given by equation (3.15) to the modified Hamiltonian $H^{(N)}$ to have this one in the real phase space. Notice that this is not necessary to do numerical integrations

and understand the dynamics, but it is useful, as the operations using real arithmetic are faster than using a complex arithmetic.

3.2.3 Results

We have adapted the public domain library in [Jor] to the RTBPS for a perpendicular Solar Sail, and considered $\beta = 0.051689$ as in Section 3.1.3.

We have computed the expansion of the Hamiltonian restricted to the centre manifold up to degree $N = 32$ at the collinear equilibrium points SL_1 and SL_2 respectively. In Tables 3.3 and 3.4 we can find the first terms of these expansions.

To have an idea of the radius of convergence of the series we have computed numerically the values,

$$r_n = \sqrt[n]{||H_n||_1}, \quad \text{where} \quad ||H_n||_1 = \sum_{|k|=n} |h_k|, \quad \text{for } 3 \leq n \leq N, \tag{3.17}$$

where the h_k are the coefficients of the monomials of exponent x^k. In Figure 3.2 we can see these values for SL_1 (left) and SL_2 (right). They give an idea of the radius of convergence of the series, we can appreciate that the divergence is very mild. Notice that for SL_2 the radius of convergence is larger than for SL_1, but in both cases for $N = 32$ we have a big neighbourhood where the modified $\widehat{H}$ gives a good approximation of the dynamics.

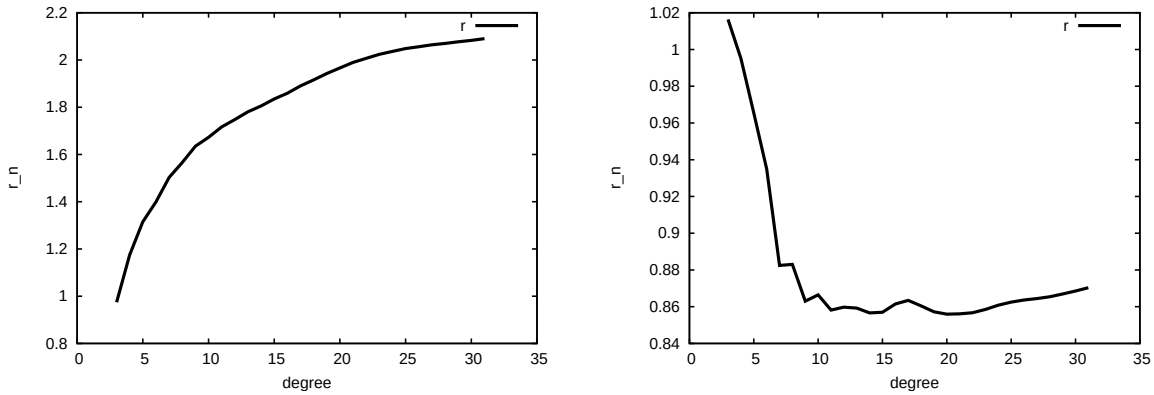

Figure 3.2: *In both pictures, the horizontal axis corresponds to the value of n and the vertical axis the values of r_n. From left to right: SL_1 and SL_2.*

k_1	k_2	k_3	k_4	h_k	k_1	k_2	k_3	k_4	h_k
2	0	0	0	6.2265667517669143e-01	0	0	2	2	2.5079559432629472e-02
0	2	0	0	6.2265667517669143e-01	4	1	0	0	-9.5850794092866431e-01
0	0	2	0	5.8841603727373581e-01	2	3	0	0	8.9664076808524873e-01
0	0	0	2	5.8841603727373581e-01	0	5	0	0	-2.4981368648887291e-02
2	1	0	0	5.6396639629808476e-01	2	1	2	0	-7.9713058687831795e-01
0	3	0	0	-8.2384619895258443e-02	0	3	2	0	2.9651411265486743e-01
0	1	2	0	2.7889905508879165e-01	3	0	1	1	-1.4808514924214936e-01
4	0	0	0	-2.7269463441025565e-01	1	2	1	1	1.9692859885303951e-01
2	2	0	0	7.5895544668314852e-01	2	1	0	2	2.0424400532712889e-01
0	4	0	0	-4.8826949550717223e-02	0	3	0	2	-3.5255336989995716e-02
2	0	2	0	-2.7377958223456894e-01	0	1	4	0	-1.5996695825115495e-01
0	2	2	0	3.2741624078653092e-01	1	0	3	1	-7.4332299532813700e-02
1	1	1	1	5.7170659054552292e-02	0	1	2	2	1.1973274094713404e-01
2	0	0	2	5.0713792305465924e-02	1	0	1	3	1.3709284563953436e-02
0	2	0	2	-2.2224922601547636e-02	0	1	0	4	-8.0914094767427763e-03
0	0	4	0	-6.8702044013507921e-02					

Table 3.3: *Coefficients up to degree* 5, *of the Hamiltonian restricted to the centre manifold at* SL_1 *for* $\beta = 0.051689$. *The exponents* (k_1, k_2, k_3, k_4) *refer to the variables* (q_2, p_2, q_3, p_3).

k_1	k_2	k_3	k_4	h_k	k_1	k_2	k_3	k_4	h_k
2	0	0	0	1.7322989883542399e+00	0	0	2	2	1.6866624170049516e-01
0	2	0	0	1.7322989883542399e+00	4	1	0	0	6.0646742774657904e-02
0	0	2	0	1.7090415995033998e+00	2	3	0	0	-1.4911538654097725e-01
0	0	0	2	1.7090415995033998e+00	0	5	0	0	1.3665081880113589e-02
2	1	0	0	-5.3481429234647238e-01	2	1	2	0	5.5825772462267019e-02
0	3	0	0	1.2941667603118245e-02	0	3	2	0	-6.9102572140442006e-02
0	1	2	0	-5.0214927846709145e-01	3	0	1	1	5.3708550049071303e-02
4	0	0	0	-2.4049000215462642e-02	1	2	1	1	-1.1553805534006134e-01
2	2	0	0	2.6749334664134067e-01	2	1	0	2	-9.5244592428503097e-02
0	4	0	0	-1.2415552501629217e-02	0	3	0	2	2.8431961390884643e-02
2	0	2	0	-4.3825787410913676e-02	0	1	4	0	-8.8476587697261728e-04
0	2	2	0	2.2438948116603341e-01	1	0	3	1	5.0249628386339631e-02
1	1	1	1	2.6832801596053099e-02	0	1	2	2	-1.0765378366189296e-01
2	0	0	2	1.7963804901434496e-01	1	0	1	3	-2.4034222457073172e-02
0	2	0	2	-1.3040877660634168e-02	0	1	0	4	1.4721820971207975e-02
0	0	4	0	-1.9948009163984572e-02					

Table 3.4: *Coefficients up to degree* 5, *of the Hamiltonian restricted to the centre manifold at* SL_2 *for* $\beta = 0.051689$. *The exponents* (k_1, k_2, k_3, k_4) *refer to the variables* (q_2, p_2, q_3, p_3).

3.3 Tests and Comparisons

First, we have done some checks on our programs, then we have compared the efficiency of both algorithms in terms of computational time.

Let us take an initial condition u_0 on the centre manifold and let u_1 be the result of integrating u_0 on the centre manifold up to time t_1. We send these points through the change of variables to the complete system. Let v_0 and v_1 be these points. Now we take

v_0 and integrate it up to time t_1 on the full system, let us call this point w_1.

Ideally, if the centre manifold, the change of variables and the numerical integrations were all exact, the difference between w_1 and v_1 would be zero. As we know, this will not be true due to the several sources of errors.

Let us define $h_0 = ||u_0||$, and compute $||v_1 - w_1||_2$. This quantity is affected by the truncation order of the reduction to the centre manifold process, the truncation error of the integrating method and the roundoff error due to the operations. We can choose the integration time t_1 and the distance to the origin h_0, in a way that $||v_1 - w_1||_2$ is mainly affected by the truncation order of the centre manifold. Then this quantity should behave as $\xi h_0^{(N+1)}$ where N is the last order that we have taken into account in the centre manifold. We can take two different initial conditions, $u_0^{(1)}$ and $u_0^{(2)}$, and estimate N by,

$$N + 1 \approx \frac{\log\left(\frac{er_1}{er_2}\right)}{\log\left(\frac{h_0^{(1)}}{h_0^{(2)}}\right)}, \tag{3.18}$$

where $er_i = ||v_1^{(i)} - w_1^{(i)}||$ and $h^{(i)} = ||u_0^{(i)}||$ for $i = 1, 2$.

We have taken the centre manifold around SL_1 and SL_2 computed in Section 3.1.3 using the Graph Transform method and used it to integrate on the centre manifold. We have taken an initial condition on the centre manifold $u_0 = (h_0, h_0, h_0, h_0)$ and computed v_1 and w_1 for $t_1 = 0.01$. In Table 3.5 we can see the local error of the numerical integration truncating the series at degree 8. It illustrates the good approximation of the dynamics on the centre manifold that this gives. In Table 3.6 we see the estimates of the truncation error.

We have done the same taking the transformed Hamiltonian around SL_1 and SL_2 computed using the Lie Series method explained in Section 3.2.3. In Table 3.7 we can see the local error of the numerical integration taking the truncated Hamiltonian up to degree 8 and in Table 3.8 we see the estimates of the truncation error using equation (3.18). Notice that we truncate the Hamiltonian up to degree 8, hence the estimation of the truncation error will be 8 as the set of equations that we are integrating are taken up to degree 7.

As we have already mentioned, the graph transform method is a more general approach, as it does not use any assumption on the set of equations, while the Lie series method can only be applied to Hamiltonian systems.

In Table 3.9 we see the CPU time needed to compute the reduction to the centre

h_0	$\|\|v_1 - w_1\|\|$
0.02	1.2139221824443741e-17
0.04	2.3643249923959272e-15
0.08	1.2618898774811476e-12
0.16	6.9534006796827247e-10
0.32	3.9879163406944996e-07

h_0	$\|\|v_1 - w_1\|\|$
0.02	2.5146775308808859e-17
0.04	1.8662949690767610e-16
0.08	9.6561350589145246e-14
0.16	4.8655084457371298e-11
0.32	2.4673928463137270e-08

Table 3.5: *For the graph transform method: difference between the numerical integration on the centre manifold and on the RTBPS taking initial conditions at a distance h_0 from the origin. Taking the series $y = v(x)$ truncated at degree 8 at SL_1 (left) and at SL_2 (right) for $\beta = 0.051689$.*

$h_0^{(1)}$	$h_0^{(2)}$	$N+1$
0.02	0.04	4.44043
0.04	0.08	9.02389
0.08	0.16	9.10595
0.16	0.32	9.16370

$h_0^{(1)}$	$h_0^{(2)}$	$N+1$
0.02	0.04	2.629343
0.04	0.08	8.764844
0.08	0.16	8.976466
0.16	0.32	8.986181

Table 3.6: *For the graph transform method: estimations of the truncation order for $\widehat{v}(x)$. For $\beta = 0.051689$ at SL_1 (left) and at SL_2 (right).*

manifold up to degree $N = 8, 16, 24, 32$, using the two different approaches. There, we can see that the graph transform algorithm is more efficient, in terms of computational time, than the Lie series approach. For instance, if we compute the centre manifold up to degree 32, it takes around $14min$ of CPU time to complete the whole process using the graph transform, and around $33min$ using the the Lie series approach. All the computations have been done on the same computer, with an Intel(R) Core(TM)2 Quad CPU at 2.83GHz.

Notice, that with the Lie series approach, we take the Hamiltonian equation, expand it around the fixed point, and by means of canonical transformation decouple up to high order the hyperbolic directions from the elliptic ones. Hence, during the whole process we deal with homogeneous polynomials with 6 variables and at the end of the process we set two of the variables to zero, to end on a 4D phase space.

On the other hand, with the graph transform method, we compute the power expansion of the local centre manifold ($y = v(x)$). We see that $v(x)$ must satisfy an invariant equation, that we solve equalising degree by degree. Now, during the whole process we deal with homogeneous polynomials with 4 variables, which coincides with the dimension of the final phase space. Under general conditions, the cost of operating with polynomials of 4 variables is much less than the cost of operating with polynomials of 6 variables.

Although it is less efficient, the Lie series approach is convenient when we have a

h_0	$\|\|v_1 - w_1\|\|$
0.02	3.6920450235560199e-15
0.04	9.4549612587473395e-13
0.08	2.4173024466492310e-10
0.16	6.4090169252390676e-08
0.32	2.1474173035560701e-05

h_0	$\|\|v_1 - w_1\|\|$
0.02	3.9057253333709475e-15
0.04	1.8756915513177915e-14
0.08	9.7024896946065764e-13
0.16	2.2668434557013075e-10
0.32	5.4714331083417134e-08

Table 3.7: *For the Lie series method: difference between the numerical integration on the centre manifold and on the RTBPS taking initial conditions at a distance h_0 from the origin. Taking the series H_N truncated at degree 8 at SL_1 (left) and at SL_2 (right) for $\beta = 0.051689$.*

$h_0^{(1)}$	$h_0^{(2)}$	N
0.02	0.04	8.001
0.04	0.08	7.998
0.08	0.16	8.051
0.16	0.32	8.388

$h_0^{(1)}$	$h_0^{(2)}$	N
0.02	0.04	2.263
0.04	0.08	5.692
0.08	0.16	7.868
0.16	0.32	7.915

Table 3.8: *For the Lie series method: estimations of the truncation order for the reduction to the centre manifold for H_8. For $\beta = 0.051689$ at SL_1 (left) and at SL_2 (right).*

N	Lie Series	Graph Transform
8	0m 0.085s	0m 0.057s
16	0m 3.876s	0m 2.943s
24	2m 10.251s	1m 13.965s
32	33m 22.000s	14m 35.475s

Table 3.9: *Computational time for Lie Series* vs *the Graph Transform method to compute the reduction to the centre manifold up to degree N.*

Hamiltonian system, as we end up with a very good approximation of the Hamilton equation on the centre manifold, and we preserve most of the interesting properties of the system. The Hamilton equation will be very useful to study the phase space, we use this first integral to reduce the phase space dimension (see Section 4.3).

3.4 Conclusions

Our aim has been to develop a tool to understand the non - linear dynamics close to unstable equilibrium point. Moreover, we are interested in a general procedure that can be applied to a non Hamiltonian systems. To this end, we use the *graph transform method*. The idea is to compute, formally, the power expansion of the graph of the local centre manifold ($y = v(x)$). In Section 3.1 we have described the main details of this algorithm

and discuss some tricks that can be implemented to reduce the computational effort.

We have compared this method with a more classical approach to this problem. If the system is Hamiltonian one can use a Lie series method, taking advantage of the Hamiltonian structure of the system. In Section 3.2 we summarise the main ideas of this method. We have taken the public software in [Jor], that deals with the reduction to the centre manifold around a collinear equilibrium point for the RTBP, and adapted it to our model.

In Section 3.3 we have seen that the graph transform method is more efficient in terms of computational time than the Lie series method. Moreover, this method gives a more general approach to the problem and will be very useful to study the non - linear dynamics around the equilibrium points when the sail is not orientated perpendicular to the Sun - line, as we will see in the next chapter.

Chapter 4

Periodic and Quasi - Periodic motion around equilibria

In this Chapter we describe the periodic and quasi - periodic motions around some of these equilibrium points, and show how the phase space portrait varies when the sail orientation changes. In the near future we want to use this information, to derive strategies in the philosophy of Chapter 2 for the station keeping of a solar sail close to these invariant objects.

From now on, we always consider the sail orientation to be fixed along time, and study what is the dynamics for several fixed sail orientations. We show how the dynamics varies for different sail orientations close to perpendicular. We study the particular case of $\alpha = 0$, and δ close to 0.

In Section 4.1 we describe some of the properties of the system when we set $\alpha = 0$. Here the system is time reversible, and has 5 families of equilibrium parametrised by δ. We will see that for three of these families, the local behaviour around an equilibrium point is as a Hamiltonian system.

In Section 4.2 we describe the families of periodic orbits that emanate from an equilibrium point for different sail orientations (δ). Finally, in Section 4.3 we have performed the reduction of the centre manifold around different equilibrium points up to degree 16, using the graph transform algorithm explained in the previous Chapter. In both sections we start by analysing what happens when the sail is perpendicular to the Sun - line and then see how the pattern varies when it is no longer perpendicular.

4.1 Particular Case

From now on, we focus on the particular case of a perfectly reflecting solar sail, when one of the two angles, α, is zero. In this way, we only allow the sail orientation to vary vertically with respect to the Sun - line.

When $\alpha = 0$, the normal direction to the sail, $\vec{n}$, is simplified:

$$\vec{n} = \left[\frac{X-\mu}{r_{ps}} \cos\delta - \frac{Z(X-\mu)}{r_{ps} r_2} \sin\delta \ , \ \frac{Y}{r_{ps}} \cos\delta - \frac{YZ}{r_{ps} r_2} \sin\delta \ , \ \frac{Z}{r_{ps}} \cos\delta + \frac{r_2}{r_{ps}} \sin\delta \right],$$

and the projected sail area $\langle \vec{r}_s, \vec{n} \rangle = \cos\delta$ is constant in time. The equations of motion can be expressed as,

$$\begin{aligned} \ddot{X} - 2\dot{Y} &= \frac{\partial \widetilde{\Omega}}{\partial X} - \beta \frac{(1-\mu)}{r_{PS}^3} \frac{(X-\mu)Z}{r_2} \cos^2\delta \sin\delta, \\ \ddot{Y} + 2\dot{X} &= \frac{\partial \widetilde{\Omega}}{\partial Y} - \beta \frac{(1-\mu)}{r_{PS}^3} \frac{YZ}{r_2} \cos^2\delta \sin\delta, \\ \ddot{Z} &= \frac{\partial \widetilde{\Omega}}{\partial Z} + \beta \frac{(1-\mu)}{r_{PS}^3} r_2 \cos^2\delta \sin\delta, \end{aligned} \tag{4.1}$$

where,

$$\widetilde{\Omega}(X,Y,Z) = \frac{1}{2}\left(X^2+Y^2\right) + \frac{(1-\mu)(1-\beta\cos^3\delta)}{r_{PS}} + \frac{\mu}{r_{PE}}.$$

In Chapter 1 we mentioned that the RTBPS has zero divergence. In addition, for $\alpha = 0$ the system is also time reversible by:

$$R : (X, Y, Z, \dot{X}, \dot{Y}, \dot{Z}) \to (X, -Y, Z, -\dot{X}, \dot{Y}, -\dot{Z}),$$

for all fixed δ. We recall, that for the particular cases $\delta = 0$ and $\delta = \pm\pi/2$ it is also Hamiltonian. (These cases correspond to a the sail perpendicular to the Sun - line direction ($\delta = 0$) or to neglect the sail's effect by aligning it to the Sun - line ($\delta = \pm\pi/2$)).

For $\alpha = 0$ the system has 5 families of equilibria parametrised by the angle δ. Each of families contains one of the classical Lagrangian equilibrium points L_i and its related displaced equilibrium point SL_i, we call each of these families FL_i for $i = 1, \ldots, 5$. In Figures 4.1 and 4.2 we can see these families for different values of β. Notice that as β increases these families get "larger", having fixed points higher above the ecliptic plane and closer to the Sun.

In Figure 4.1 we have the families FL_1 (left), FL_2 (centre) and FL_3 (right), all of them are on the $Y = 0$ plane. All of these equilibrium points are unstable, for small values of β, the spectrum of the equilibrium point is $\{\pm\lambda, \pm i\,\omega_1, \pm i\,\omega_2\}$. In Figure 4.3 we show the spectrum of the fixed points for $\beta = 0.051689$. For large β this changes, and for some of the equilibrium points, the spectrum is $\{\pm\lambda_1, \pm\lambda_2, \pm i\,\omega_1\}$ [WM07, WM08].

In Figure 4.2 we have the family FL_4, which no longer lies on the $Y = 0$ plane. The FL_5 family is symmetric to FL_4 with respect to $Y = 0$. The spectrum for all these points is $\{\gamma_1 \pm i\,\omega_1, \gamma_2 \pm i\,\omega_2, \gamma_3 \pm i\,\omega_3\}$, where $\gamma_i \neq 0$ with $\gamma_1 > 0, \gamma_2 < 0$ and γ_3 positive on FL_4 and negative on FL_5. In Figure 4.4 we see the spectrum for $\beta = 0.051689$ for FL_4 and FL_5. Notice that although $\gamma_i \neq 0$, it is very small. Hence, they present a very mild instability, we can think of fixed points that are practically stable.

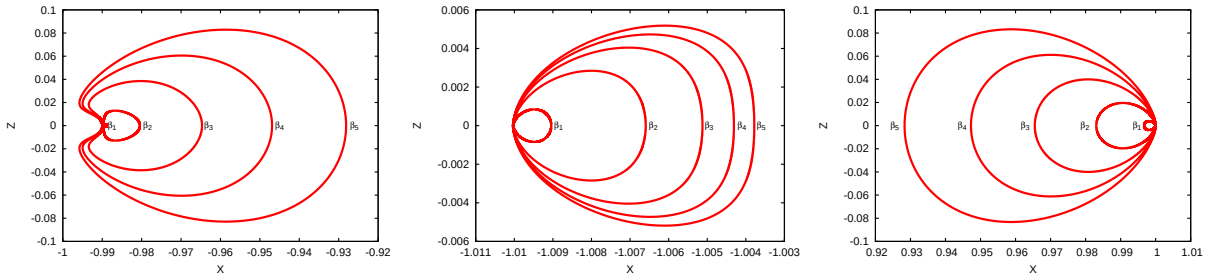

Figure 4.1: *Families of equilibrium points for* $\beta_1 = 0.01$, $\beta_2 = 0.05$, $\beta_3 = 0.1$, $\beta_4 = 0.15$ *and* $\beta_5 = 0.2$. *From left to right:* FL_1, FL_2 *and* FL_3 *families of equilibria.*

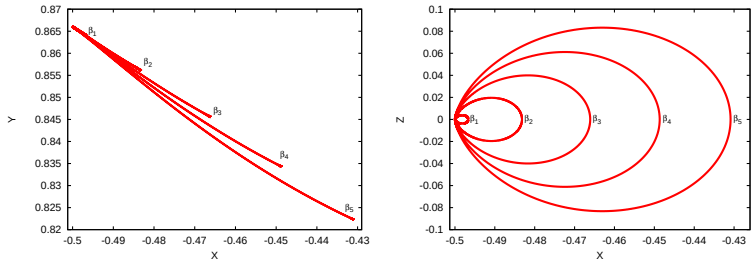

Figure 4.2: FL_4 *family of equilibrium points for* $\beta_1 = 0.01$, $\beta_2 = 0.05$, $\beta_3 = 0.1$, $\beta_4 = 0.15$ *and* $\beta_5 = 0.2$. *From left to right:* XY *projection and* XZ *projection.*

Our aim is to describe the natural dynamics around different unstable equilibrium of these families. We focus on the FL_1 family, which we consider a more relevant region for possible mission applications. Although, the same techniques presented here can be used to understand the motion around the $FL_{2,3}$ families. We will show how the dynamics varies for different sail orientations close to $\delta = 0$.

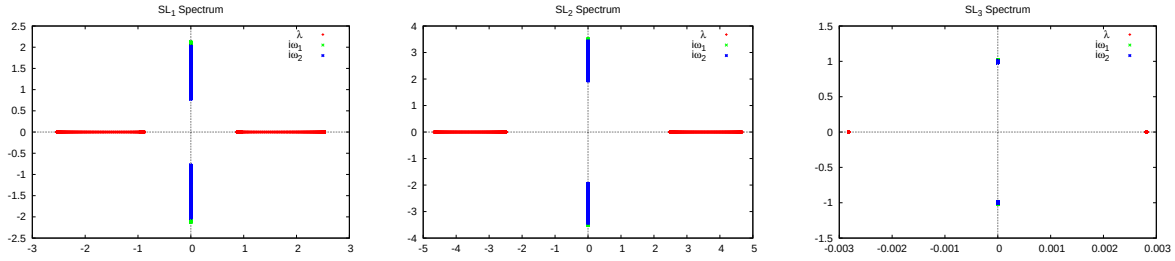

Figure 4.3: *Spectrum of the equilibrium points on the FL_1, FL_2 and FL_3 families for $\beta =$ 0.051689.*

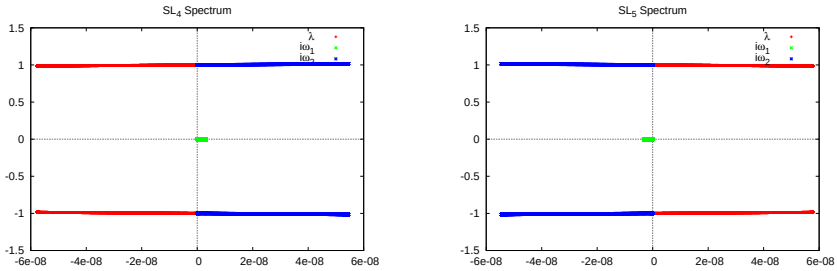

Figure 4.4: *Spectrum of the equilibrium points on the FL_4 and FL_5 families for $\beta = 0.051689$.*

In Section 4.2 we describe the families of periodic orbits around an equilibrium point and in Section 4.3, using the reduction to the centre manifold we describe the bounded motion around equilibria.

4.1.1 Linearisation around equilibria

The equilibrium points on the FL_1 family for a given $\delta \in [-\pi/2, \pi/2]$ are of the type $p_0 = (X^*, 0, Z^*)$, with $\mu - 1 < X^* < 0$. The linearised system around an equilibrium point is given by $\dot{\Phi} = M\Phi$, where $M = Df(p_0)$ is of the form,

$$M = \left(\begin{array}{c|c} 0 & Id \\ \hline A & B \end{array}\right), \quad A = \begin{pmatrix} a_{xx} & 0 & a_{xz} \\ 0 & a_{yy} & 0 \\ a_{zx} & 0 & a_{zz} \end{pmatrix}, \quad B = \begin{pmatrix} 0 & 2 & 0 \\ -2 & 0 & 0 \\ 0 & 0 & 0 \end{pmatrix}.$$

It can be seen that if $\delta = -\pi/2, 0, \pi/2$, then $a_{xz} = a_{zx} = 0$. Hence the Z oscillation is decoupled from the planar motion. For the other values of δ, $a_{xz} \neq a_{zx}$, as $Z^* \neq 0$, so the vertical oscillation is not decoupled. As we will see further on, for $\delta = 0$, the periodic motion is equivalent to the periodic motion on the RTBP.

The characteristic polynomial of M is $p(\eta) = \eta^6 + C_1\eta^4 + C_2\eta^2 + C_3$. Calling $\nu = \eta^2$, one can see that $p(\nu)$ has always three real roots [WM07]. Depending on the values of β and δ, there will be two positive roots and one negative one, or one positive root and two negative ones. For $\beta = 0.051689$ we always have one positive and two negative roots ($\nu_1 > 0$ and $\nu_2, \nu_3 < 0$). Hence, if we define $\lambda = \sqrt{\nu_1}$ and $\omega_1 = \sqrt{-\nu_2}$, $\omega_2 = \sqrt{-\nu_3}$, then $\pm\lambda$, $\pm\mathrm{i}\,\omega_1$ and $\pm\mathrm{i}\,\omega_2$ are the eigenvalues. This shows that the linear dynamics around each equilibrium point is of the type centre $\times$ centre $\times$ saddle.

To find the eigenvectors we will take advantage of the form of the matrix $M_\eta = M - \eta I_6$. We denote by $(v_1^T, v_2^T)^T$ to the elements of the kernel of M_η. It is easy to check that they must satisfy $v_2 = \eta v_1$ and $Av_1 + (B - \eta Id)v_2 = 0$. Then we need to solve a 3×3 linear system. We will treat separately two cases $\delta = -\pi/2, 0, \pi/2$ and the rest of the possible values for δ.

It is known [Sze67] that for $\delta = -\pi/2, 0, \pi/2$, i.e. $a_{xz} = a_{zx} = 0$, the eigenvectors related to $\nu = \pm\lambda$ are,

$$\begin{aligned}
\vec{v}_{+\lambda} &= [\ 2\lambda\ ,\ \lambda^2 - a_{xx}\ ,\ 0\ ,\ 2\lambda^2\ ,\quad \lambda(\lambda^2 - a_{xx})\ ,\ 0\ ]^T, \\
\vec{v}_{-\lambda} &= [-2\lambda\ ,\ \lambda^2 - a_{xx}\ ,\ 0\ ,\ 2\lambda^2\ ,\ -\lambda(\lambda^2 - a_{xx})\ ,\ 0\ ]^T.
\end{aligned}$$

The eigenvectors related to $\nu = \mathrm{i}\,\omega_1$ are $\vec{v}_{\omega_1} \pm i\vec{u}_{\omega_1}$ with,

$$\begin{aligned}
\vec{v}_{\omega_1} &= [\ 2\omega_1\ ,\ 0\ ,\ 0\ ,\ 0\ ,\ \omega_1(\omega_1^2 - a_{xx})\ ,\ 0\ ]^T, \\
\vec{u}_{\omega_1} &= [\ 0\ ,\ \omega_1^2 - a_{xx}\ ,\ 0\ ,\ 2\omega_1^2\ ,\ 0\ ,\ 0\ ]^T,
\end{aligned}$$

and the eigenvectors related to $\nu = \mathrm{i}\,\omega_2$ are $\vec{v}_{\omega_2} \pm i\vec{u}_{\omega_2}$ with,

$$\begin{aligned}
\vec{v}_{\omega_2} &= [\ 0\ ,\ 0\ ,\ 1\ ,\ 0\ ,\ 0\ ,\ 0\ ]^T, \\
\vec{u}_{\omega_2} &= [\ 0\ ,\ 0\ ,\ 0\ ,\ 0\ ,\ 0\ ,\ \omega_2\ ]^T.
\end{aligned}$$

For the other values of δ it can be seen that the elements of the kernel of M_η are of the form

$$\begin{aligned}
\vec{v} = \ [\ &(a_{zz} - \eta^2)(a_{yy} - \eta^2),\ 2\eta(a_{zz} - \eta^2),\ -a_{zx}(a_{yy} - \eta^2), \\
&\eta(a_{zz} - \eta^2)(a_{yy} - \eta^2),\ 2\eta^2(a_{zz} - \eta^2), -a_{zx}\eta(a_{yy} - \eta^2)\ ]^T .
\end{aligned}$$

Then the eigenvectors related to $\eta = \pm\lambda$ are,

$$\begin{aligned}
\vec{v}_{+\lambda} &= [\ (a_{zz}-\lambda^2)(a_{yy}-\lambda^2)\ ,\ 2\lambda(a_{zz}-\lambda^2)\ ,\ -a_{zx}(a_{yy}-\lambda^2)\ , \\
&\qquad \lambda(a_{zz}-\lambda^2)(a_{yy}-\lambda^2)\ ,\ 2\lambda^2(a_{zz}-\lambda^2)\ ,\ -a_{zx}\lambda(a_{yy}-\lambda^2)\ ]^T, \\
\vec{v}_{-\lambda} &= [\ (a_{zz}-\lambda^2)(a_{yy}-\lambda^2)\ ,\ -2\lambda(a_{zz}-\lambda^2)\ ,\ -a_{zx}(a_{yy}-\lambda^2)\ , \\
&\qquad -\lambda(a_{zz}-\lambda^2)(a_{yy}-\lambda^2)\ ,\ 2\lambda^2(a_{zz}-\lambda^2)\ , -a_{zx}\lambda(a_{yy}-\lambda^2)\ ]^T.
\end{aligned}$$

We can do the same for $\eta = \pm\mathrm{i}\,\omega_1,\ \pm\mathrm{i}\,\omega_2$, having the expression $\vec{v}$ for the eigenvector. Separating real and imaginary parts as $\vec{u}_{\omega_i} + i\vec{v}_{\omega_i}$, we obtain,

$$\begin{aligned}
\vec{u}_{\omega_i} &= [\ (a_{zz}+\omega_i^2)(a_{yy}+\omega_i^2)\ ,\ 0,\ -a_{zx}(a_{yy}+\omega_i^2)\ ,\ 0\ ,\ -2\omega_i^2(a_{zz}+\omega_i^2)\ ,\ 0\ ]^T, \\
\vec{v}_{\omega_i} &= [\ 0\ ,\ 2\omega_i(a_{zz}+\omega_i^2)\ ,\ 0\ ,\ \omega_i(a_{zz}+\omega_i^2)(a_{yy}+\omega_i^2)\ ,\ 0\ ,\ -a_{zx}\omega_i(a_{yy}+\omega_i^2)\ ]^T,
\end{aligned}$$

for $i = 1, 2$. Now the $Z, \dot{Z}$ motion is no longer decoupled from the planar motion, due to the loss of symmetry when we change δ. But it can be seen, that for small δ's, one of the two oscillations has a larger Z oscillation than the other. For the sake of simplicity, from now on we assume this one to be ω_2.

Finally, the linearised motion around an equilibrium point p_0 is given by,

$$\begin{aligned}
\Phi(t) &= p_0 + A_0\,[\cos(\omega_1 t+\psi_1)\vec{v}_{\omega_1} + \sin(\omega_1 t+\psi_1)\vec{u}_{\omega_1}] \\
&\quad + B_0\,[\cos(\omega_2 t+\psi_2)\vec{v}_{\omega_2} + \sin(\omega_2 t+\psi_2)\vec{u}_{\omega_2}] \\
&\quad + C_0 e^{\lambda t}\vec{v}_{+\lambda} + D_0 e^{-\lambda t}\vec{v}_{-\lambda}.
\end{aligned} \tag{4.2}$$

We will use this linear approximation to find periodic orbits close to the equilibrium point, by setting $C_0 = D_0 = 0$, and $A_0 = 0$ or $B_0 = 0$, depending on which type of orbits we are more interested. These small orbits can the be used as initial guess for a continuation method to compute the whole family of periodic orbits, as we will see in Section 4.2.

4.2 Periodic Motion

It is well known that if we have a fixed point p_0 on a Hamiltonian system, with $\pm\mathrm{i}\,\omega$ as an eigenvalue, then under suitable non-resonance conditions with respect to the remaining eigenvalues λ_i, the Lyapunov Centre Theorem [MH91] ensures that there exist a one - parametric family of periodic orbits emanating from p_0, with limiting period $2\pi/\omega$.

Unfortunately, as we have already mentioned, the Hamiltonian character of the set of equations is only true for 3 values of δ.

In any case, in the previous section we saw that for $\alpha = 0$ the RTBPS is time R - reversible by

$$R : (t, X, Y, Z, \dot{X}, \dot{Y}, \dot{Z}) \rightarrow (-t, X, -Y, Z, -\dot{X}, \dot{Y}, -\dot{Z}).$$

It is known [Sev86, LR98], that under certain constraints a time reversible system behave locally as Hamiltonian systems around an equilibrium point. In particular, around this point the Lyapunov's Centre Theorem [Dev76, Mos58, Sev86, LR98] and KAM Theory [Sev98, LR98] also apply.

Theorem 4.2.1 *[Dev76] Let $\dot{x} = f(x)$, with $f \in \mathcal{C}^2$ and $x \in \mathbb{R}^{2n}$ be an autonomous R - reversible dynamical system, where $\dim(Fix(R)) = n$. Let p_0 be a fixed point such that $R(p_0) = p_0$, and with $\pm \mathrm{i}\,\omega,\ \pm\lambda_2, \ldots,\ \pm\lambda_n$ as eigenvalues.*

Then, if $\forall \lambda_i$ we have that $\mathrm{i}\,\omega/\lambda_i \notin \mathbb{Z}$, there exists a one-parametric family of periodic orbits emanating from p_0, where the period of these orbits tends to $2\pi/\omega$ when approaching p_0.

This Theorem is commonly known as Devaney - Lyapunov's Centre Theorem, for further details and its proof see [Dev76, Sev86].

One can check that the only equilibrium points that remain fixed by R are the ones on the FL_1, FL_2 and FL_3 families. Hence, the local behaviour around these equilibria will be Hamiltonian. Theorem 4.2.1 [Dev76] assures that under non - resonant conditions between ω_1, ω_2 we have two families of periodic orbits emanating from the fixed point.

In this section we want to describe the two families of periodic orbits that appear around an equilibrium point of the FL_1 family. We distinguish the two families by their vertical oscillation. In Section 4.1.1 we already mentioned that, for small δ, one of the two eigendirections has a wider vertical oscillation than the other, and we assume this one to be ω_2. Then, we call the $\mathcal{P}$ - *Lyapunov Family* to the family of periodic orbits emanating from p_0 related to ω_1 and the $\mathcal{V}$ - *Lyapunov Family* to the family emanating from p_0 related to ω_2.

Due to the symmetric reversibility properties of the system, all these families of periodic orbits are symmetric with respect to $Y = 0$. Furthermore, for small δ, the $\mathcal{P}$ - Lyapunov Family cross transversally $Y = 0$ and the $\mathcal{V}$ - Lyapunov Family cross transversally $Z = Z^*$ just two times. From now on, we will only consider $\delta > 0$, as the systems is also symmetric by

$$S : (X, Y, Z, \dot{X}, \dot{Y}, \dot{Z}, \delta) \rightarrow (X, Y, -Z, \dot{X}, \dot{Y}, \dot{Z}, -\delta).$$

We start by taking $\delta = 0$, and study how the family of periodic orbits behave. Then, we see how these families vary for different sail orientations.

To compute the families of periodic orbits, we have designed our own routines for the numerical refinement and continuation of periodic orbits. For each of the families we have taken into account the transversality properties mentioned before. We have used a multiple shooting method [SB02] using two spatial sections, to avoid difficulties in the integration of the periodic orbits, as they are very unstable. For the $\mathcal{P}$ - Family we have taken the sections $\Gamma_1 = \{Y = 0, \dot{Y} > 0\}$ and $\Gamma_2 = \{Y = 0, \dot{Y} > 0\}$, and for the $\mathcal{V}$ - Family we have taken $\Sigma_1 = \{Z = Z^*, \dot{Z} > 0\}$ and $\Sigma_2 = \{Z = Z^*, \dot{Z} > 0\}$. As an initial guess for the continuation we can take the linear approximation of the solutions for the flow from equation (4.2). We must also mention that due to the symmetries on the equations, if we take the cross section Γ_1 and Γ_2 we can save time by just integrating half of the period.

We have also computed the stability of the periodic orbits on each family. It is well known that, if $\phi_t(x)$ is the flow associated to an ODE, the normal behaviour around a T - periodic orbit through x_0 is given by the monodromy matrix $M = D\phi_T(x_0)$. As we are in a reversible system, the eigenvalues come in pairs, so

$$spect(M) = \{1, 1, \lambda_1, \lambda_1^{-1}, \lambda_2, \lambda_2^{-1}\}.$$

We define the *stability parameters* of the periodic orbit as $s_i = \lambda_i + \lambda_i^{-1}$ for $i = 1, 2$. These parameters will help us to describe the stability of the periodic orbit. The S_i can be of the kind:

- *Hyperbolic*: if $s_i \in \mathbb{R}$ with $|s_i| > 2$. It is equivalent to $\lambda_i \in \mathbb{R} \setminus \{-1, 1\}$.
- *Elliptic*: if $s_i \in \mathbb{R}$ with $|s_i| < 2$. It is equivalent to $\lambda_i = e^{\mathrm{i}\rho}$ with $\rho \in \mathbb{R}$.
- *Parabolic*: if $s_i \in \mathbb{R}$ with $|s_i| = 2$. It is equivalent to $\lambda_i = \pm 1$.
- *Complex unstable*: if $\lambda_i \in \mathbb{C} \setminus \mathbb{R}$. It is equivalent to $\lambda_i \in \mathbb{C} \setminus \mathbb{R}$, $|\lambda_i| \neq 1$.

In what follows, we will say that the periodic orbit has an hyperbolic direction if $|s_i| > 2$, and we say it has an elliptic direction if $|s_i| < 2$. Notice that if s_1 is complex unstable, then s_2 is also complex unstable, in fact $s_2 = \overline{s_1}$.

4.2.1 $\mathcal{P}$ - Family of periodic orbits

We have taken the linear approximation given by equation (4.2) as an initial guess, and we have considered the X coordinate of the point where the orbit crosses Γ_1 as the parameter

of continuation.

Let us start by taking $\delta = 0$, where the periodic orbits that are born close to the equilibrium point are totally contained on the $Z = 0$ plane. In Figure 4.5 we can see the continuation scheme, on the x - axis we have the continuation parameter (X) and on the y - axis the Z component of the point of the orbit on the section Γ_1. At a certain time, a pitchfork bifurcation takes place, and two new periodic orbits are born, commonly known as Halo orbits.

On the left - hand side of Figure 4.5 we can see this bifurcation, in red we have plotted those periodic orbits with one elliptic and an hyperbolic direction, and in blue those orbits with two hyperbolic directions. On the right - hand side of Figure 4.5 we have the evolution on the stability parameters along the family.

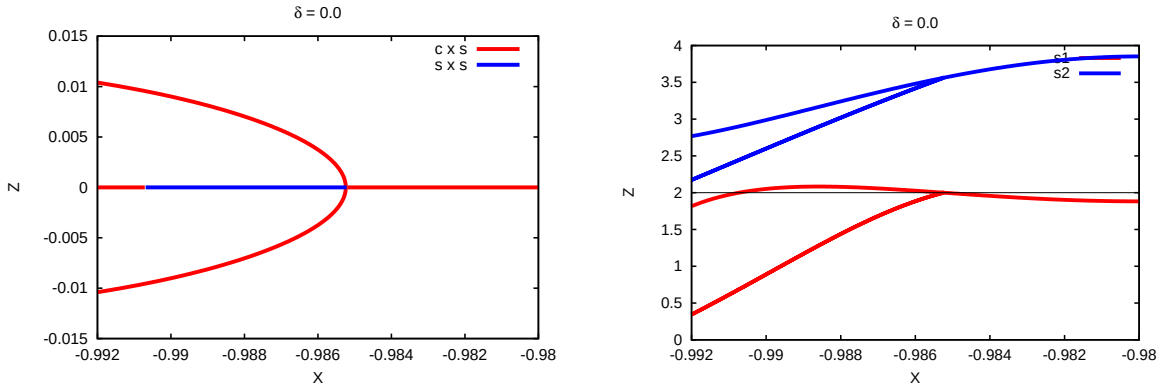

Figure 4.5: *$\mathcal{P}$ - family of periodic orbits for $\delta = 0$. Left: bifurcations diagram for the continuation of periodic orbits w.r.t. X, centre×saddle orbits in red, saddle×saddle orbits in blue. Right: evolution of the stability parameters s_1 and s_2 along the family of periodic orbits.*

On the left hand side of Figure 4.6 we see the planar periodic orbits on the $\mathcal{P}$ - Family, before and after the bifurcation point, and on the left hand side we see the evolution of the stability parameters along the family. In Figure 4.7 we see different projections of one of the two families of Halo orbits. The other family is symmetric to this one w.r.t. $Z = 0$. Finally, in Figure 4.8 we have two different 3D projections on the X, Y, Z space of the three branches of the periodic orbits on the family.

Now we consider $\delta \neq 0$, and again continue the $\mathcal{P}$ - Family of periodic orbits emanating from the equilibrium point. We see that there is no longer a pitchfork bifurcation as it happened for $\delta = 0$. Now, two of the branches split, leaving a family of periodic orbits with no change in the stability and another family with a saddle - node bifurcation, as can be seen in on the left hand side of Figure 4.9. This is due to what is known as symmetry

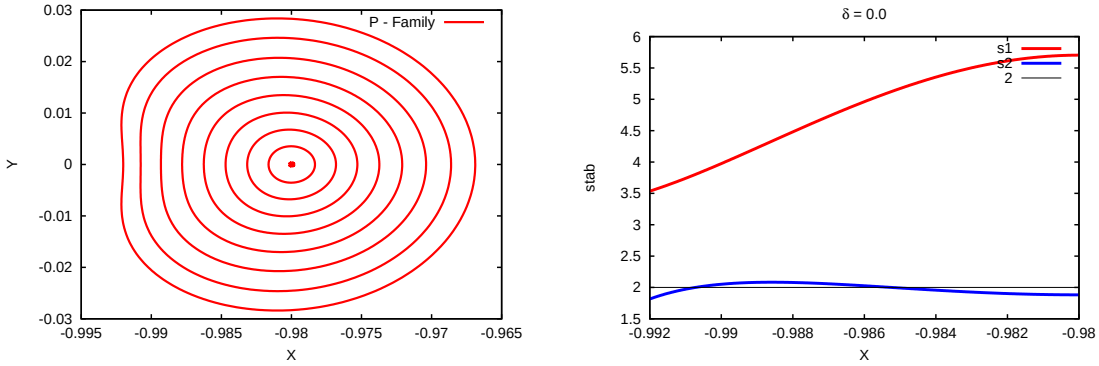

Figure 4.6: *XY projection on the Planar Lyapunov periodic orbits on the $\mathcal{P}$ - Family (left). Stability parameters of the planar family of periodic orbits (right).*

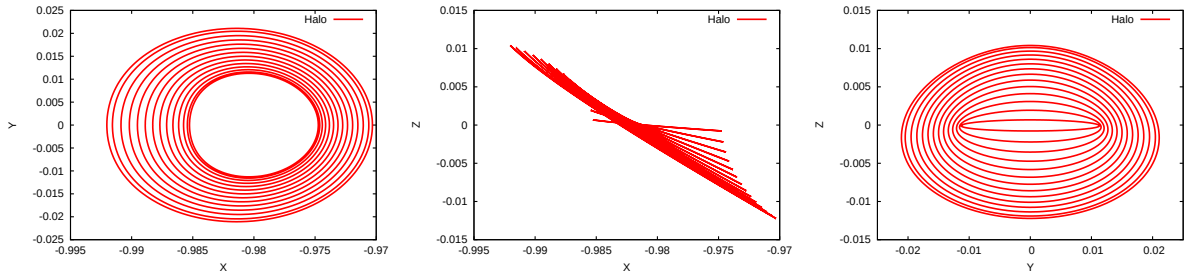

Figure 4.7: *Projections of Halo type orbits, that appear after the first bifurcation of the Planar Family of periodic orbits. From left to right: XY projection, XZ projection and YZ projection of the orbits.*

breaking [GSS85, Cra91]. It is well known that the pitchfork bifurcations are a degenerate type of bifurcations, that usually appear when the system has some symmetries, as it happens when $\delta = 0$. But for $\delta \neq 0$ this symmetry breaks, and a saddle - node bifurcation appears instead (the saddle - node bifurcations are more common, and do not require symmetries). On the right hand side of Figure 4.9, we can see the evolution of separation between the two branches as δ increases.

In Figures 4.10 and 4.11 we can see different projections of these two families for $\delta = 0.01$. In Figure 4.10 we have the family that emanates from the equilibrium point. We can see how, as the orbits amplitude increases they gain Z amplitude, ending up looking like Halo type orbits. Here all the periodic orbits have one hyperbolic and one elliptic direction. In Figure 4.10 we see the family of periodic orbits that appears after the saddle - node bifurcation. The orbits on the second component of the family that have less Z oscillation have two hyperbolic directions, while the other ones have one hyperbolic and one elliptic direction. Finally, in Figure 4.12 we have different 3D projections, on the

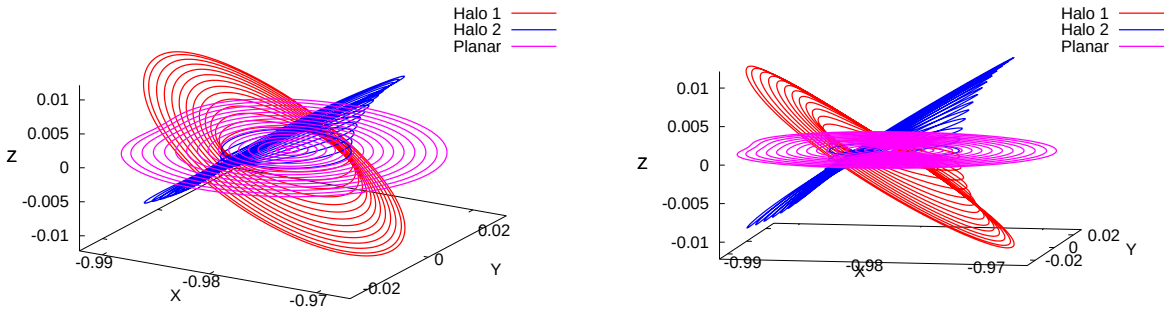

Figure 4.8: *Different projections on the XYZ space of the 3 different branches of periodic orbits for $\delta = 0$.*

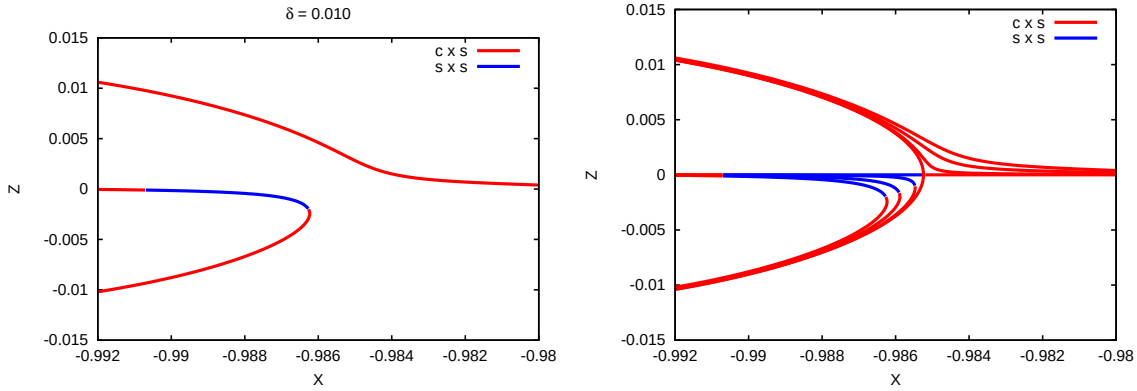

Figure 4.9: *Bifurcation diagram for the continuation of periodic orbits w.r.t. X of the $\mathcal{P}$ - Family of periodic orbits for different sail orientations (δ). For $\delta = 0.001$ (left). Evolution of the bifurcation diagram for $\delta = 0, 0.001, 0.005, 0.01$ (right).*

X, Y, Z space, of the two disconnected branches of the $\mathcal{P}$ - Family of periodic orbits for $\delta = 0.01$. We can see that qualitatively it does not differ that much from the particular case $\delta = 0$. We still have Halo - type orbits and planar motion.

4.2.2 $\mathcal{V}$ - Family of periodic orbits

Here we have also taken the linear approximation in equation (4.2) as initial guess, and we have considered the $\dot{Z}$ coordinate of the point where the orbit crosses Σ_1 as the parameter of continuation.

We start by taking $\delta = 0$, here the periodic orbits are symmetric with respect to the

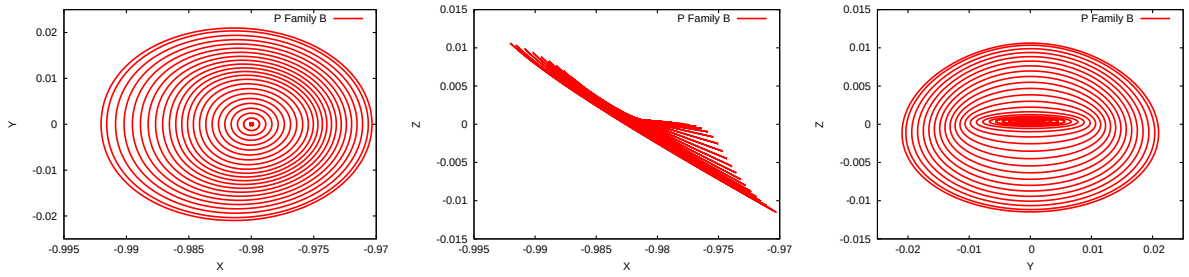

Figure 4.10: *For $\delta = 0.01$. Different projections of the periodic orbits on $\mathcal{P}$ - Family that emanate form the fixed pint. From left to right: XY projection, XZ projection and YZ projection.*

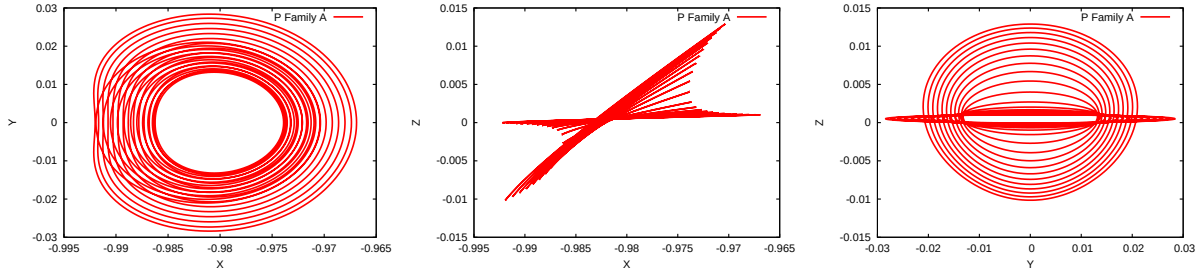

Figure 4.11: *For $\delta = 0.01$. Different projection of the periodic orbits on $\mathcal{P}$ - Family that appear after a saddle node bifurcation. From left to right: XY projection, XZ projection and YZ projection.*

planes $Z = 0$ and $Y = 0$. In Figure 4.13 we have different projections of this family of periodic orbits. We can see that these orbits have a bow tie shape. All them have one hyperbolic and one elliptic direction.

For $\delta \neq 0$ the family of periodic orbits is only symmetric with respect to the $Y = 0$ plane. The periodic orbits that are born near the equilibrium point are seen as circles on the XZ projection. As we move along the family, their shape changes and they again look like a bow tie, although it is no longer symmetric. For small δ, the shape of most of the orbits in the family still looks like a bow tie. We can see that as δ increases there is more difference between the two loops on the bow tie. In Figure 4.14 we have different projections of this family for $\delta = 0.01$. Again, all these periodic orbits have one hyperbolic and one elliptic direction. Finally, Figure 4.15 shows 3D projections, on the X, Y, Z space, of these families for different values of δ. We can see clearly, how these families get more asymmetric as δ increases. In the picture we have $\delta = 0, 0.005, 0.01$ and 0.03.

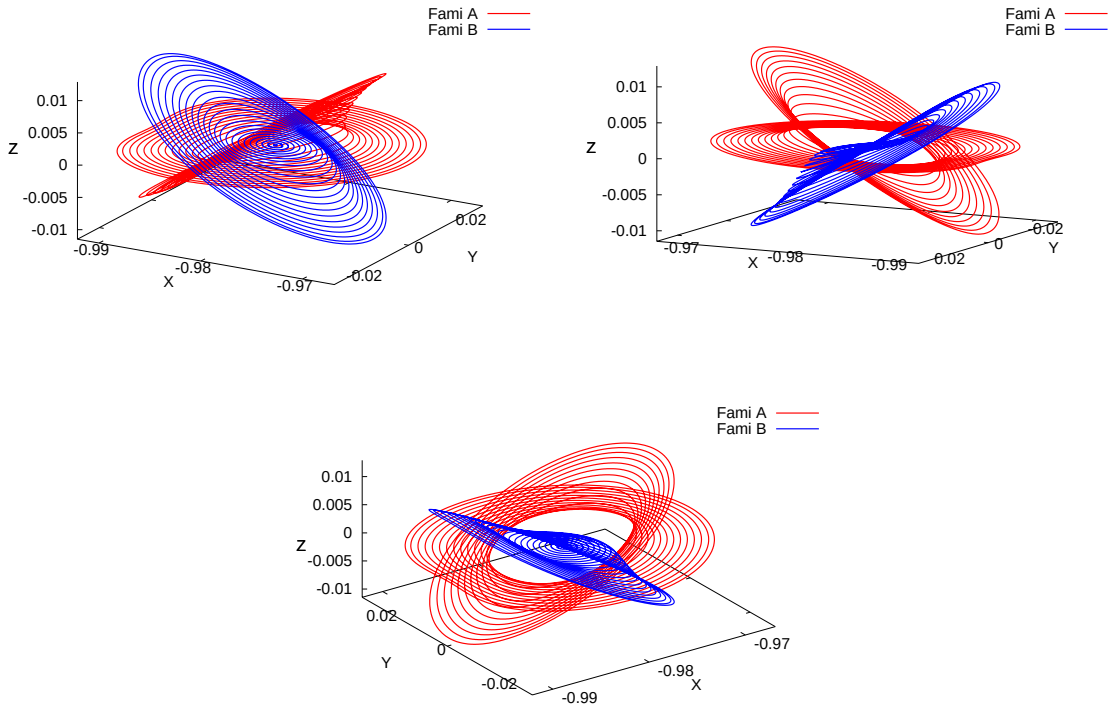

Figure 4.12: *Different projections on the XYZ space of the 2 disconnected branches of periodic orbits for $\delta = 0.01$.*

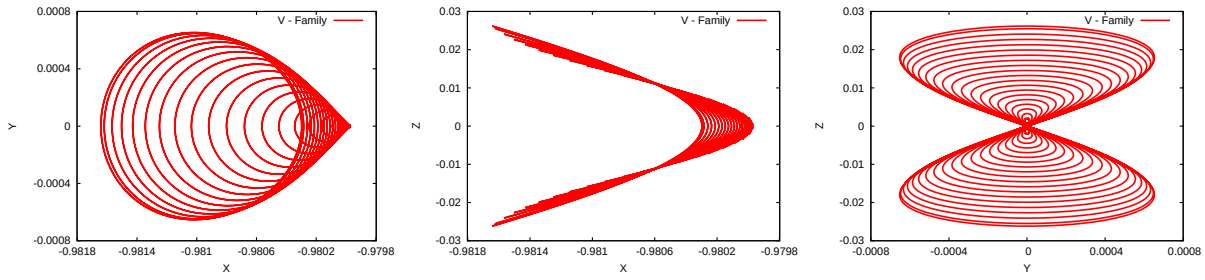

Figure 4.13: *For $\delta = 0$. Different projections of the periodic orbits on the $\mathcal{V}$ - family. From left to right: XY projection, XZ projection and YZ projection.*

4.3 Dynamics on the Centre Manifold

Using the algorithm explained in Chapter 3 we have computed the centre manifold around several equilibrium points of the FL_1 family, i.e different sail orientations. For each each fixed point we have computed the approximation $y = \widehat{v}(x)$ of the centre manifold up to degree 16. Here we want to describe the dynamics around an equilibrium point for

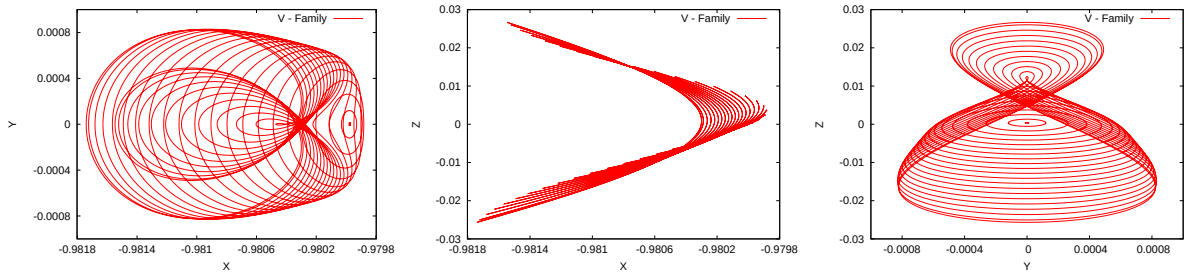

Figure 4.14: *For $\delta = 0.01$. Different projections of the periodic orbits on the $\mathcal{V}$ - family. From left to right: XY projection, XZ projection and YZ projection.*

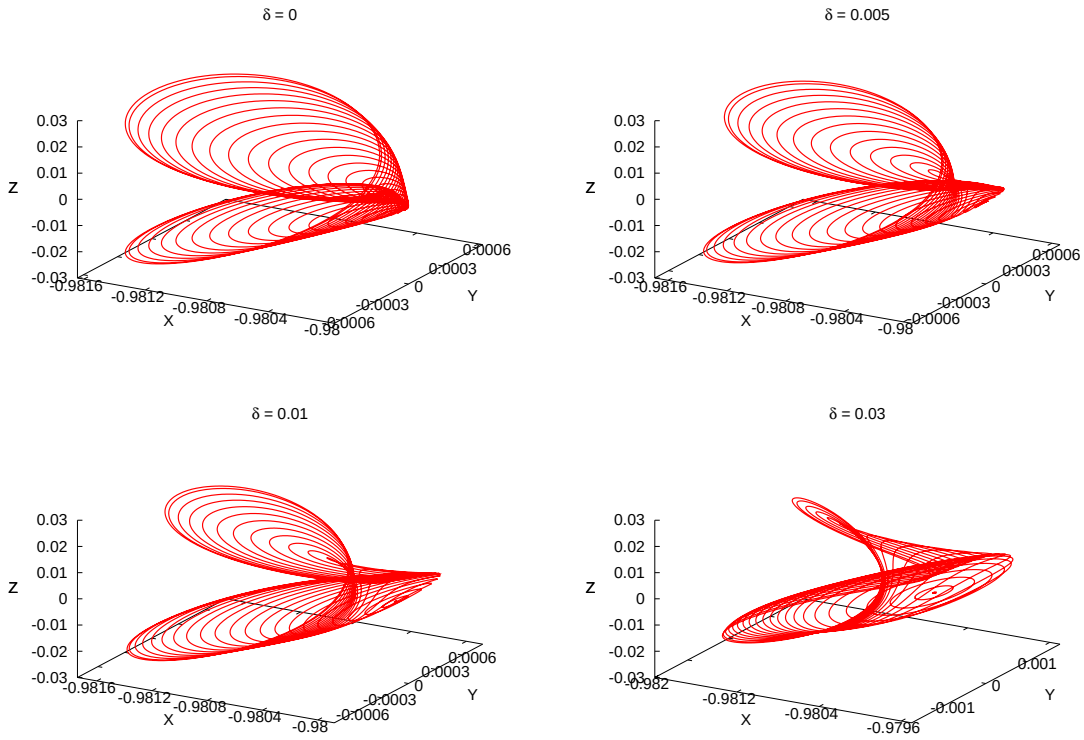

Figure 4.15: *Projections on the XYZ space of the $\mathcal{V}$ - Family of periodic orbits for different values of δ. From left to right, top to bottom: $\delta = 0, \delta = 0.005, \delta = 0.01$ and $\delta = 0.03$*

different values of δ.

We start by considering $\delta = 0$, where the system is Hamiltonian. We take advantage of this to visualise the phase space. Once we have described the non - linear dynamics for this particular case, we will discuss how the phase space varies when we change the sail orientation (δ).

Once we have reduced to the centre manifold, we are on a 4D phase space. Let (x_1, x_2, x_3, x_4) be the local coordinates on the centre manifold. A 4D phase space is difficult to visualise, so we need to perform suitable Poincaré sections to reduce the phase space dimension.

4.3.1 When the sail is perpendicular to the Sun - sail line

As we have mentioned several times, here the system is Hamiltonian. We take advantage of this to visualise the phase space. The Jacobi constant,

$$J_C = \dot{X}^2 + \dot{Y}^2 + \dot{Z}^2 - 2\Omega(X, Y, Z),$$

with $\Omega(X, Y, Z) = (X^2 + Y^2)/2 + (1 - \mu)(1 - \beta)/r_{PS} + \mu/r_{PE}$, is a first integral of the system. Hence, it remains constant along time for a given trajectory. We group the trajectories on the phase space by their energy level, i.e. the value of the Jacobi constant (J_C).

To visualise the dynamics on the centre manifold, we take the Poincaré section $x_3 = 0$ and fix J_C to determine x_4. Notice that taking $x_3 = 0$ is the same as taking $Z = 0$ and x_4 is related to $\dot{Z}$. Hence, x_1, x_2 are a linear transformation of the XY plane. For each energy level we take several initial conditions and compute 500 iterates of the Poincaré map. Figure 4.16 shows the results for $J_C = -2.895937, -2.895920, -2.895904$ and -2.895889. We can see that for a fixed energy level, the motion on the section is bounded by the planar Lyapunov orbit, which is fully contained on this section. The vertical Lyapunov orbit is the fixed point in the middle, as it crosses transversally this section close to the origin.

For small values of the energy, the coupling of the two frequencies, ω_1 and ω_2, give rise to a family of invariant tori. As the J_C varies, the planar Lyapunov orbit changes its stability and the Halo orbits appear (see Section 4.2.1). These orbits are the two new fixed points on the section, as the Halo orbits also cross transversally this section. We still see families of invariant tori around the fixed point and around the two Halo orbits.

Notice that $x_3 = 0$ is not the only Poincaré section that we can do. We have taken this one for classical reasons, and because we know that $Z = 0$ is a cross section and the motion is symmetric with respect to this plane. But we could choose another one, for instance $Y = 0$ is also a cross section and a symmetry plane.

So we take $x_2 = 0$ and determine x_1 from the J_C. We repeat the same process as before, for each J_C we take several initial conditions x_3, x_4 and compute 500 iterates of

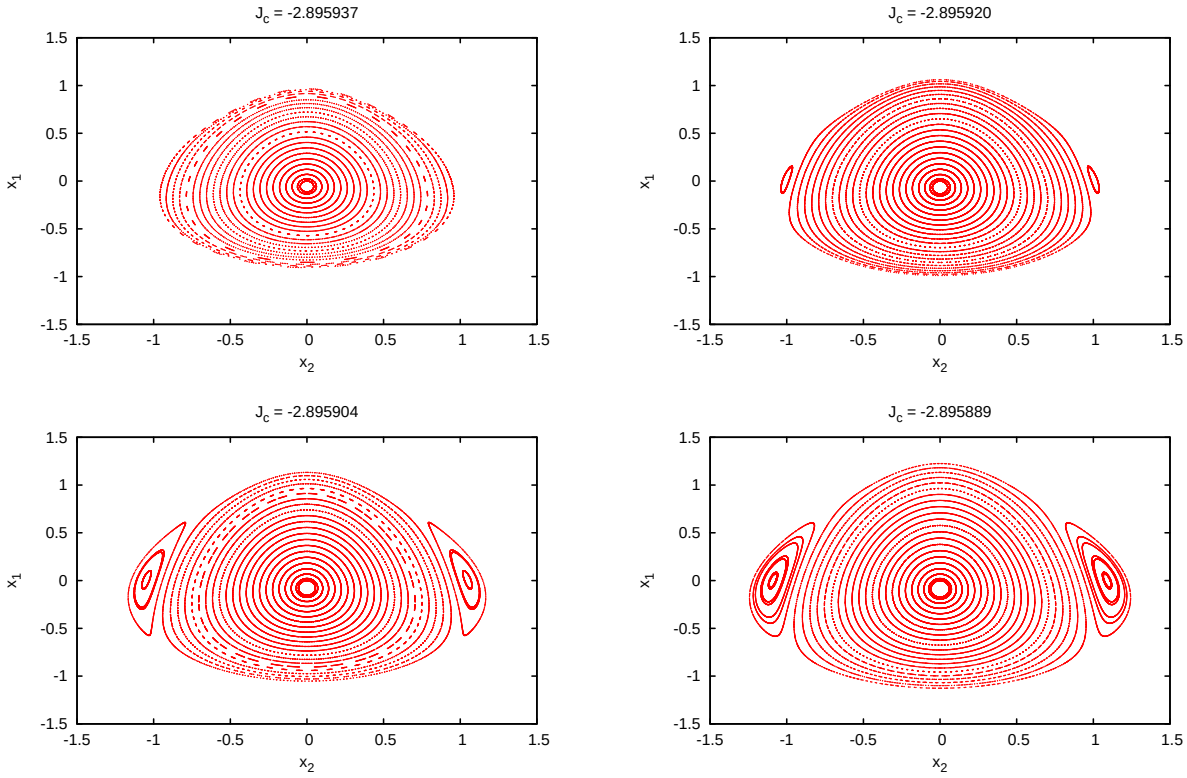

Figure 4.16: *For $\delta = 0$. Poincaré section for $x_3 = 0$ for different energy levels. From left to right, top to bottom: $J_C = -2.895937, -2.895920, -2.895904, -2.895889$.*

the Poincaré map. Figure 4.17 shows the results for the same energy levels as before.

Now the planar Lyapunov orbit is the central fixed point. As before, we can see that for small values of the energies, we have a family of invariant tori due to the coupling of the two frequencies. As the energy level increases the planar Lyapunov orbit changes its stability and the two Halo orbits appear. Here we can clearly appreciate the pitchfork bifurcation of the planar Lyapunov orbit that gives rise to the Halo orbits that was mentioned in Section 4.2.

We note that the behaviour here is qualitatively the same as for the RTBP close to the collinear points. Now we want to see how this is perturbed when the sail is no longer perpendicular to the Sun - line (i.e. $\delta \neq 0$).

4.3.2 When the sail is not perpendicular to the Sun - sail line.

Now we take different values for the sail orientation $\delta_1 = 0.005$ and $\delta_2 = 0.01$ and we perform the same analysis. The main difference is that now the system is not Hamilto-

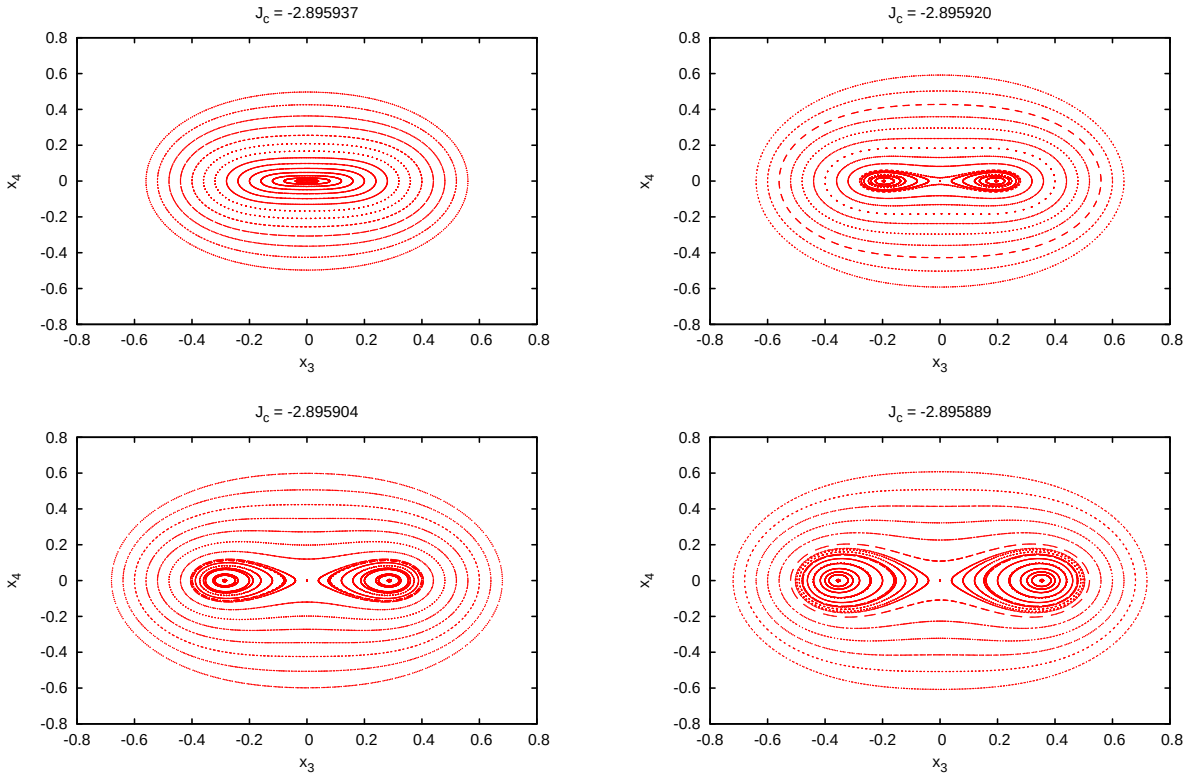

Figure 4.17: *For $\delta = 0$. Poincaré section for $x_2 = 0$ for different energy levels. From left to right, top to bottom: $J_C = -2.895937, -2.895920, -2.895904, -2.895889$.*

nian, hence we do not have a first integral to help us reduce the phase space dimension. Nevertheless, we use the quantity,

$$\widetilde{J}_C = \dot{X}^2 + \dot{Y}^2 + \dot{Z}^2 - 2\widetilde{\Omega}(X, Y, Z) + 2\beta(1-\mu)\frac{Zr_2}{r_{PS}^3}\cos^2\delta\sin^2\delta.$$

We recall that $\widetilde{\Omega}(X, Y, Z) = (X^2 + Y^2)/2 + (1-\mu)(1-\beta\cos^2\delta)/r_{PS} + \mu/r_{PE}$. Notice that for $\delta = 0$, $\widetilde{J}_C$ is the Jacobi constant used before. This value varies little along the trajectories, we observe variations of less than 10^{-8} in the cases that we have studied. We will use it as an "approximated energy level" and will allow us to classify the trajectories and compare the Hamiltonian behaviour with the non - Hamiltonian one.

When the system is Hamiltonian and we take several initial conditions with the same energy level, their trajectories are in the same surface of fixed energy. Hence, we are reducing in one the phase space dimension. When the system is not Hamiltonian and we take several initial conditions with the same $\widetilde{J}_C$, the "approximated energy level", this one does not remain fixed for all of the points on the trajectories. But close to the equilibrium

point, $\widetilde{J}_C$ has a small variation. The projection of the trajectories on a fixed surface of fixed $\widetilde{J}_C$ will be good enough to produce meaningful plots.

As for the Hamiltonian case, we first perform the Poincaré section $x_3 = 0$. This is like taking the cross section $Z = Z^*$. We use $\widetilde{J}_C$ to determine x_4, that is related to $\dot{Z}$. Now we take different initial conditions (x_1, x_2) and perform 500 iterates of the Poincaré map for different $\widetilde{J}_C$. Figures 4.18 and 4.19 show, for $\delta = 0.005$ and $\delta = 0.01$ respectively, these iterates on the Poincaré sections for $\widetilde{J}_C = -2.895937, -2.895920, -2.895904$ and -2.895889.

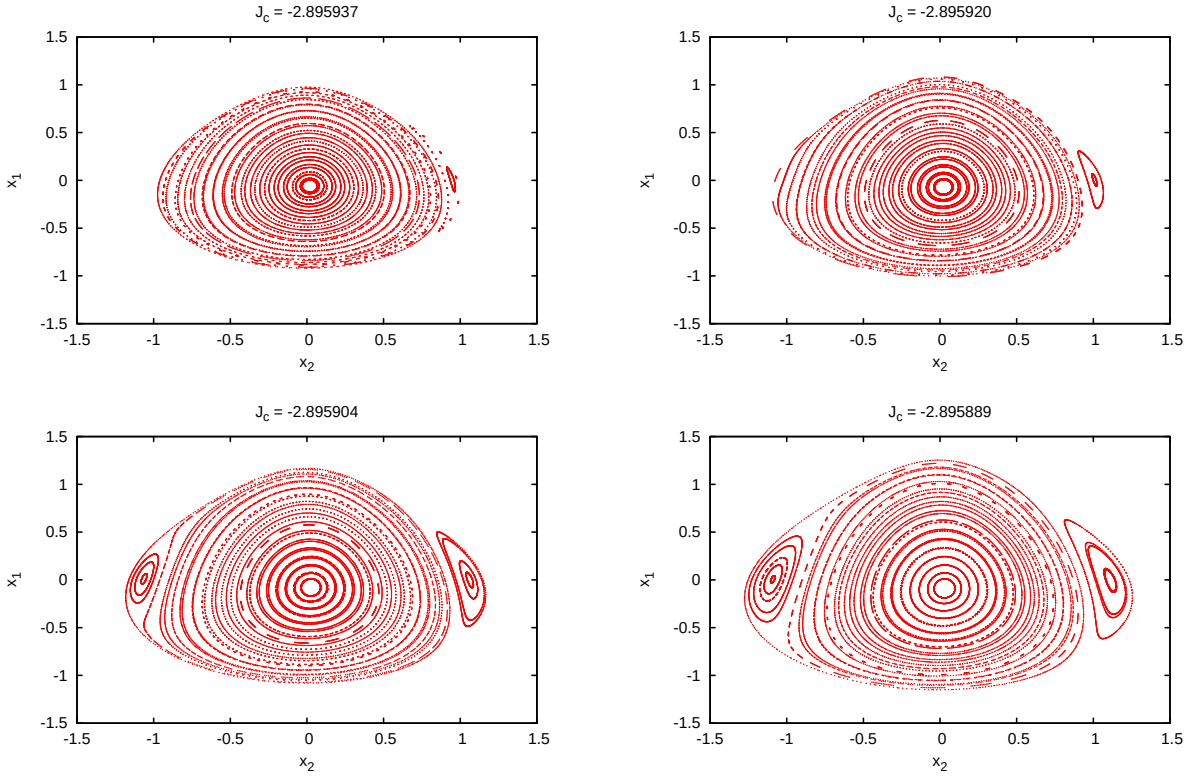

Figure 4.18: *For $\delta = 0.005$. Poincaré section for $x_3 = 0$ for different $\widetilde{J}_C$. From left to right, top to bottom: $\widetilde{J}_C = -2.895937, -2.895920, -2.895904, -2.895889$.*

As before, we see that for small energy levels the coupling between the two frequencies gives rise to families of invariant tori around the equilibrium point. The fixed points in the centre corresponds to an orbit of the $\mathcal{V}$ - Family that cross transversally this section, and an orbit of the $\mathcal{P}$ - Family is close to the boundary of the motion on the section. As $\widetilde{J}_C$ varies, one Halo-type orbit appears, seen as the new fixed point that appears on the right hand side of the Poincaré sections. We recall the behaviour of the $\mathcal{P}$ - Family of periodic orbits for $\delta \neq 0$ discussed in Section 4.2.1. This family starts with a small $\dot{Z}$ amplitude

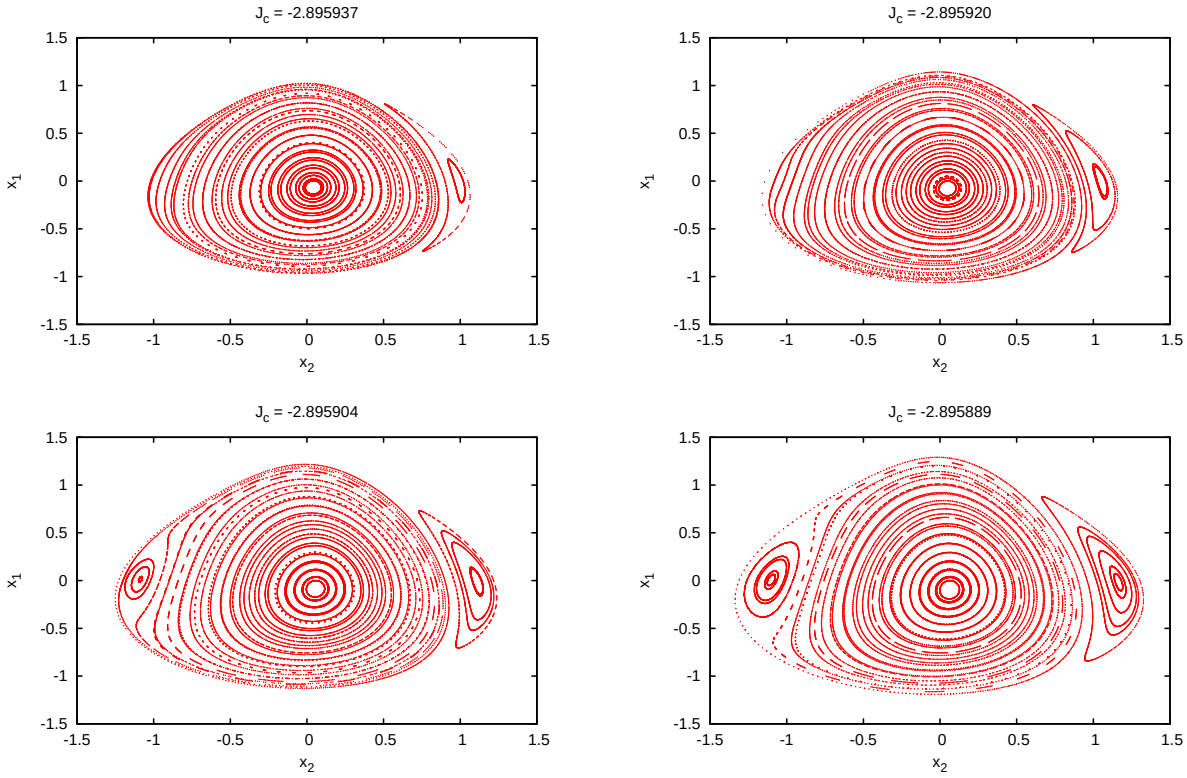

Figure 4.19: *For $\delta = 0.01$. Poincaré section for $x_3 = 0$ for different $\widetilde{J}_C$. From left to right, top to bottom:* $\widetilde{J}_C = -2.895937, -2.895920, -2.895904, -2.895889$.

and there is a point close to the saddle - node bifurcation where the $\dot{Z}$ amplitude starts to grow significantly, having Halo - type orbits. When the orbit gains Z amplitude, it is transversal to this Poincaré section, and we see it appear in the Poincaré section. When the saddle - node bifurcation takes place, another Halo - type orbit appears, as can be seen in Figure 4.18 and 4.19. We can see that the two Halo orbits are no longer symmetric to each other, as well as the behaviour around them.

Let us now take the Poincaré section $x_2 = 0$ and we fix $\widetilde{J}_C$ to determine x_1. As before we take several initial conditions (x_3, x_4) as perform 500 iterates on the Poincaré section for different $\widetilde{J}_C$. In Figures 4.20 and 4.21 show, for $\delta = 0.005$ and $\delta = 0.01$ respectively, the Poincaré section $x_2 = 0$ for different values for $\widetilde{J}_C$.

Now the fixed point in the centre corresponds to an orbit of the $\mathcal{P}$ - Family. For small values of $\widetilde{J}_C$ we just see the families of invariant tori around the fixed point, due to the coupling between the two elliptic frequencies. As this energy increases, we can see how the fixed point shifts to the left and two new periodic orbits appear, one stable and the other unstable, giving rise to the second family of Halo - type orbit. Here we can clearly

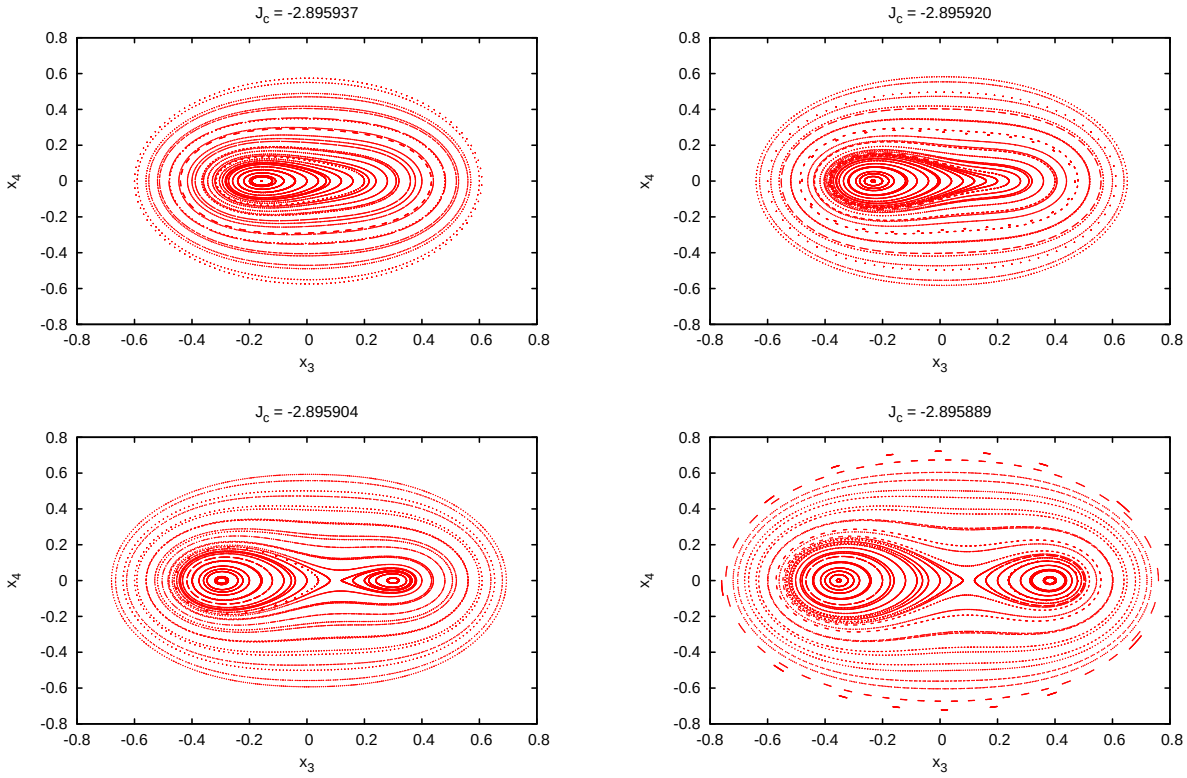

Figure 4.20: *For $\delta = 0.005$. Poincaré section for $x_2 = 0$ for different $\widetilde{J}_C$. From left to right, top to bottom: $\widetilde{J}_C = -2.895937, -2.895920, -2.895904, -2.895889$.*

appreciate the saddle - node bifurcation on the family of periodic orbits that was seen in Section 4.2.1.

If we remember Figure 4.17, we saw that the planar family of periodic orbits experiences a pitchfork bifurcation as the energy level increases, which gives rise to the Halo orbits. Now in Figures 4.20 and 4.21 we can see how for $\delta \neq 0$, due to the symmetry breaking on the equations motion, this bifurcation is replaced by a saddle - node bifurcation.

The main difference between the behaviour for $\delta = 0.005$ or $\delta = 0.01$ is that the phase space becomes "less symmetric" as δ increases.

4.4 Conclusions

In this Chapter we have focused on the understanding of the non - linear dynamics for a family of fixed points close to SL_1. We have restricted to the particular case $\alpha = 0$ to take advantage of the reversible character of the system, as it ensures us the existence of

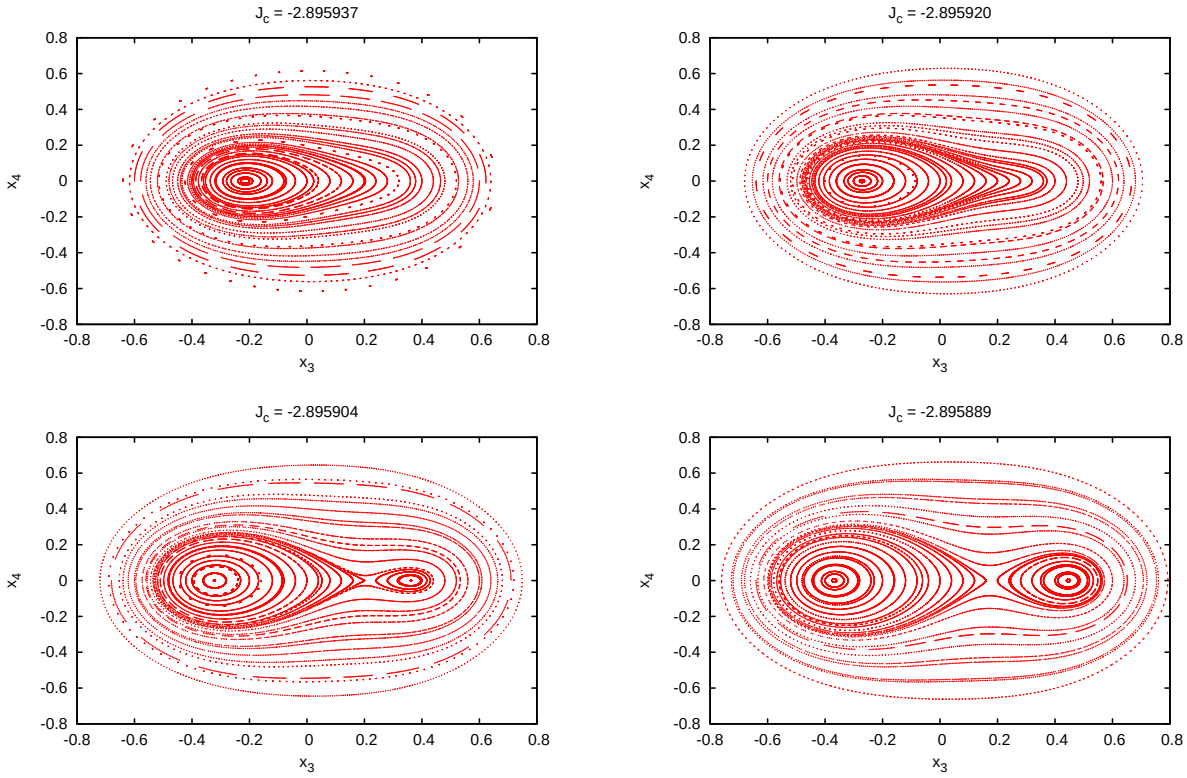

Figure 4.21: *For $\delta = 0.01$. Poincaré section for $x_2 = 0$ for different $\widetilde{J}_C$. From left to right, top to bottom: $\widetilde{J}_C = -2.895937, -2.895920, -2.895904, -2.895889$.*

families of periodic orbits and invariant tori.

For this study we have computed the families of periodic orbits by means of a continuation method. Furthermore, we have performed the reduction to the centre manifold using the graph transform method (Chapter 3) around the different equilibrium points to have a better understanding of the bounded motion.

We find that when the sail is perpendicular to the Sun - line the system behaves qualitatively as the RTBP. The two frequencies defining the centre motion give rise to two families of periodic orbits, a planar and a vertical family, and we find families of invariant tori due to the interaction between the two frequencies. As we move along the planar family of periodic orbits a pitchfork bifurcation takes place, and two families of Halo - type orbits appear.

When the sail is no longer perpendicular to the ($\delta \neq 0$) this behaviour varies slightly. We still have two families of periodic orbits emanating from the two fixed points, each one related to one of the two frequencies defining the centre motion. But we no longer have a pitchfork bifurcation that gives rise to the Halo - type orbits, this one has been replaced

by a saddle - node bifurcation due to the symmetry breaking of the system. Finally, we also find families of invariant tori due to the interaction between the two frequencies.

Summary & Future Work

In this thesis we have studied the natural dynamics of a solar sail in the Earth - Sun system and derived station keeping strategies using Dynamical System tools.

We have used the Restricted Three Body Problem including the solar radiation pressure as a model. It is known that the extra effect of the solar sail on the RTBP adds to the system a 2D family of equilibria parametrised by the sail orientation. These artificial new equilibria open a wide new range of possible mission applications that cannot be achieved by a conventional spacecraft. Moreover, these new equilibria are in general unstable but controllable by means of a feedback control strategy.

We have derived a station keeping strategy for a Solar Sail using dynamical systems tools. In Chapter 2 we described the details of these strategies. We recall that the main idea relies in understanding the variation of the dynamics close to an equilibrium point when the sail orientation is changed. Then try to find an appropriate sequence of changes in the sail orientation so that the phase space acts in our favour. We have used the same ideas to derive a strategy to move along the family of equilibrium points in a controlled way.

We find a sequence of changes in the sail orientation, discrete in time, that manage to maintain the sail in a close neighbourhood of a given fixed point. This differs from the solutions seen in the literature where, using optimisation techniques, they find a continuous change on the sail orientation to keep the sails trajectory close to equilibria.

We have tested our strategies in two particular missions: the Geostorm Warning Mission and the Polar Observer. We have also tested the robustness of our algorithms including errors on the sail orientation at each manoeuvre and errors on the position and velocity determination. Several Monte Carlo simulations have been done considering the different sources of errors. We see that the errors on the sail's orientations have a bigger impact on the final result than the errors on position and velocity determination.

An advantage of our strategies is that the mission does not require previous planning as the decisions taken by the probe only depend on its position in the phase space. In

this way, one can deal with errors during the mission in a more flexible way.

In the near future, we would like to extend these ideas to derive strategies to maintain the trajectory of a solar sail around an unstable periodic orbit. For instance, we could consider the Halo - type orbits about SL_1 and SL_2 or periodic orbits above the ecliptic plane. They all offer interesting mission applications.

Moreover, we would also like to use these ideas to derive station keeping strategies around a fixed point for a low - thrust satellite. Here the system has an extra parameter, as we can turn on and off the thrust or we can choose, within some range, the thrust magnitude, something that is not possible with a solar sail. This adds an extra dimension to the surfaces of artificial equilibria. Furthermore, we have more freedom in the thrust direction than with a solar sail. To this end, it seems that the same ideas are applicable and that we would also be able to control the trajectories of a low - thrust probe.

In the second part of this thesis we have studied the dynamics of the system close to SL_1. Most of these equilibrium points are of the type centre $\times$ centre $\times$ saddle. We have developed numerical tools to understand the periodic and quasi-periodic motion around these type of points. In Chapter 3 we describe the main details on the implementation of the Graph Transform method for the reduction to the centre manifold. We have also compared it with the Lie series method by taking the public software [Jor] and adapting it to our model. It turns out that the graph transform method is more efficient than the Lie series method in terms of computational time.

In Chapter 4 we have used these method to describe the non linear dynamics in an extended neighbourhood of the equilibrium points close to SL_1. We have considered $\alpha = 0$, and studied how different orientations in δ affected to the periodic and quasi-periodic motion of the system. In this particular case, the system is time reversible and the family of fixed points close to SL_1 remains fixed by the reversibility. Hence, the system has a local Hamiltonian behaviour around these points. In particular, the fixed points that appear close to SL_1 are of the type saddle $\times$ centre $\times$ centre.

We have seen that when the sail is perpendicular to the Sun - sail line ($\alpha = \delta = 0$), the systems behaves essentially as the RTBP close to L_1. We find families of planar and vertical periodic orbits given by each of the two frequencies defining the centre motion. The coupling between the two frequencies gives rise to families of invariant tori. We can also see that for larger energy values Halo - type orbits appear. If we consider $\delta \neq 0$ this picture persists. Due to the reversible character of the system we still find two families of periodic orbits emanating from the fixed point and families of invariant tori. We also find Halo - type orbits, although they are no longer symmetric one to the other.

If we consider $\alpha \neq 0$ the fixed points are no longer of the type saddle $\times$ centre $\times$ centre and the system is not time reversible. The dynamics on the centre projection spirals inwards or outwards depending on the fixed point. We would like to study if at some distance from the equilibrium point these periodic and quasi - periodic orbits persist when $\alpha \neq 0$.

Appendix A

Expansion of the Equations of Motion

Here we give the recurrent expressions that we have used in our computations of the reduction to the centre manifold. In Chapter 4 we have studied the case $\alpha = 0$, $\delta \in [-\pi/2, \pi/2]$. Due to some simplifications that can be done on the set of equations we consider two separate cases: $\alpha = \delta = 0$ and $\alpha = 0, \delta \neq 0$. We have used the well known Legendre polynomials to expand the equations of motion in a recurrent way.

The *Legendre polynomials* are defined by the formula,

$$P_0(x) = 1, \qquad P_n(x) = \frac{1}{2^n n!}\frac{d^n}{dx^n}[(x^2-1)^n], \quad \text{for } n = 1, 2, \dots , \tag{A.1}$$

where $P_n(x)$ is a polynomial of degree n. Equivalently the $P_n(x)$ can also be defined as the coefficients in the Taylor series expansion (at $t = 0$),

$$\frac{1}{\sqrt{1-2xt-t^2}} = \sum_{n=0}^{\infty} P_n(x)t^n. \tag{A.2}$$

Let us give some properties on the Legendre polynomials [AS92].

1. They are orthogonal w.r.t. the $\mathcal{L}^2$ inner product on the interval $[-1, 1]$:

$$\int_{-1}^{1} P_m(x)P_n(x)dx = \frac{2}{2n+1}\delta_{mn}. \tag{A.3}$$

2. They are symmetric or antisymmetric depending on the degree:

$$P_n(-x) = (-1)^n P_n(x). \tag{A.4}$$

3. They can be constructed using the recurrent relations:

$$(n+1)P_{n+1}(x) = (2n+1)xP_n(x) - nP_{n-1}(x), \tag{A.5}$$

with $P_0(x) = 1$ and $P_1(x) = x$. They also satisfy,

$$\frac{x^2-1}{n}\frac{d}{dx}P_n(x) = xP_n(x) - P_{n-1}(x). \tag{A.6}$$

It is not difficult to verify, from equation (A.2), that,

$$\frac{1}{\sqrt{(x-A)^2+(y-B)^2+(z-C)^2}} = \frac{1}{D}\sum_{n=0}^{\infty}\left(\frac{\rho}{D}\right)^n P_n\left(\frac{Ax+By+Cz}{D}\right), \tag{A.7}$$

where $D^2 = A^2 + B^2 + C^2$ and $\rho^2 = x^2 + y^2 + z^2$. We will use this expression to expand the nonlinear terms of the equations of motion.

A.1 When the sail is perpendicular to the Sun - sail line

When the sail is perpendicular to the Sun - sail direction $\alpha = \delta = 0$ and the equations take the simplified form:

$$\ddot{X} - 2\dot{Y} = \frac{\partial\Omega}{\partial X}, \qquad \ddot{Y} + 2\dot{X} = \frac{\partial\Omega}{\partial X}, \qquad \ddot{Z} = \frac{\partial\Omega}{\partial Z}, \tag{A.8}$$

where

$$\Omega(X,Y,Z) = \frac{1}{2}(X^2+Y^2) + \frac{(1-\mu)(1-\beta)}{r_{PS}} + \frac{\mu}{r_{PE}},$$

and r_{PS}, r_{PE} are the distances to the Sun and Earth respectively. See Appendix B for further discussions on the dynamical properties of this particular case.

We start by translating the origin of coordinates to one of the fixed points $SL_{1,2,3}$,

using the change of variables:

$$X = \mp\xi_i x + \mu + a_i, \qquad Y = \mp\xi_i y, \qquad Z = \xi_i z, \tag{A.9}$$

where the upper sign corresponds to $SL_{1,2}$ and the lower to SL_3, $a_1 = -1 + \xi_1$, $a_2 = -1 - \xi_2$ and $a_3 = \xi_3$. To have good numerical properties for the coefficients of the Taylor expansion, we scale the distance from the fixed point to the closest primary to one [JM99, Jor99].

Using equation (A.7) we have that the equations of motion around the equilibrium point in these new coordinates can be rewritten as,

$$\ddot{x} - 2\dot{y} - (1 + 2c_2)x = \frac{\partial}{\partial x}\sum_{n\geq 3} c_n(\mu,\beta)\rho^n P_n\left(\frac{x}{\rho}\right), \tag{A.10}$$

$$\ddot{y} + 2\dot{x} + (c_2 - 1)y = \frac{\partial}{\partial y}\sum_{n\geq 3} c_n(\mu,\beta)\rho^n P_n\left(\frac{x}{\rho}\right), \tag{A.11}$$

$$\ddot{z} + c_2 z = \frac{\partial}{\partial z}\sum_{n\geq 3} c_n(\mu,\beta)\rho^n P_n\left(\frac{x}{\rho}\right), \tag{A.12}$$

where the left - hand side contains the linear terms and the right - hand side the nonlinear ones. The coefficients $c_n(\mu,\beta)$ are given by,

$$c_n(\mu,\beta) = \begin{cases} \dfrac{1}{\xi_i^3}\left((\pm 1)^n\mu + (-1)^n\dfrac{(1-\mu)(1-\beta)\xi_i^{n+1}}{(1\mp\xi_i)^{n+1}}\right), & \text{for } SL_i,\ i = 1,2 \\ \dfrac{(-1)^n}{\xi_3^3}\left((1-\mu)(1-\beta) + \dfrac{\mu\xi_3^{n+1}}{(1+\xi_3)^{n+1}}\right), & \text{for } SL_3. \end{cases} \tag{A.13}$$

The upper sign of the first equation is for SL_1 and the lower sign for SL_2.

We define,

$$T_n(x,y,z) = \rho^n P_n\left(\frac{x}{\rho}\right).$$

Using equation (A.5) one can see that $T_n(x,y,z)$ is a homogeneous polynomial of degree n satisfies the recurrent expression,

$$T_n = \frac{2n-1}{n}xT_{n-1} - \frac{n-1}{n}(x^2+y^2+z^2)T_{n-1}, \tag{A.14}$$

with $T_0 = 1$ and $T_1 = x$. Now we can find recurrences to compute, $\partial T_n/\partial x$, $\partial T_n/\partial y$ and

$\partial T_n/\partial z$. Deriving equation (A.14) and using the equation (A.6) we see that,

$$\frac{\partial T_{n+1}}{\partial x} = (n+1)T_n, \qquad \frac{\partial T_n}{\partial y} = yR_{n-1}, \qquad \frac{\partial T_n}{\partial z} = zR_{n-1},$$

where $R_n(x, y, z)$ is also a homogeneous polynomial of degree n and satisfies the recurrent expression,

$$R_n(x, y, z) = \frac{2n+3}{n+2}xR_{n-1} - \frac{2n+2}{n+2}T_n - \frac{n+1}{n+2}(x^2+y^2+z^2)R_{n-2}, \tag{A.15}$$

with $R_0 = -1$ and $R_1 = -3x$.

Finally, the expansion of the equations of motion is:

$$\begin{aligned} \ddot{x} - 2\dot{y} - (1+2c_2)x &= \sum_{n\geq 2} c_{n+1}(\mu,\beta)(n+1)T_n, \\ \ddot{y} + 2\dot{x} + (c_2-1)y &= y\sum_{n\geq 2} c_{n+1}(\mu,\beta)R_{n-1}, \\ \ddot{z} + c_2 z &= z\sum_{n\geq 2} c_{n+1}(\mu,\beta)R_{n-1}. \end{aligned} \tag{A.16}$$

A.2 When the sail is not perpendicular to the Sun - sail line

Here we consider the sail orientation to satisfy $\alpha = 0$ and $\delta \neq 0$. In Chapter 4 we focus on the equilibrium points on the FL_1 family. These equilibrium points are on the $Y = 0$ plane between the Earth and Sun ($\mu - 1 < X < \mu$). We also have that the equations of motion take the simplified form:

$$\begin{aligned} \ddot{X} - 2\dot{Y} &= \frac{\partial \widetilde{\Omega}}{\partial X} - \beta\frac{(1-\mu)}{r_{PS}^3}\frac{(X-\mu)Z}{r_2}\cos^2\delta\sin\delta, \\ \ddot{Y} + 2\dot{X} &= \frac{\partial \widetilde{\Omega}}{\partial Y} - \beta\frac{(1-\mu)}{r_{PS}^3}\frac{YZ}{r_2}\cos^2\delta\sin\delta, \\ \ddot{Z} &= \frac{\partial \widetilde{\Omega}}{\partial Z} + \beta\frac{(1-\mu)}{r_{PS}^3}r_2\cos^2\delta\sin\delta, \end{aligned} \tag{A.17}$$

where

$$\widetilde{\Omega} = \frac{1}{2}\left(X^2 + Y^2\right) + \frac{(1-\mu)(1-\beta\cos^3\delta)}{r_{PS}} + \frac{\mu}{r_{PE}}.$$

We start by translating the fixed point, $(X^*, 0, Z^*)$, to the origin and scale so that the distance to the closest primary is 1. This is done to have good numerical properties on the coefficients of the Taylor expansion. As β is small the closest primary is always the Earth. This change of variable is:

$$X = -\xi x + X^*, \qquad Y = -\xi y, \qquad Z = \xi z + Z^*, \tag{A.18}$$

where $\xi = \sqrt{(X^* - \mu + 1)^2 + (Z^*)^2}$ is the distance between the fixed point and the Earth.

After this linear change of variables, equation (A.17) takes the form,

$$\begin{aligned}
\ddot{x} &= 2\dot{y} + x - \frac{X^*}{\xi} - \mathcal{K}_S\frac{(x - \frac{X^*-\mu}{\xi})}{r_{ps}^3} - \mathcal{K}_E\frac{(x - \frac{X^*-\mu+1}{\xi})}{r_{pe}^3} - \mathcal{K}_{ss}\frac{(x - \frac{X^*-\mu}{\xi})(z + \frac{Z^*}{\xi})}{r_{ps}^3 r_2},\\
\ddot{y} &= -2\dot{x} + y - \left(\frac{\mathcal{K}_S}{r_{ps}^3} + \frac{\mathcal{K}_E}{r_{pe}^3}\right) y \; - \; \mathcal{K}_{ss}\frac{y(z + \frac{Z^*}{\xi})}{r_{ps}^3 r_2},\\
\ddot{z} &= -\left(\frac{\mathcal{K}_S}{r_{ps}^3} + \frac{\mathcal{K}_E}{r_{pe}^3}\right)\left(z + \frac{Z^*}{\xi}\right) \; + \; \mathcal{K}_{ss}\frac{r_2}{r_{ps}^3}.
\end{aligned} \tag{A.19}$$

where $\mathcal{K}_S = (1-\mu)(1-\beta\cos^3\delta)/\xi^3$, $\mathcal{K}_E = \mu/\xi^3$ and $\mathcal{K}_{ss} = \beta(1-\mu)\cos^2\delta\sin\delta/\xi^3$. Now,

$$\begin{aligned}
r_{ps} &= \sqrt{(x - (X^* - \mu)/\xi)^2 + y^2 + (z + Z^*/\xi)^2},\\
r_{pe} &= \sqrt{(x - (X^* - \mu + 1)/\xi)^2 + y^2 + (z + Z^*/\xi)^2},\\
r_2 &= \sqrt{(x - (X^* - \mu)/\xi)^2 + y^2}.
\end{aligned}$$

To expand the nonlinear terms in a recurrent way we use equation (A.7).

Let us take $1/r_{ps}$:

$$\frac{1}{r_{ps}} = \frac{1}{\sqrt{(x - (X^* - \mu)/\xi)^2 + y^2 + (z + Z^*/\xi)^2}} = \sum_{n\geq 0}\left(\frac{\xi}{\eta}\right)^{n+1}\rho^n P_n\left(\frac{(X^* - \mu)x - Z^* z}{\eta\rho}\right),$$

where $\eta = \sqrt{(X^* - \mu)^2 + (Z^*)^2}$.

We define $TS_n(x, y, z) = \rho^n P_n\left(\frac{(X^*-\mu)x - Z^* z}{\eta\rho}\right)$. Using equation (A.5) we see that this

is a homogeneous polynomial of degree n that satisfies the recurrent expression:

$$TS_{n+1} = \frac{2n+1}{n+1}\left(\frac{(X^*-\mu)x - Z^*z}{\eta}\right)TS_n - \frac{n}{n+1}\rho^2 TS_{n-1}, \tag{A.20}$$

with $TS_0(x,y,z) = 1,\ TS_1(x,y,z) = \dfrac{(X^*-\mu)x - Z^*z}{\eta}$. Hence,

$$\frac{1}{r_{ps}} \ = \ \sum_{n\geq 0}\left(\frac{\xi}{\eta}\right)^{n+1} TS_n(x,y,z),$$

The same can be done for $1/r_{pe}$:

$$\frac{1}{r_{pe}} = \frac{1}{\sqrt{(x-(X^*-\mu+1)/\xi)^2 + y^2 + (z+Z^*/\xi)^2}} = \sum_{n\geq 0}\rho^n P_n\left(\frac{(X^*-\mu+1)x - Z^*z}{\xi\rho}\right).$$

We define $TE_n = \rho^n P_n\left(\frac{(X^*-\mu+1)x - Z^*)z}{\xi\rho}\right)$. It also is a homogeneous polynomial of degree n and using equation (A.5) we see that they can also be found in a recurrent way:

$$TE_{n+1} = \frac{2n+1}{n+1}\left(\frac{(X^*-\mu+1)x - Z^*z}{\xi}\right)TE_n - \frac{n}{n+1}\rho^2 TE_{n-1}, \tag{A.21}$$

with $TE_0(x,y,z) = 1,\ TE_1(x,y,z) = \dfrac{(X^*-\mu+1)x - Z^*z}{\xi}$. Hence,

$$\frac{1}{r_{pe}} \ = \ \sum_{n\geq 0} TE_n(x,y,z),$$

Finally, for $1/r_2$,

$$\frac{1}{r_2} = \frac{1}{\sqrt{(x-(X^*-\mu)/\xi)^2 + y^2}} = \sum_{n\geq 0}\left(\frac{\xi}{|X^*-\mu|}\right)^{n+1}\bar{\rho}^n P_n\left(\frac{-x}{\rho}\right),$$

where $\bar{\rho} = x^2 \ + \ y^2$. We define $Tb_n = \bar{\rho}^n P_n\left(\frac{x}{\rho}\right)$, that is also a homogeneous polynomial of degree n that satisfies the recurrent expression:

$$Tb_{n+1} = \frac{2n+1}{n+1}xTb_n - \frac{n}{n+1}\bar{\rho}^2 Tb_{n-1}, \tag{A.22}$$

with, $Tb_0 = 1, Tb_1 = x$. Hence,

$$\frac{1}{r_2} = \sum_{n\geq 0}(-1)^n\left(\frac{\xi}{|X^*-\mu|}\right)^{n+1} Tb_n(x,y).$$

With all this, equation (A.17) can be written as,

$$\begin{aligned}
\ddot{x} &= 2\dot{y} + x - \frac{X^*}{\xi} - \mathcal{K}_S \left[\sum_{n\geq 0} c_n TS_n\right]^3 \left(x - \frac{X^*-\mu}{\xi}\right) - \mathcal{K}_E \left[\sum_{n\geq 0} TE_n\right]^3 \left(x - \frac{X^*-\mu+1}{\xi}\right) \\
&\quad -\mathcal{K}_{ss} \left[\sum_{n\geq 0} c_n TS_n\right]^3 \left[\sum_{n\geq 0} d_n Tb_n\right] \left(x - \frac{X^*-\mu}{\xi}\right)\left(z + \frac{Z^*}{\xi}\right), \\
\ddot{y} &= -2\dot{x} + \left(1 - \mathcal{K}_S \left[\sum_{n\geq 0} c_n TS_n\right]^3 - \mathcal{K}_E \left[\sum_{n\geq 0} TE_n\right]^3 - \mathcal{K}_{ss} \left[\sum_{n\geq 0} c_n TS_n\right]^3 \left[\sum_{n\geq 0} d_n Tb_n\right] \left(z + \frac{Z^*}{\xi}\right)\right) y, \\
\ddot{z} &= -\left(\mathcal{K}_S \left[\sum_{n\geq 0} c_n TS_n\right]^3 + \mathcal{K}_E \left[\sum_{n\geq 0} TE_n\right]^3\right)\left(z + \frac{Z^*}{\xi}\right) + \mathcal{K}_{ss} \left[\sum_{n\geq 0} c_n TS_n\right]^3 \left[\sum_{n\geq 0} d_n Tb_n\right]^{-1}.
\end{aligned} \tag{A.23}$$

where, $c_n = \left(\frac{\xi}{\eta}\right)^{n+1}$ and $d_n = (-1)^n \left(\frac{\xi}{|X^*-\mu|}\right)^{n+1}$.

Notice that at some point we need to invert the power series $\left[\sum_{n\geq 0} d_n Tb_n\right]$. Once we have computed its the power expansion up to a given order N we can invert this series with a simple iteration scheme [Knu81].

Let $SQ = \sum_{|k|=0}^{N} q_k x^k$ and $SR = SQ^{-1} = \sum_{|k|=0}^{N} r_k x^k$, then it is easy to check that the coefficient r_k satisfy,

$$\begin{aligned}
r_0 &= 1/q_0, \\
r_k &= \frac{1}{q_k}\left(\sum_{|j|=0}^{|k|-1} q_{k-j}\ r_j\right), \qquad \text{for } |k| = 1, \ldots, N.
\end{aligned}$$

Appendix B

Equilibrium Points when the Sail is Perpendicular to the Sun - line

In this Appendix we focus on the particular case of a perfectly reflecting sail that is oriented perpendicular to the Sun - sail line ($\alpha = \delta = 0$). Notice that the force due to the sail is in the opposite direction to the Sun's gravitational attraction. As we will see, the system has lots of similarities with the RTBP. In some sense we can think that we are changing the mass of the Sun.

The equations of motion of the RTBPS for this particular case are simplified. When $\alpha = \delta = 0$ we have that,

$$\vec{n} = \left(\frac{(X-\mu)}{r_{PS}}, \frac{Y}{r_{PS}}, \frac{Z}{r_{PE}} \right).$$

The equations of motion can be written as:

$$\ddot{X} - 2\dot{Y} = \frac{\partial \Omega}{\partial X}, \qquad \ddot{Y} + 2\dot{X} = \frac{\partial \Omega}{\partial X}, \qquad \ddot{Z} = \frac{\partial \Omega}{\partial Z}, \tag{B.1}$$

where

$$\Omega(X, Y, Z) = \frac{1}{2}(X^2 + Y^2) + \frac{(1-\mu)(1-\beta)}{r_{PS}} + \frac{\mu}{r_{PE}},$$

and r_{PS}, r_{PE} are the distances to the Sun and Earth respectively. As in the RTBP this system has a first integral, similar to the Jacobi constant,

$$J_C = \dot{X}^2 + \dot{Y}^2 + \dot{Z}^2 - 2\Omega(X, Y, Z).$$

If we introduce the classical momentums $P_X = \dot{X} - Y$, $P_Y = \dot{Y} + X$ and $P_Z = \dot{Z}$, the equations take the Hamiltonian form, where

$$H = \frac{1}{2}(P_X^2 + P_Y^2 + P_Z^2) + YP_X - XP_Y - \frac{(1-\mu)(1-\beta)}{r_{PS}} - \frac{\mu}{r_{PE}}.$$

Here we consider $\mu = \mu_{SE}$ and $\beta \in [0, 1]$, although only small values for β are considered realistic (Section 1.1.2).

To have an equilibrium point we need $\dfrac{\partial\Omega}{\partial X} = \dfrac{\partial\Omega}{\partial Y} = \dfrac{\partial\Omega}{\partial Z} = 0$. Hence,

$$0 = X - (1-\mu)(1-\beta)\frac{X-\mu}{r_{PS}^3} - \mu\frac{X-\mu+1}{r_{PE}^3}, \tag{B.2}$$

$$0 = Y\left(1 - \frac{(1-\mu)(1-\beta)}{r_{PS}^3} - \frac{\mu}{r_{PE}^3}\right), \tag{B.3}$$

$$0 = -Z\left(\frac{(1-\mu)(1-\beta)}{r_{PS}^3} + \frac{\mu}{r_{PE}^3}\right). \tag{B.4}$$

Notice that equation (B.4) is true if and only if $Z = 0$ as the other part is always the sum of two positive quantity for $\beta \in [0, 1]$. Hence, the fixed points lie on the XY plane. Now we focus on equation (B.3) and distinguish two possible cases, $Y = 0$ or $Y \neq 0$.

CASE I $(Y = 0)$**.**

If $Y = Z = 0$ equation (B.2) turns into:

$$X - (1-\mu)(1-\beta)\frac{X-\mu}{|X-\mu|^3} - \mu\frac{X-\mu+1}{|X-\mu+1|^3} = 0,$$

we follow the same scheme as in [Sze67] to find the values of X that satisfy this equation. We consider three different cases, (a) the fixed point is on the left-hand side of both primaries, (b) the fixed point is between the two primaries, and (c) the fixed point is on the right-hand side of both primaries.

(a) $X - \mu < 0$ and $X - \mu + 1 < 0$:

So $|X - \mu| = \mu - X$ and $|X - \mu + 1| = \mu - 1 - X$ then,

$$X + \frac{(1-\mu)(1-\beta)}{(\mu - X)^2} + \frac{\mu}{(1-\mu-X)^2} = 0.$$

We consider $\xi = \mu - 1 - X$, the distance to the closest primary, the Earth, so:

$$\mu - 1 - \xi + \frac{(1-\mu)(1-\beta)}{(\xi+1)^2} + \frac{\mu}{\xi^2} = 0,$$

and the following quintic must be satisfied,

$$\xi^5 + (3-\mu)\xi^4 + (3-2\mu)\xi^3 - (\mu\beta - \beta + \mu)\xi^2 - 2\mu\xi - \mu = 0. \tag{B.5}$$

(b) $X - \mu < 0$ and $X - \mu + 1 > 0$:

So $|X - \mu| = \mu - X$ and $|X - \mu + 1| = X - \mu + 1$ then,

$$X + \frac{(1-\mu)(1-\beta)}{(\mu - X)^2} - \frac{\mu}{(X - \mu + 1)^2} = 0.$$

We consider $\xi = X - \mu + 1$, then,

$$\xi + \mu - 1 + \frac{(1-\mu)(1-\beta)}{(1-\xi)^2} - \frac{\mu}{\xi^2} = 0,$$

and the following quintic must be satisfied,

$$\xi^5 - (3-\mu)\xi^4 + (3-2\mu)\xi^3 + (\mu\beta - \beta - \mu)\xi^2 + 2\mu\xi - \mu = 0. \tag{B.6}$$

(c) $X - \mu > 0$ and $X - \mu + 1 > 0$:

So $|X - \mu| = X - \mu$ and $|X - \mu + 1| = X - \mu + 1$ then,

$$X - \frac{(1-\mu)(1-\beta)}{(\mu - X)^2} - \frac{\mu}{(X - \mu + 1)^2} = 0.$$

We consider $\xi = X - \mu$ the distance to the closest primary, the Sun, so:

$$\xi + \mu - \frac{(1-\mu)(1-\beta)}{\xi^2} - \frac{\mu}{(\xi + 1)^2} = 0,$$

and the following quintic must be satisfied,

$$\xi^5 + (2+\mu)\xi^4 + (1+2\mu)\xi^3 - (1-\mu)(1-\beta)\xi^2 - 2(1-\mu)(1-\beta)\xi - (1-\mu)(1-\beta) = 0. \tag{B.7}$$

We follow the classical RTBP notation and consider SL_1 to be the fixed point between both primaries and SL_2 and SL_3 the fixed points at the left hand side and right hand side of both primaries respectively. Hence,

$$SL_1 = (\mu - 1 + \xi_1, 0, 0), \qquad SL_2 = (\mu - 1 - \xi_2, 0, 0), \qquad SL_3 = (\mu + \xi_3, 0, 0),$$

where ξ_1, ξ_2 and ξ_3 are the positive solutions of the quintics (B.6), (B.5) and (B.7) respectively. In Figure B.1 we can see the position of these three equilibrium point for $\beta \in [0, 1]$. Notice that as β tends to 1 the fixed points come closer to the Sun. For $\beta = 1$, SL_1 and SL_3 collide with the Sun, and SL_2 gets closer to the Earth, but not colliding with it.

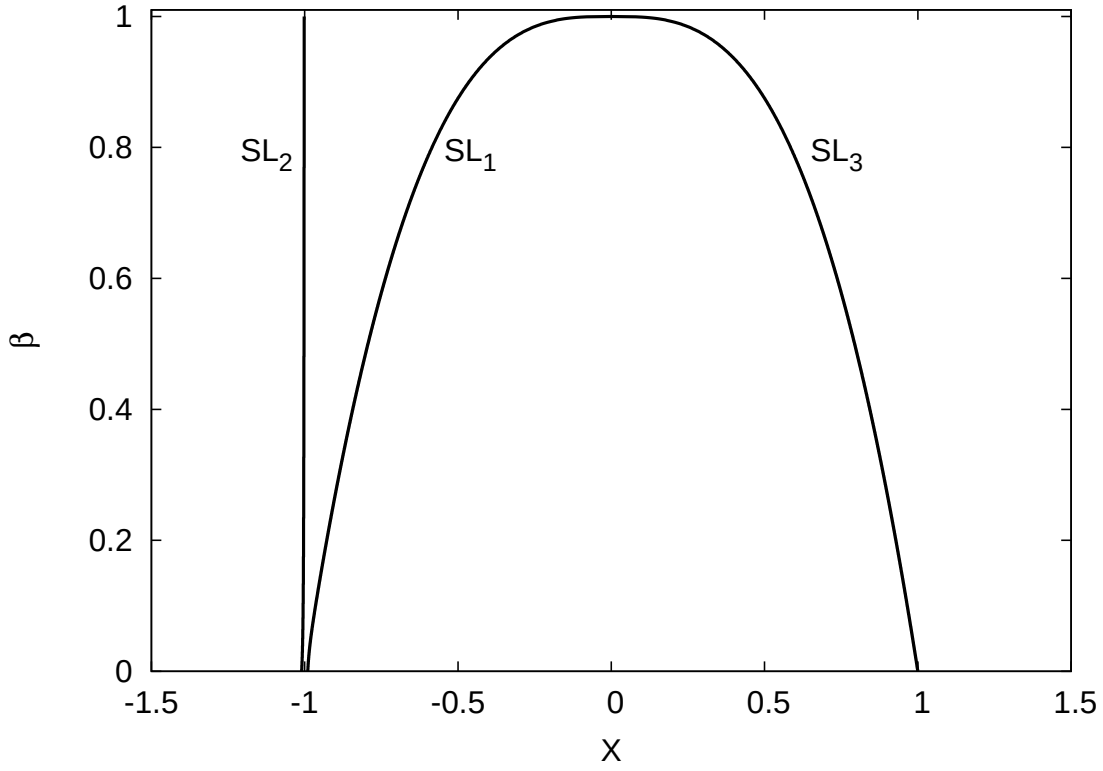

Figure B.1: *Position of the three collinear equilibrium points $SL_{1,2,3}$ for $\beta \in [0, 1]$.*

CASE II $(Y \neq 0)$.

For equation (B.3) to be true we need,

$$1 - \frac{(1-\mu)(1-\beta)}{r_{PS}^3} - \frac{\mu}{r_{PE}^3} = 0.$$

Without loss of generality, we take $r_{PE} = R$ and $r_{PS} = d \cdot R$ and we try to find R and d that satisfy equations (B.2) and (B.3). Then,

$$\begin{aligned} 0 &= X - (1-\mu)(1-\beta)\frac{X-\mu}{d^3R^3} - \mu\frac{X-\mu+1}{R^3}, \\ 0 &= 1 - \frac{(1-\mu)(1-\beta)}{d^3R^3} - \frac{\mu}{R^3}, \end{aligned} \tag{B.8}$$

equivalently,

$$\begin{aligned} 0 &= (d^3R^3 - (1-\mu)(1-\beta) - d^3\mu)X + (1-\mu)(1-\beta)\mu - \mu(1-\mu)d^3, \\ 0 &= d^3R^3 - (1-\mu)(1-\beta) - d^3\mu, \end{aligned} \tag{B.9}$$

This holds if,

$$d^3R^3 - (1-\mu)(1-\beta) - d^3\mu = 0 \;\text{ and }\; (1-\mu)(1-\beta)\mu - \mu(1-\mu)d^3 = 0.$$

Finally, we get that $d = (1-\beta)^{1/3}$ and $R = 1$. This means that the fixed points with $Y \neq 0$ must satisfy $r_{PE} = 1$ and $r_{PS} = (1-\beta)^{1/3}$. It is easy to see that this is true for,

$$X = \mu - \frac{(1-\beta)^{2/3}}{2}, \qquad Y = \pm(1-\beta)^{1/3}\left[1 - \frac{(1-\beta)^{2/3}}{4}\right]^{1/2}.$$

Hence, we have two other fixed points $SL_{4,5}$:

$$\left(\mu - \frac{(1-\beta)^{2/3}}{2}, \pm(1-\beta)^{1/3}\left[1 - \frac{(1-\beta)^{2/3}}{4}\right]^{1/2}, 0\right).$$

Again, as β tends to 1 these two points come closer to the Sun, colliding with it for $\beta = 1$.

To summarise, this problem has 5 equilibrium points: Three of them ($SL_{1,2,3}$) lay on the line joining the two primaries, and their position is found by finding the only positive root of a quintic; The other two fixed points ($SL_{4,5}$) lay on the X, Y and can be found as one of the vertexes of an isosceles triangle taking the other two primaries as vertexes. The ratio of this triangles is 1 to $(1-\beta)^{1/3}$, where the small distance is given by the Sun - $SL_{4,5}$ side. In Figure B.2 we have a schematic representation of the fixed points position for a fixed β. As β increases, all the fixed points come closer to the Sun.

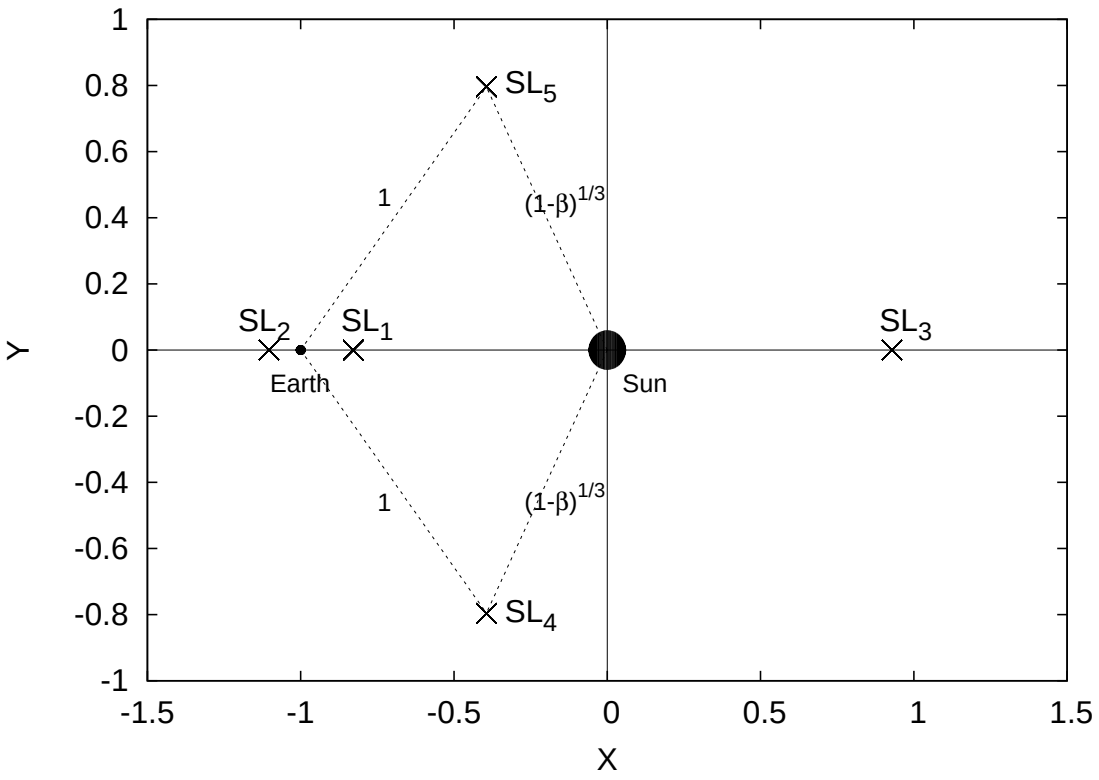

Figure B.2: *Schematic representation of the position of the equilibrium points* $SL_{1,\ldots,5}$ *for a fixed* β.

Bibliography

[AS92] M. Abramowitz and I.A. Stegun, editors. *Handbook of mathematical functions with formulas, graphs, and mathematical tables*. Dover Publications Inc., New York, 1992. Reprint of the 1972 edition.

[Car81] J. Carr. *Applications of Centre Manifold Theory*, volume 35 of *Applied Mathematical Series*. Springer-Verlag, New York, 1981.

[Cra91] J.D. Crawford. Introduction to bifurcation theory. *Reviews of Modern Physics*, 64(4), October 1991.

[Dev76] R. L. Devaney. Reversible diffeomorphisms and flows. *Trans. Amer. Math. Soc.*, 218:89–113, 1976.

[For90] R. L. Forward. Statite: A spacecraft that does not orbit. *Journal of Spacecraft*, 28(5):606–611, 1990.

[GJMS01] G. Gómez, À. Jorba, J. Masdemont, and C. Simó. *Dynamics and Mission Design Near Libration Points - Volume III: Advanced Methods for Collinear Points.*, volume 4 of *World Scientific Monograph Series in Mathematics*. World Scientific, 2001.

[GLMS01a] G. Gómez, J. Llibre, R. Martínez, and C. Simó. *Dynamics and Mission Design Near Libration Points - Volume I: Fundamentals: The Case of Collinear Libration Points*, volume 2 of *World Scientific Monograph Series in Mathematics*. World Scientific, 2001.

[GLMS01b] G. Gómez, J. Llibre, R. Martínez, and C. Simó. *Dynamics and Mission Design Near Libration Points - Volume II: Fundamentals: The Case of Triangular Libration Points.*, volume 3 of *World Scientific Monograph Series in Mathematics*. World Scientific, 2001.

[GSS85] M. Gulobitski, D.G. Schaeffer, and I.N. Stewart. *Singularities and Groups in Bifurcation Theory*. Springer-Verlag, 1985.

[Har08] A. Haro. Automatic differentiation tools in computational dynamical systems. Preprint, 2008.

[HMM+04] G.W. Hughes, M. MacDonald, C.R. McInnes, A. Atzei, and P. Falkner. Analysis of a solar sail mercury sample return mission. In *55th International Astronautical Congress*, Vancouver, Canada, 2004.

[JL] À. Jorba and R. Llave. Regularity properties of the centre manifolds and applications. In progress.

[JM99] À. Jorba and J. Masdemont. Dynamics in the centre manifold of the collinear points of the restricted three body problem. *Physica D 132*, pages 189–213, 1999.

[Jor] À. Jorba. `http://www.maia.ub.es/~angel/soft.html`.

[Jor99] À. Jorba. A methodology for the numerical computation of normal forms, centre manifolds and first integrals of hamiltonian systems. *Experimental Mathematics 8*, pages 155–195, 1999.

[Knu81] D.E. Knuth. *The art of computer programming. Vol. 2*. Addison-Wesley Publishing Co., Reading, Mass., second edition, 1981. Seminumerical algorithms, Addison-Wesley Series in Computer Science and Information Processing.

[Lan64] P. Lancaster. On eigenvalues of matrices dependent on a parameter. *Numerische Mathematik*, 6:377–387, December 1964.

[Lis05] M. Lisano. Solar sail transfer trajectory design and station keeping control for missions to Sub-L1 equilibrium region. In *15th AAS/AIAA Space Flight Mechanics Conferece*, Colorado, January 2005. AAS paper 05–219.

[LP04] D.A. Lawrence and S. Piggott. Solar sailing trajectory control for Sub-L1 stationkeeping. *AIAA 2004-5014*, 2004.

[LR98] J.S.W. Lamb and J.A.G. Roberts. Time-reversal symmetry in dynamical systems: a survey. *Phys. D*, 112(1-2):1–39, 1998. Time-reversal symmetry in dynamical systems (Coventry, 1996).

[McI99] C.R. McInnes. *Solar Sailing: Technology, Dynamics and Mission Applications*. Springer-Praxis, 1999.

[McI03] C.R. McInnes. Solar sailing: mission applications and engineering challanges. *Philosophical transactions of the Royal Society of London (Series A)*, pages 2989–3008, November 2003.

[MH91] K. R. Meyer and G. R. Hall. *Introduction to Hamiltonian Dynamical Systems and the N-Body Problem*. Springer, 1991.

[MM04] M. Macdonald and C.R. McInnes. A near - term road map for solar sailing. In *55th International Astronautical Congress*, Vancouver, Canada, 2004.

[MMSM94] C.R. McInnes, A.J.C. McDonald, J.F.L. Simmons, and E.W. MacDonald. Solar sail parking in restricted three-body system. *Journal of Guidance, Control and Dynamics*, 17(2):399–406, 1994.

[Mos58] J. K. Moser. On the generalization of a theorem of A. Liapounoff. *Comm. Pure Appl. Math.*, 11:257–271, 1958.

[Nel76] R. B. Nelson. Simplified calculation of eigenvector derivatives. *AIAA Journal*, 14:1201–1205, September 1976.

[PPP96] J-Y. Prado, A. Perret, and G. Pignolet. Using a solar sail for a plasma storm early warning system. In *47th International Astronautical Congress*, October 1996.

[Rol07] P. Roldan. *Analytical and Numerical Tools for the study of Normally Hyperbolic Invariant Manifolds in Hamiltonian Systems and their associated dynamics*. PhD thesis, Universitat Politécnica de Barcelona, 2007.

[RRS05] L. Rios-Reyes and D.J. Scheeres. Robust solar sail trajectory control for large pre-launch modelling errors. In *2005 AIAA Guidance, Navigation and Control Conference*, August 2005.

[SB02] J. Stoer and R. Bulirsch. *Introduction to numerical analysis*, volume 12 of *Texts in Applied Mathematics*. Springer-Verlag, New York, third edition, 2002. Translated from the German by R. Bartels, W. Gautschi and C. Witzgall.

[Sev86] M. B. Sevryuk. *Reversible Systems*, volume 1211 of *Lecture Notes in Mathematics*. Springer-Verlag, Berlin, 1986.

[Sev98] M. B. Sevryuk. The finite-dimensional reversible KAM theory. *Physica D: Nonlinear Phenomena*, 112(1-2):132–147, 1998. Proceedings of the Workshop on Time-Reversal Symmetry in Dynamical Systems.

[Sij85] J. Sijbrand. Properties of the centre manifold. *Transactions of the American Mathematical Society*, 289(2), June 1985.

[Sim90] C. Simó. *Les Méthodes Modernes de la Mecánique Céleste (Course given at Goutelas, France, 1989))*, chapter On the Analytical and Numerical Approximation of Invariant Manifolds, pages 285–329. Editions Frontières, 1990.

[SRM04] R. Stevens, I.M. Ross, and S.E. Motousek. Eath - mars return trajectories using solar sails. In *55th International Astronautical Congress*, Vancouver, Canada, 2004.

[Sze67] V. Szebehely. *Theory of orbits. The restricted problem of three bodies*. Academic Press, 1967.

[Van89] A. Vanderbauwhebe. *Centre Manifolds, Normal Forms and Elementary Bifurcations*, chapter 4. Dynamics Reported. A Series in Dynamical Systems and their Applications, Vol. 2. John Wiley & Sons Ltd., 1989.

[VdHM79] J.C. Van der Ha and V. J. Modi. Long-term evaluation of three-dimensional heliocentric solar sail trajectories with arbitrary fixed sail setting. *Celestial Mechanics*, 19:113–138, February 1979.

[Wes04] J.L. West. The Geostorm Warning Mission: enhanced opportunities based on new technology. In *14th AAS/AIAA Space Flight Mechanics Conference*. Pasadena, CA : Jet Propulsion Laboratory, National Aeronautics and Space Administration, 2004, February 2004.

[Wie04a] B. Wie. Solar sail attitude control and dynamics, part 1. *Journal of Guidance, Control and Dynamics*, 27(4):526–535, July-August 2004.

[Wie04b] B. Wie. Solar sail attitude control and dynamics, part 2. *Journal of Guidance, Control and Dynamics*, 27(4):536–544, July-August 2004.

[Wil65] J. Wilkinson. *The Algebraic Eigenvalue Problem*. Clarendon Press, 1965.

[WM07] T.J. Waters and C.R. McInnes. Periodic orbits above the ecliptic plane in the solar sail restricted 3-body problem. *Journal of Guidance, Control and Dynamics*, 30(3):786–693, 2007.

[WM08] T.J. Waters and C.R. McInnes. Invariant manifolds and orbit control in the solar sail 3-body problem. *Journal of Guidance, Control and Dynamics*, 31(3), May-June 2008.

[Yen04] C.-W. L. Yen. Solar sail Geostorm Warning Mission design. In *14th AAS/AIAA Space Flight Mechanics Conference*, Hawaii, February 2004.